Eucritetype achondrites: Petrology and oxygen isotope compositions

The Meteoritical Society

Meteoritics & Planetary Science 1–43 (2021)
doi: 10.1111/maps.13730

Eucrite-type achondrites: Petrology and oxygen isotope compositions†

David W. MITTLEFEHLDT[1*], Richard C. GREENWOOD[2], Eve L. BERGER[3], Loan LE[4], Zhan X. PENG[4§], and D. Kent ROSS[4,5††]

[1]Mail code XI3, Astromaterials Research Office, NASA/Johnson Space Center, Houston, Texas 77058, USA
[2]Planetary and Space Sciences, School of Physical Sciences, The Open University, Walton Hall, Milton Keynes MK7 6AA, UK
[3]Texas State University—Jacobs JETS Contract, NASA Johnson Space Center, Houston, Texas 77058, USA
[4]Jacobs JETS-NASA Johnson Space Center, Houston, Texas 77058, USA
[5]UTEP-CASSMAR, El Paso, Texas 79968, USA
[§]Current address: Department of Geological Sciences, California State University, Northridge, Northridge, California 91330, USA
*Corresponding author. E-mail: david.w.mittlefehldt@nasa.gov

(Received 26 February 2021; revision accepted 17 July 2021)

Abstract–We report petrologic studies and oxygen isotope analyses of normal and anomalous eucrites, termed eucrite-type achondrites. Petrologically anomalous eucrite-type achondrites can have normal oxygen isotope compositions, and vice versa. Two basaltic eucrites with normal oxygen isotope compositions contain pyroxenes with anomalous Fe/Mn engendered by parent body processes acting on normal eucrites: solid-state reduction by S gas in EET 87542, and reduction during crystallization by magmatic S in QUE 94484. Cataclastic basaltic breccias PCA 82502 and PCA 91007 are paired (petrology, anomalous oxygen). Although isotopically like Pasamonte, they are petrologically distinct. We confirm the petrological and isotopic anomalies of cumulate gabbro EET 92023; likely formed by impact melting of mixed cumulate and basaltic materials. Many main group eucrites include plagioclases that retain near-liquidus compositions despite metamorphic overprinting. Stannern group eucrites contain more sodic plagioclase, which is consistent with the melt hybridization hypothesis for Stannern group magma formation. The lack of more calcic plagioclase suggests reactive exchange of the anorthite component of the primary melt with the albitic component of the crust. Asteroids that are modestly different in composition can produce virtually indistinguishable basalts, providing a ready explanation for the eucrite-type achondrite suite. Small stochastic variations in petrologic evolution can cause substantial differences in rocks produced on an asteroid.

INTRODUCTION

Most mafic achondrites can be broadly categorized as being "eucritic," that is, they are composed of ferroan pigeonite and augite, high-Ca plagioclase, a silica polymorph, and an assortment of minor and accessory phases (Mittlefehldt 2015). They are petrologically distinct from angritic basalts and gabbros, which are composed mostly of Al-Ti-rich diopside–hedenbergite, magnesian to ferroan Ca-rich olivine, nearly pure anorthite and ferroan kirschsteinite (Keil 2012), or from what might be called brachinitic basalts (e.g., Graves Nunataks [GRA] 06128), which are composed mostly of intermediate-Mg orthopyroxene, augite and diopside, intermediate-Ca plagioclase, and ferroan olivine (Shearer et al. 2010; Day et al. 2012). The focus here is on mafic achondrites that are petrologically and mineralogically like eucrites. We refer to these as "eucrite-type achondrites" irrespective of whether they have anomalous characteristics (e.g., isotopic) or are typical eucrites in all respects. We reserve the term "eucrites" for those eucrite-type achondrites for which there is no isotopic evidence of anomalous character.

Early petrologic and compositional studies noted that eucrites, diogenites, and howardites are closely related, and

†This study is dedicated to the memory of John T. Wasson, friend and colleague, and for DWM, the mentor who molded him into the scientist he became.
††Deceased

a common parent object was proposed for them (e.g., Mason 1962; Duke and Silver 1967; Jérome and Goles 1971). Subsequently, O-isotope analyses that included ^{17}O showed that these data can be used to identify genetic associations among meteorite groups, and that the howardite, eucrite, and diogenite (HED) clan of meteorites form one such genetic association (Clayton et al. 1976). These early three-O-isotope analyses showed that some basalts considered at the time to be anomalous eucrites were instead related to other igneous meteorites now known to originate on Mars (Clayton and Mayeda 1983).

Some eucrite-type achondrites have long been known to have unusual petrological and/or compositional characteristics (e.g., Ibitira; Wilkening and Anders 1975; Stolper 1977), but nevertheless they were considered to have come from the same parent asteroid as other HEDs. Ibitira was shown to have an O-isotope composition close to those of other HED meteorites (Clayton and Mayeda 1983). In contrast, Northwest Africa (NWA) 011 was found to have an O-isotope composition very different from those of other HEDs and the requirement for a distinct parent asteroid for it was demonstrated (Yamaguchi et al. 2002). NWA 011 also plots within the carbonaceous ^{50}Ti-^{54}Cr-isotope cluster, distinct from HED meteorites in the noncarbonaceous cluster (Warren 2011). These clusters are thought to represent discrete major reservoirs of material in the solar system.

Subsequent to the pioneering work on three-O-isotope analyses undertaken by Clayton's group, a new method—laser-assisted fluorination analysis—allowed for much higher precision analyses on smaller samples and was applied to HED meteorites (Wiechert et al. 2004; Greenwood et al. 2005; Scott et al. 2009). These studies showed that Ibitira is discrepant in $\Delta^{17}O$ from the mean of other HEDs by 16–21σ (Wiechert et al. 2004; Scott et al. 2009). Wiechert et al. (2004) favored the formation of Ibitira on a heterogeneous HED asteroid, but nevertheless, recognized that it could have arisen on a distinct parent asteroid. In contrast, Greenwood et al. (2005) found that monomict and unbrecciated basaltic eucrites, cumulate eucrites, and diogenites had a narrow range in $\Delta^{17}O$ and argued that this indicated a homogeneous parent asteroid. These authors posited that the HED asteroid had been homogenized through a stage of high degree of melting (>50%). Scott et al. (2009) showed that five eucrites have $\Delta^{17}O$ values that depart from the HED igneous mean by >3σ and argued that these outlier meteorites were formed on distinct parent asteroids. Note that there is some circularity in this reasoning: Initial results suggested a homogeneous asteroid; subsequent divergent values were relegated to a different source. However, one might expect that basalts formed on an isotopically heterogeneous parent asteroid would yield a normal distribution of values about the mean. This is not what is observed. The distribution is highly skewed with all but one outlier falling between the eucrite–diogenite mean and the terrestrial fractionation line (TFL; Scott et al. 2009). This lends credence to the interpretation that the anomalous meteorites hail from distinct parent asteroids with different O-isotope compositions.

The FeO/MnO ratios of planetary basalts can also be used to fingerprint source bodies (Papike et al. 2003). Divalent Mn and Fe are homologous species and the FeO/MnO ratio is relatively invariant during most igneous processes. Provided that the oxygen fugacity is buffered, the magma FeO/MnO is inherited from the source region with little modification. Distinct parent body FeO/MnO ratios are caused by nebular fractionations that engender differences in Fe^0/Fe^{2+}, Fe^{3+}/Fe^{2+}, Fe_{total}/Mn, and/or Fe_{total}/S. However, the efficacy of the FeO/MnO ratio as a diagnostic of source body was originally demonstrated through comparison of basalts from the Earth, Moon, Mars, the HED parent asteroid (presumed to be Vesta), and the angrite parent asteroid, where large differences in pyroxene and/or olivine FeO/MnO are present (Papike et al. 2003). Modifications imposed by igneous processes are small secondary effects in comparison. Yamaguchi et al. (2002) showed that low-Ca pyroxene in NWA 011 has an FeO/MnO of ~65, roughly twice that of pyroxenes in basaltic eucrites (~31–32), supporting the conclusion from O-isotope results that it derives from a different parent asteroid. Using an electron microprobe analysis protocol that improves the precision on FeO/MnO ratios for eucritic pyroxenes, Mittlefehldt (2005) showed that low-Ca pyroxenes in Ibitira have ratios that are resolvable from those of other basaltic eucrites and argued for a separate parent asteroid for this basalt. Note, however, that although metabasalt Emmaville has a $\Delta^{17}O$ ~11σ from the HED igneous mean, it has a low-Ca pyroxene FeO/MnO indistinguishable from those of isotopically normal basaltic eucrites (Barrett et al. 2017). Thus, there is not always a correlation between O-isotope composition and anomalous FeO/MnO.

Analyses have shown that some eucrite-type basalts also have anomalous Cr-isotopic compositions, with $\varepsilon^{54}Cr$ in the range from −0.4 to −0.2, compared to the range for normal basaltic eucrites of −0.8 to −0.7 (Sanborn and Yin 2014; Sanborn et al. 2016; Benedix et al. 2017). At present, uncertainties on Cr-isotope measurements are relatively large, and fine-scale resolution among Cr-anomalous eucrite-type achondrites is not possible. Thus, Ibitira is indistinguishable from Pasamonte in $\varepsilon^{54}Cr$ (e.g., Sanborn and Yin 2014), despite being well resolved in oxygen isotope composition (Wiechert et al. 2004; Scott et al. 2009).

In order to further our understanding of relationships between anomalous O-isotope composition and petrology

of eucrite-type achondrites, we have done petrologic studies on a suite of eucrite-type achondrites, including several that have small departures in $\Delta^{17}O$ from the HED igneous mean and/or have anomalous petrologic characteristics, and on a suite of isotopically and/or petrologically normal eucrites by way of comparison. We have also done precise O-isotope analyses on a suite of eucrite-type achondrites including several that have anomalous petrologic properties based on literature descriptions and our work.

Pasamonte is a special case. It is a polymict mafic breccia composed of unequilibrated basalt clasts and contains a small amount of chondritic component possibly like H or CI chondrites (Metzler et al. 1995). The O-isotope data on Pasamonte are 5σ from the HED igneous mean (Scott et al. 2009) and are consistent with a mixture of eucritic and H chondritic materials. However, all samples analyzed have the same O-isotope composition (Wiechert et al. 2004; Greenwood et al. 2005; Scott et al. 2009), and given that sample masses were only a few mg, this is an unlikely result if the anomalous O character was caused by an impact-mixing processes. Furthermore, the Cr isotope composition of Pasamonte is inconsistent with a eucrite–H chondrite mixture (Sanborn et al. 2016). Our preliminary petrologic study of Pasamonte shows that its mafic component is derived from several distinct lithic types (Mittlefehldt et al. 2017). Our study of this complex breccia will be presented in a future paper; the petrology of Pasamonte will not be discussed here.

Asteroid 4 Vesta has long been put forth as being the parent of the HED clan of meteorites (Consolmagno and Drake 1977). Strong arguments can be made supporting this hypothesis (McSween et al. 2013), but this consensus view can be challenged for several reasons (Schiller et al. 2011; Wasson 2013). For the purposes of this study, whether Vesta is, or is not, the HED parent asteroid is of no importance.

SAMPLES AND ANALYTICAL METHODS

We have done petrologic studies of thin sections of 36 eucrite-type achondrites. We include in our discussion five other meteorites studied previously by the senior author, and Emmaville, which was analyzed at NASA Johnson Space Center using identical analytical protocols (Barrett et al. 2017). Table 1 lists these meteorites. The suite comprises six cumulate gabbros, 34 unbrecciated or monomict basalts, and mafic clasts from two polymict breccias. Of the basalts, five are Stannern group eucrites: Lewis Cliff (LEW) 88010, Pecora Escarpment (PCA) 82501, PCA 91179, Queen Alexandra Range (QUE) 94484, and Stannern. Sioux County is classified as a monomict eucrite, but petrologic evidence suggests that it is a polymict breccia (Yamaguchi et al. 1997). We separated a collection of basalt clasts from it for a study investigating the igneous components of this breccia (Mittlefehldt et al. 1998a). We also studied a thin section made from a bulk sample chip of Sioux County. The thin section includes a coarse-grained gabbro clast that is discussed here. The results on matrix grains in the thin section are not discussed. For polymict eucrite Yamato (Y-) 793164, thin section 63-3 consists of a fine-grained ferroan metabasalt (Mittlefehldt and Lindstrom 1993). Results on matrix grains from Y-793164 thin section 65-3 are not discussed.

Four of the eucrites were recently classified unbrecciated basalts and were tentatively paired: Grosvenor Mountains (GRO) 17070, GRO 17098, GRO 17200, and GRO 17210; collectively referred to as GRO 17 eucrites. We examine the pairing issue for them in the supporting information. Our conclusions are that GRO 17070 is a distinct meteorite, GRO 17098 and GRO 17200 are probably paired, while GRO 17210 is tentatively paired with the latter two.

There is a significant database of HED samples for which high-precision oxygen isotope analyses are available (Greenwood et al. 2017). However, there are as yet no unambiguous mineralogical or petrologic features that can be used to identifying those examples which have anomalous oxygen isotope compositions. We selected 19 meteorites for O-isotope analysis. Some of these were chosen based on literature descriptions that suggested some unusual petrological characteristics; others because they had not previously been analyzed. Although Elephant Moraine (EET) 92023, GRA 98098, Pasamonte, and PCA 82502 had been analyzed previously (Greenwood et al. 2009, 2012; Scott et al. 2009), we sought to examine the issue of sample heterogeneity by reanalyzing them using distinct sample fractions. EET 87520, EET 87542, and QUE 94484 were analyzed for the first time in order to determine whether they have anomalous oxygen isotope compositions. Descriptions of all of these suggested some unusual petrologic characteristics. Subsequent to the start of this project, independent samples for EET 87520 and QUE 94484 were analyzed, again for the purpose of testing for sample heterogeneity (Greenwood et al. 2017).

High-precision oxygen isotopic measurements were undertaken at The Open University (Milton Keynes, UK) using our standard procedures (e.g., Greenwood et al. [2017] and references therein). The calculation of $\Delta^{17}O$, which represents the deviation from the TFL, uses the linearized format of Miller (2002):

$$\Delta^{17}O = 1000\ln(1+(\delta^{17}O/1000)) - \lambda 1000\ln(1+(\delta^{18}O/1000)) \text{ where } \lambda = 0.5247.$$

Table 1. Meteorites included in the petrologic study.

Meteorite	Thin section	Type	Texture
Anomalous oxygen			
A-881394	52-4	Cumulate	Unbrecciated
EET 92023	14; 16	Cumulate	Unbrecciated
Emmaville[1]	BM(NH) P293; USNM 5755	Basaltic	Hornfels
Ibitira[2]	USNM	Basaltic	Unbrecciated
PCA 82502	93	Basaltic	Cataclastic breccia
PCA 91007	16	Basaltic	Cataclastic breccia
HED-normal oxygen			
BTN 00300	18	Basaltic, main group	Unbrecciated
Caldera	USNM 6394-3	Basaltic, main group	Unbrecciated
CMS 04049	23	Basaltic, main group	Unbrecciated
EET 87520	5; 17	Basaltic, main group	Unbrecciated
EET 87542	18; 19	Basaltic, main group	Brecciated
EET 90020	17	Basaltic, main group	Unbrecciated
EET 92003	6	Basaltic, main group	Brecciated
GRA 98098	15, 19; 49	Basaltic, main group	Unbrecciated
GRO 17070	10	Basaltic, main group	Unbrecciated
GRO 17098	6	Basaltic	Unbrecciated
GRO 17200[a]	9	Basaltic	Unbrecciated
GRO 17210	10	Basaltic	Unbrecciated
HOW 88401	31; 32	Basaltic, main group	Brecciated
LEW 85305	11	Basaltic, main group	Brecciated
LEW 88010	9; 12	Basaltic, Stannern	Unbrecciated
Moore County[3]	ASU	Cumulate	Unbrecciated
PCA 82501	30	Basaltic, Stannern	Unbrecciated
PCA 91179	20	Basaltic, Stannern	Brecciated
QUE 94484	11	Basaltic, Stannern	Unbrecciated
Sioux County[b]	BM(NH)	Basaltic, main group	Unbrecciated
Stannern	n/a	Basaltic, Stannern	Brecciated
Unknown oxygen			
ALH 85001	18; 27	Cumulate	Brecciated
DOM 08001	12	Basaltic, main group	Brecciated
EET 87548	15	Cumulate	Brecciated
GRO 06059	15	Basaltic, main group	Brecciated
LAR 06875	14	Basaltic, main group	Brecciated
MIL 05041	10	Basaltic, main group	Brecciated
MIL 07004	12	Basaltic, main group	Brecciated
MIL 07016	8	Basaltic, main group	Brecciated
MIL 11290	11	Basaltic, main group	Brecciated
Orlando	n/a	Basaltic, main group	Brecciated
Y-791195[4]	92-2	Cumulate	Unbrecciated
Y-792510	61-5; 91-2	Basaltic, main group	Brecciated
Y-793164[4c]	63-3; 65-3	Basaltic, main group	Hornfels
Y-82037	91-3	Basaltic, main group	Brecciated
Y-82066[4]	53-2	Basaltic, main group	Brecciated

Sources for some petrologic data: [1]Barrett et al. (2017); [2]Mittlefehldt (2005); [3]Mittlefehldt (1990); [4]Mittlefehldt and Lindstrom (1993).
[a]There are no O-isotope data for GRO 17200 but it is assumed to be normal because of probable pairing with GRO 17098; see text and supporting information.
[b]Separated basalt clasts; gabbro in thin section.
[c]Ferroan basalt clast from polymict eucrite.

Details of the analytical procedures are given in the supporting information.

Our petrologic study utilizes data from all electron microprobes in use at NASA Johnson Space Center over the last four decades. Pre-1993 mineral composition measurements were done using a Cameca Camebax electron microprobe. A Cameca SX100 electron microprobe was used exclusively between late

1992 and 2014. From late 2014, the SX100 and a JEOL JXA-8530F shared analysis duties, but most pyroxene analyses done since then utilized the JEOL probe.

Ferromagnesian silicates and oxide phases were analyzed using higher than typical accelerating potential and sample current: 20 keV and 40 nA. These conditions, plus longer than typical counting times, increase the excitation of transition elements and total counts, which result in greater precision than do analyses using more typical beam conditions and counting times (Mittlefehldt 2005). These modifications allow for theoretical 1σ analytical precision on the Fe/Mn ratio of eucritic low-Ca pyroxenes as low as ~0.8% for Ibitira (Mittlefehldt 2005). A full discussion of the electron microprobe analytical methods is given in the supporting information.

RESULTS

Oxygen Isotope Compositions

Our new results and high-precision oxygen isotope analyses from literature available for the meteorites examined in this study are given in Table 2 and plotted in Fig. 1. An O anomaly is given for each meteorite. This is the median absolute deviation about the median (MAD; Leys et al. 2013) calculated as the median of absolute deviations from the $\Delta^{17}O$ HED igneous median of Open University data (Greenwood et al. [2017] and references therein; this study). The igneous median was calculated using all non-polymict, non-impact melt eucrites and diogenites in the Open University database. We define the term "MAD unit" as an analog to σ in relation to the mean of normally distributed data. The procedure for calculating the MAD unit is described in the supporting information. Scott et al. (2009) used the mean and standard deviation of the mean to test for outliers among eucrite-type achondrites. However, this procedure assumes that the data are normally distributed, and the mean is strongly affected by outliers. The $\Delta^{17}O$ values for eucrite-type achondrites are highly skewed and not normally distributed (Fig. 1b). The sample median is a more robust statistic with which to test for and exclude outliers in such cases (e.g., Rousseeuw and Croux 1993).

The discussion here divides eucrite-type achondrites into three anomaly groups utilizing the Open University data: "normal" with $\Delta^{17}O$ within ±3 MAD units of the HED igneous median; "anomalous" with $\Delta^{17}O$ outside the ±3 MAD unit range; and "unknown" for which precise O-isotope data are lacking. The ±3 MAD unit cutoff is a very conservative limit (e.g., Leys et al. 2013) and is analogous to the >3σ departure from the mean used by Scott et al. (2009) to define those eucrite-type achondrites considered to be from different parent asteroids. Among the Stannern group basalts, none of the five that have been analyzed are anomalous (Table 1). We have calculated MAD anomalies for all igneous HEDs and ungrouped eucrite-type achondrites in the Open University database and present these in Table S1 of the supporting information.

There is an apparent systematic bias between laboratories doing precise laser-assisted fluorination analyses. For example, Greenwood et al. (2005) noted that their mean $\Delta^{17}O$ for non-polymict HED meteorites, -0.239 ± 0.007, was significantly different from that of Wiechert et al. (2004), -0.219 ± 0.004. Nine non-polymict HEDs are common between these two studies; the results of Greenwood et al. (2005) have a lower $\Delta^{17}O$. Because of this systematic bias, we rely on Open University data for evaluating whether a meteorite contains anomalous O.

Most samples display normal oxygen isotope compositions, falling within the ±3 MAD unit envelope; only a few are anomalous (Fig. 1a). We did an extensive analysis campaign on PCA 82502 and PCA 91007, which are paired meteorites (see Discussion section). This campaign is described in the supporting information. The average of all PCA 82502 samples is at +3.1 MAD units, and that of PCA 91007 is +4.3 (Table 2). Combining the data for both meteorites, we derive an O anomaly of +3.7 MAD units. However, there is variability within the individual measurements for each meteorite. Our analysis campaign on them revealed no compelling evidence for terrestrial O in these samples, and we conclude that these meteorites are moderately heterogeneous in O-isotope composition (see supporting information). Our analysis of QUE 94484 has a relatively low $\delta^{18}O$ compared to other basaltic eucrites and plots with diogenites in Fig. 1a. This may reflect a relatively high pyroxene content in the analyzed sample. Regardless, this eucrite has a normal $\Delta^{17}O$ for eucrites. Our analysis of anomalous eucrite EET 92023 (Fig. 1) is only marginally different in terms of $\Delta^{17}O$ from that of Greenwood et al. (2017) and suggests that this sample is relatively homogeneous with respect to $\Delta^{17}O$. This contrasts with anomalous eucrites Bunburra Rockhole (Benedix et al. 2017) and Dhofar 007 (Greenwood et al. 2017), which show significant levels of $\Delta^{17}O$ variation. With the notable exceptions of the NWA 011 pairing group and NWA 1240, all isotopically anomalous eucrite-type achondrites plot between the eucrite fractionation line (EFL) and angrite fractionation line (AFL). NWA 1240 is an impact melt (Barrat et al. 2003) and its O-isotope composition could reflect mixing processes. The possible

Table 2. Oxygen isotope data for new samples studied here plus Open University data for other meteorites discussed.

Meteorite	Split	*n*	Data source[a]	$\delta^{17}O$ (½)	1σ	$\delta^{18}O$ (½)	1σ	$\Delta^{17}O$ (½)$_{linear}$	1σ	$\Delta^{17}O$ anomaly (MAD units)[b]
Anomalous eucrite-type achondrites and diogenite Dhofar 778										
A-881394		6	3	1.912	0.036	3.882	0.084	−0.122	0.015	16.0
Bunburra Rockhole		42	5	1.959	0.058	3.992	0.104	−0.134	0.020	15.3
Dhofar 007		11	4	1.832	0.177	3.806	0.306	−0.163	0.024	10.6
Dhofar 778		4	4	2.024	0.019	4.167	0.068	−0.160	0.027	11.0
EET 92023	,26	2	1	1.948	0.050	3.929	0.087	−0.112	0.005	–
		4	4	1.881	0.044	3.821	0.097	−0.122	0.018	–
	ave	6		1.903	0.054	3.857	0.101	−0.119	0.015	16.5
Emmaville		5	4	1.993	0.036	4.069	0.093	−0.139	0.016	–
		8	6	2.032	0.168	4.168	0.298	−0.153	0.015	–
	ave	13		2.017	0.132	4.130	0.239	−0.148	0.016	12.6
Ibitira		6	3, 4[c]	1.960	0.021	3.878	0.045	−0.073	0.015	22.5
NWA 1240		4	3	1.324	0.057	3.043	0.106	−0.271	0.007	−3.8
Pasamonte		2	1	1.857	0.064	3.929	0.113	−0.202	0.004	–
Pasamonte		23	4	1.778	0.052	3.785	0.098	−0.205	0.011	–
Pasamonte	ave	25		1.785	0.056	3.796	0.105	−0.205	0.011	5.0
PCA 82502—untreated[d]	,106	4	1	1.748	0.051	3.757	0.089	−0.222	0.005	–
EATG residue	,106	2	1	1.763	0.040	3.782	0.083	−0.219	0.004	–
untreated	,89	3	4	1.734	0.022	3.720	0.050	−0.216	0.017	–
EATG residue	,89	1	4	1.720	–	3.708	–	−0.223	0.000	–
	ave	10		1.744	0.037	3.746	0.069	−0.220	0.009	3.1
PCA 91007—untreated[d]	,2	5	1, 3	1.740	0.073	3.713	0.140	−0.207	0.014	–
HCL residue	,2	2	3	1.766	0.001	3.767	0.033	−0.208	0.016	–
EATG residue	,2	2	1	1.670	0.150	3.613	0.288	−0.224	0.001	–
	ave	9		1.730	0.082	3.703	0.153	−0.211	0.014	4.3
PCA pair	ave	19		1.737	0.061	3.725	0.115	−0.215	0.012	3.7
Basaltic and cumulate eucrites										
Moore County		5	2	1.677	0.078	3.665	0.163	−0.244	0.017	−0.1
BTN 00300	,23	2	4	1.633	0.020	3.580	0.026	−0.243	0.006	0.0
Caldera		2	3	1.804	0.020	3.911	0.030	−0.246	0.004	−0.3
CMS 04049		2	4	1.799	0.024	3.891	0.049	−0.240	0.002	0.4
EET 87520		2	4	1.658	0.024	3.630	0.036	−0.244	0.005	–
	,30	4	1	1.766	0.009	3.825	0.035	−0.239	0.013	–
	ave	6		1.730	0.057	3.760	0.106	−0.241	0.010	0.3
EET 87542	,14	2	1	1.861	0.008	4.003	0.023	−0.237	0.004	0.8
EET 90020	,48	2	3	1.690	0.047	3.689	0.098	−0.244	0.004	−0.1
EET 92003	,24	2	1	1.757	0.045	3.810	0.069	−0.240	0.009	0.5
Basaltic and cumulate eucrites										
EET 92004	,8	2	1	1.729	0.051	3.768	0.088	−0.246	0.005	−0.3
GRA 98098	,53	2	3	1.679	0.007	3.640	0.022	−0.229	0.019	–
	,67	4	1	1.731	0.045	3.739	0.086	−0.229	0.014	–
	ave	6		1.714	0.044	3.706	0.085	−0.229	0.013	1.9
GRO 95533	,8	2	1	1.637	0.007	3.602	0.013	−0.251	0.000	–
	,15	2	1	1.726	0.006	3.786	0.002	−0.258	0.005	–
	ave	4		1.681	0.051	3.694	0.107	−0.255	0.005	−1.5
GRO 17070	,6	2	1	1.836	0.050	3.967	0.091	−0.244	0.003	−0.1
GRO 17098	,7	2	1	1.734	0.033	3.768	0.066	−0.241	0.002	0.3
GRO 17210	,6	2	1	1.625	0.016	3.554	0.027	−0.238	0.001	–
	,11	2	1	1.564	0.025	3.389	0.045	−0.212	0.002	–
	ave	4		1.595	0.039	3.472	0.100	−0.225	0.015	2.4
HOW 88401	,48	2	1	1.556	0.144	3.431	0.266	−0.242	0.005	0.1
LEW 85305		2	4	1.711	0.009	3.710	0.000	−0.234	0.009	1.2

Table 2. *Continued*. Oxygen isotope data for new samples studied here plus Open University data for other meteorites discussed.

Meteorite	Split	*n*	Data source[a]	$\delta^{17}O$ (½)	1σ	$\delta^{18}O$ (½)	1σ	$\Delta^{17}O$ (½)$_{linear}$	1σ	$\Delta^{17}O$ anomaly (MAD units)[b]
LEW 88010	,8	2	1	1.763	0.033	3.842	0.073	−0.251	0.005	–
LEW 88010	,10	2	1	1.697	0.030	3.711	0.040	−0.248	0.009	–
	ave	4		1.730	0.046	3.776	0.089	−0.249	0.006	−0.8
MAC 02522	,8	2	1	1.640	0.101	3.607	0.200	−0.251	0.004	−1.0
PCA 82501	,13	2	1	1.675	0.042	3.661	0.082	−0.244	0.001	−0.1
PCA 91179	,21	2	1	1.654	0.033	3.612	0.058	−0.240	0.003	0.4
PCA 91245	,5	2	1	1.700	0.014	3.696	0.018	−0.237	0.005	–
	,15	2	1	1.621	0.013	3.554	0.022	−0.242	0.002	–
	ave	4		1.660	0.047	3.625	0.084	−0.240	0.004	0.5
QUE 94484[e]	,4	3	4	1.395	0.028	3.138	0.077	−0.250	0.015	–
	,4	1	4	1.717	0.000	3.744	0.000	−0.245	0.000	–
	,12	4	1	1.546	0.125	3.423	0.231	−0.249	0.006	–
	ave	8		1.511	0.139	3.356	0.263	−0.249	0.009	−0.7
Sioux County		2	2	1.806	0.039	3.891	0.101	−0.234	0.014	1.3
Stannern		2	2	1.749	0.026	3.803	0.068	−0.245	0.009	−0.2

[a]Data sources: 1—this study; 2—Greenwood et al. (2005); 3—Scott et al. (2009); 4—Greenwood et al. (2017); 5—Benedix et al. (2017); 6—Barrett et al. (2017).

[b]$\Delta^{17}O$ deviation from igneous median expressed in median absolute deviation (MAD) units; see text and supporting information.

[c]These data are given as from Wiechert et al. (2004) in table 6 of Greenwood et al. (2017) but are in fact combined data from the sources listed here.

[d]Analyses from this study and Greenwood et al. (2017) included splits that are untreated, HCl-treated residues and EATG-treated residues to evaluate Antarctic alteration; see text and supporting information.

[e]Sample from Greenwood et al. (2017) (,4) was untreated (3 replicates) and a single EATG treated split; that from this study (,12) was untreated.

reason for the skewed distribution is covered in the Discussion section.

Petrology

The full mineral composition data sets for all meteorites are presented in a single file hosted by the Astromaterials Data Repository (Mittlefehldt 2021). Data summaries for Emmaville are given in Barrett (2018) and Barrett et al. (2017), but the full data set was not published. We include these data in the data set.

The supporting information describes the procedures used for quality control on the data set. Quality control used automatic filters (analysis total; stoichiometry) that are identical for all meteorites, and interactive filters applied by DWM to each meteorite/phase while examining the data. The data presented in the full data set include analyses labeled as "normal" that passed all filters, and "anomalous" that were flagged during examination of the data because they showed some small deviations from most of the data. These latter could be due to either real variations within phases, or analytical artifacts, for example, caused by secondary fluorescence of minute inclusions. Mineral analyses were done in automatic mode, with analysis locations selected and stored, and then analyzed in sequence. Minute inclusions could have been unintentionally included within the activation volume of the electron beam.

Summaries of mineral compositional characteristics for pyroxene, plagioclase, and oxide phases are presented in Tables 3–5. These characteristics are derived only from analyses labeled "normal" in the data set. Olivine was not systematically analyzed because it is present only as a minor phase in some of the meteorites and absent from most. The olivine characteristics in Table S3 in the supporting information are derived from opportunistic analyses of grains that were within regions of interest targeted for pyroxene analyses. Metal compositions for EET 87542, EET 92023, and Queen Alexandra Range (QUE) 94484 are given in Table S4 in the supporting information. The first two are unusually rich in metal, the latter in troilite.

An important parameter discussed here is the low-Ca pyroxene Fe/Mn ratio, but definitions for low- and high-Ca compositional limits are challenging. Liquidus pyroxenes in eucrites were Mg-pigeonite, which evolved

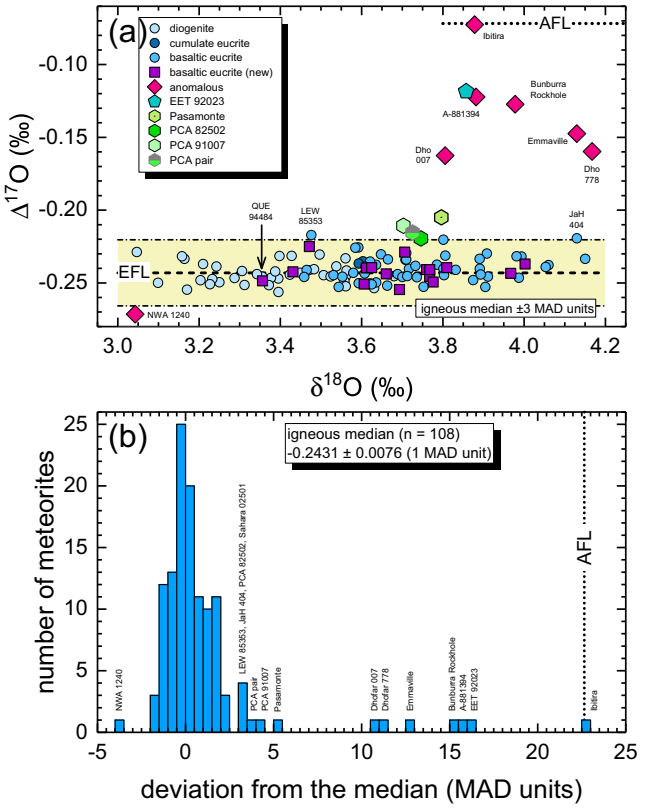

Fig. 1. Oxygen isotope data for eucrite-type achondrites and diogenites: (a) $\Delta^{17}O$ (linearized, $\lambda = 0.5247$) versus $\delta^{18}O$ highlighting new data; and (b) histogram of deviations from the HED igneous median in median absolute deviation (MAD) units (see text). EFL (eucrite fractionation line) = HED igneous median; AFL = angrite fractionation line. Labeled meteorites are outliers that are >3 MAD units from the HED igneous median (see text). Color versions of all figures are available online and in the pdf version.

to Fe-augite as crystallization progressed (e.g., Stolper 1977; Takeda and Graham 1991). However, most eucrites have been metamorphosed with consequent homogenization of pyroxene Fe/Mg and exsolution of augite from host pigeonite and pigeonite from host augite (Takeda and Graham 1991). The resulting exsolution texture resulted in some intermediate composition analyses due to beam overlap on both pyroxenes, causing challenges in defining low- and high-Ca compositional ranges. The general procedure used to set pyroxene endmember limits is described in the supporting information and shown graphically in mineral composition diagrams for all samples that are contained in a single file hosted by the Astromaterials Data Repository (Mittlefehldt 2021).

Because of the long time span over which the analyses were done, differences in the standard set used, and the multiple instruments used, some systematic instrumental biases are present in the data set. These potential biases are explored in detail in the supporting information. Any systematic biases in the data set would impact our ability to come to firm petrologic conclusions for some of the differences in Fe/Mn we observe. The potential issues engendered by systematic biases are also considered in the Discussion section as needed. The pyroxene data shown in Table 3 represent averages for each meteorite. Multiple average compositions are shown for some meteorites for which distinctly different compositions are present in different grains. These latter are due to real pyroxene variability and not analytical biases as they are determined within individual analysis sessions.

The low-Ca pyroxene Fe/Mn versus Fe/Mg data (Table 3) are shown in Fig. 2 and are compared to mafic clasts from mesosiderites (Mittlefehldt 1990). Most basalt and gabbro clasts in mesosiderites are secondary, the product of remelting of the primary crust after metal–silicate mixing (e.g., Mittlefehldt 1979, 1990; Rubin and Mittlefehldt 1992). Interaction of remelted silicates with the admixed metal and troilite caused reduction of FeO from the silicate system, resulting in low-Ca pyroxenes with low Fe/Mn compared to those of eucrites, and low Fe/Mg for basaltic clasts compared to those of basaltic eucrites (Fig. 2a) (Mittlefehldt 1990). Two isotopically normal basaltic eucrites include low-Ca pyroxenes that have Fe/Mn much lower than those of mesosiderite mafic clasts: all pyroxenes in equilibrated, metal-rich brecciated basalt EET 87542; and ferroan pigeonite rims in unequilibrated, unbrecciated fine-grained basalt QUE 94484. Pyroxenes in EET 87542 have the lowest mean Fe/Mn determined for eucrites and are also more magnesian than typical for basaltic eucrites (Figs. 2a and 3a). Magnesian low-Ca pyroxene cores in QUE 94484 have compositional characteristics of low-Ca pyroxenes in Mg-rich cumulate eucrites (Fig. 2b). Pyroxenes in this meteorite show continuous zoning from these low-Ca, magnesian cores through ferroan augites with $Wo_{\sim 30}$, but there are few analyses between these augites and a cluster with $Wo_{\sim 40\text{-}45}$ (Fig. 3b). Internal variations in pyroxene Fe/Mn in this meteorite were first documented by Mayne et al. (2009).

Two basaltic eucrites have unusual low-Ca pyroxene compositions compared to others. Miller Range (MIL) 11290 is a fine-grained, unbrecciated ferroan basalt. Its pyroxene compositions show some similarity to the distribution characteristic of type 3 eucrites of Takeda and Graham (1991), except that pyroxenes intermediate between the magnesian and ferroan low-Ca pyroxenes are not present (Fig. 3c). Most analyses are more ferroan than Sioux County basalt clast pyroxenes. Magnesian

Table 3. Pyroxene compositional parameters for eucrite-type achondrites: Fe/Mg, Fe/Mn—mole ratio; Wo—mole %.

	Low-Ca pyroxene						High-Ca pyroxene						
	n	Wo	Fe/Mg		Fe/Mn		*n*	Wo	Fe/Mg		Fe/Mn		
Meteorite		Ave	Ave	Std	Ave	Std		Ave	Ave	Std	Ave	Std	Notes
Cumulate gabbro, eucrite, and anomalous													
A-881394	92	3.00	0.809	0.011	30.22	0.33	25	42.7	0.460	0.007	25.96	0.35	
ALH 85001	627	2.08	0.525	0.011	28.34	0.42	314	44.3	0.302	0.017	22.11	0.63	
EET 87548	107	1.82	0.828	0.016	28.52	0.50	33	44.5	0.439	0.012	24.45	0.42	
EET 92023	52	4.92	1.057	0.028	32.60	0.66	8	39.0	0.671	0.011	31.68	0.30	Type a
	11	6.30	0.750	0.021	30.44	0.35	–	–	–	–	–	–	Type b
Moore County*	99	5.62	1.015	0.021	30.00	0.50	114	41.8	0.629	0.017	29.12	0.74	Type a
	25	4.82	0.967	0.021	33.24	0.48	10	41.8	0.644	0.011	30.14	0.52	Type b
Y-791195*	50	5.24	1.351	0.011	30.64	0.49	20	42.5	0.782	0.009	30.90	0.59	
Basalt, main group eucrite, and anomalous													
BTN 00300	49	6.54	1.627	0.029	31.20	0.23	10	40.3	1.074	0.006	32.29	0.30	
Caldera	65	5.10	1.506	0.020	30.27	0.23	21	40.1	0.958	0.017	31.17	0.42	
CMS 04049	265	5.22	1.535	0.052	30.18	0.26	235	41.5	0.953	0.046	32.07	0.51	Type a
	35	2.70	1.408	0.014	33.64	0.25	–	–	–	–	–	–	Type b
DOM 08001	63	1.84	1.652	0.058	31.28	0.95	35	42.8	0.883	0.025	30.50	0.61	
EET 87520	425	6.46	1.546	0.030	29.55	0.42	154	40.3	0.959	0.014	30.37	0.55	Camebax data excluded
EET 87542	305	6.16	1.055	0.042	18.56	0.47	76	39.3	0.673	0.027	17.72	0.64	
EET 90020	59	4.67	1.727	0.024	31.58	0.28	16	41.1	1.039	0.018	31.49	0.53	
EET 92003	5	7.61	1.000	0.016	32.22	0.52	1	28.8	1.084	–	28.75	–	Magnesian
	4	16.36	1.911	0.054	30.91	0.61	–	–	–	–	–	–	Ferroan
Emmaville*	73	2.04	1.767	0.070	31.57	0.65	46	43.5	0.898	0.016	31.41	0.33	
GRA 98098	49	5.72	1.560	0.041	31.43	0.34	4	38.0	1.082	0.036	30.84	0.40	
GRO 06059	88	5.78	1.662	0.024	31.49	0.25	14	41.1	0.975	0.019	33.51	0.51	Type a
	149	3.19	1.541	0.025	35.02	0.33	–	–	–	–	–	–	Type b
GRO 17070	61	5.11	1.767	0.023	30.71	0.24	10	41.6	1.019	0.022	32.88	0.36	Type a
	2	2.91	1.691	–	34.48	–	–	–	–	–	–	–	Type b
GRO 17098	69	1.72	1.555	0.040	31.89	0.35	18	43.7	0.840	0.022	30.64	0.41	
GRO 17200	74	1.67	1.560	0.029	31.90	0.33	9	43.6	0.837	0.016	30.70	0.49	
GRO 17210	104	1.73	1.449	0.074	32.29	0.47	4	43.8	0.821	0.054	31.23	0.34	
Basalt, main group eucrite, and anomalous													
HOW 88401	44	2.13	1.594	0.064	32.17	1.14	9	43.6	0.885	0.039	30.72	0.54	
Ibitira*	30	4.50	1.428	0.015	36.45	0.29	13	38.6	0.950	0.012	34.69	0.76	
LAR 06875	63	1.98	1.695	0.044	32.19	0.58	24	42.9	0.884	0.018	32.19	0.59	
LEW 85305	51	8.69	1.741	0.048	32.94	0.48	8	34.1	1.380	0.047	33.25	0.69	
MIL 05041	78	2.42	1.804	0.080	30.99	0.87	34	42.6	0.953	0.047	32.06	0.68	
MIL 07004	77	1.92	1.721	0.037	32.13	0.48	14	43.2	0.889	0.023	32.23	0.36	
MIL 07016	28	4.47	2.077	0.096	31.23	0.39	2	38.6	1.386	–	34.54	–	
MIL 11290	4	6.91	0.599	0.002	29.46	0.66	12	40.4	1.359	0.040	33.17	0.56	Magnesian
	4	3.96	2.314	0.023	30.68	0.13	–	–	–	–	–	–	Ferroan
Orlando	49	1.82	1.777	0.035	31.83	0.55	23	43.2	0.962	0.026	31.01	0.49	Type a
	9	2.32	1.881	0.025	29.41	0.35	–	–	–	–	–	–	Type b
PCA 82502	48	4.73	1.704	0.076	33.04	0.37	–	–	–	–	–	–	
PCA 91007	119	4.19	1.717	0.090	33.32	0.53	5	27.4	1.411	0.036	32.72	0.25	
Sioux County	477	2.18	1.624	0.036	30.22	0.70	56	42.8	0.924	0.029	29.49	0.89	Basalt clasts
	50	1.89	1.522	0.138	31.06	0.49	36	43.4	0.895	0.021	30.80	0.56	Gabbro clast; type a
	10	1.98	1.566	0.012	28.85	0.24	13	43.5	0.797	0.026	28.86	0.48	Gabbro clast; type b

Table 3. *Continued*. Pyroxene compositional parameters for eucrite-type achondrites: Fe/Mg, Fe/Mn—mole ratio; Wo—mole%.

	Low-Ca pyroxene						High-Ca pyroxene						
	n	Wo	Fe/Mg		Fe/Mn		*n*	Wo	Fe/Mg		Fe/Mn		
Meteorite		Ave	Ave	Std	Ave	Std		Ave	Ave	Std	Ave	Std	Notes
Y–792510	55	2.08	1.689	0.054	31.29	0.66	51	44.0	0.894	0.028	31.08	0.57	
Y-793164*	47	9.70	2.034	0.063	32.32	0.43	27	23.1	1.753	0.109	32.94	0.65	
Y-82037	70	9.42	1.452	0.026	30.85	0.22	56	37.1	1.064	0.018	30.56	0.47	
Y-82066*	33	2.80	1.379	0.037	33.62	0.65	44	42.2	0.888	0.017	30.77	0.59	
Basalt; Stannern group													
LEW 88010	123	1.67	1.392	0.034	33.30	0.64	12	42.7	0.783	0.041	33.40	1.51	
PCA 82501	86	4.12	1.524	0.064	32.11	1.28	7	40.9	0.915	0.021	32.41	0.39	
PCA 91179	132	4.56	1.495	0.016	31.94	0.49	23	41.1	0.902	0.019	32.62	0.44	
QUE 94484	15	5.78	0.491	0.004	28.60	0.44	–	–	–	–	–	–	Magnesian
	3	21.3	1.569	0.010	21.92	0.11	9	43.8	1.233	0.061	29.89	0.61	Ferroan
Stannern	77	1.63	1.667	0.030	31.85	0.39	13	43.9	0.888	0.020	31.77	0.59	

*Data from literature; see Table 1 for sources.

and ferroan low-Ca pyroxenes in MIL 11290 have indistinguishable Fe/Mn despite being the second-most magnesian and most ferroan low-Ca pyroxenes from this study (Fig. 2c). EET 92003 is a fine-grained, unequilibrated, brecciated basalt with an unusual distribution of pyroxene compositions (Fig. 3d) that do not match any of the defined pyroxene composition types (Takeda and Graham 1991; Yamaguchi et al. 1996). Most of the pyroxene is pigeonite with a mean composition of $Wo_{12.4}En_{39.0}Fs_{48.6}$ and mg# 44.5; compositions vary from $Wo_{7.6}En_{46.2}Fs_{46.2}$ and mg# 50.0, to $Wo_{16.4}En_{28.7}Fs_{54.9}$ and mg# 34.4 (mg# = molar 100 × MgO/[MgO + FeO]) (Fig. 2c). Absent from EET 92003 are the low-Ca, magnesian pyroxenes with compositions of $Wo_{5-7}En_{64-66}Fs_{\sim 29}$ that typify pyroxene cores in type 1–3 eucrites (Takeda and Graham 1991).

Five basaltic eucrites have low-Ca pyroxenes with two distinct populations in Fe/Mn: Cumulus Hills (CMS) 04049, GRO 06059, GRO 17070, Orlando, and a gabbro clast in Sioux County (Fig. 2d); these are given separate entries in Table 3. In all cases, the population with the lower Fe/Mn has a higher Fe/Mg. The gabbro clast from Sioux County was small relative to the grain size and only a few pyroxene grains were measured. For the others, individual analysis spots in numerous randomly selected grains show that one population dominates, constituting 80–97% of random analyses; these are referred to as type-a pyroxene. Moore County cumulate eucrite and EET 92023 anomalous cumulate gabbro also contain two pyroxene populations (Table 3; Fig. 2b).

Plagioclase compositional ranges of eucrite-type achondrites exhibit variable characteristics, but there is only imperfect correlation with type. Many eucrite-type achondrites have extensive compositional ranges with smoothly increasing Or with Ab (GRA 98098; Fig. 4a). A two-degree polynomial fit to the GRA 98098 data (solid curve) encompasses all analyses within ±0.25 mole % Or bounding curves (dotted curves). A few eucrite-type achondrites have smoothly varying Or and Ab contents, but with a greater increase in Or with Ab at high Ab contents compared to the GRA 98098 trend (MIL 11290; dashed line in Fig. 4a). Plagioclase grains in cumulate gabbros generally show limited ranges in composition, but EET 92023 is an exception (Table 4; Fig. 4b). Metamorphic, granoblastic-textured basalts Bates Nunataks (BTN) 00300 and Ibitira (Mittlefehldt 2005) have limited ranges in Ab and Or contents similar to those of cumulate eucrites, but metamorphic, fine-grained granular textured basalts (hornfels) Emmaville (Barrett et al. 2017) and a basaltic clast from Y-793164 (Mittlefehldt and Lindstrom 1993) have wider ranges (Table 4). Some coarse-grained igneous textured basalts have restricted ranges in Ab and Or similar to those of cumulate gabbros (e.g., Caldera, Y-82037), but others like EET 87520 do not (Table 4).

Some eucrite-type achondrites contain plagioclase grains that have regions of anomalously high K contents compared to smooth trends exhibited by most analyses. High-K analyses for each meteorite are defined as being >0.25 mole% Or above a polynomial fit for that meteorite. For example, the preponderance of plagioclase analyses from Sioux County basaltic clasts has a well-constrained relationship between Or and Ab that follow the GRA 98098 trend, but ~8% of the analyses have K contents higher than the +0.25 mole% Or bounding curve (Fig. 4a). Some of those analyses at high Ab contents roughly parallel, but at higher Ab, the trend exhibited by

Table 4. Plagioclase compositional parameters for eucrite-type achondrites, in mole%.

			An		Ab		Or	
Meteorite	n[a]	High-K[b]	max	ΔAn[c]	ave[a]	ΔAb[c]	ave[a]	ΔOr[c]
Cumulate gabbro, eucrite, and anomalous								
A-881394	67	0.0%	98.5	0.79	1.82	0.79	0.08	0.16
ALH 85001	172	0.0%	93.7	3.06	7.51	3.01	0.25	0.24
EET 87548	174	0.0%	93.4	4.19	8.86	4.07	0.19	0.27
EET 92023	109	9.2%	94.1	18.4	9.90	17.0	0.37	1.87
Moore County[d]	147	0.0%	93.8	2.90	7.55	2.71	0.28	0.24
Y-791195[d]	33	2.9%	91.8	2.03	8.84	1.94	0.35	1.29
Basalt, main group eucrite, and anomalous								
BTN 00300	49	0.0%	90.5	2.42	10.2	2.40	0.36	0.16
Caldera	67	0.0%	91.1	2.74	10.3	2.62	0.36	0.21
CMS 04049	219	8.4%	93.8	20.4	15.6	20.4	0.89	4.83
DOM 08001	76	9.5%	91.2	16.8	13.3	15.2	0.64	2.57
EET 87520	189	0.0%	90.7	5.83	10.6	5.45	0.48	0.45
EET 87542	61	9.0%	92.1	16.6	15.2	15.3	0.76	1.33
EET 92003	170	5.0%	94.3	13.9	9.89	14.0	0.33	1.96
Emmaville[d]	119	0.0%	93.1	9.33	11.3	8.82	0.36	0.54
GRA 98098	316	0.0%	92.9	28.2	11.7	25.9	0.60	2.43
GRO 06059	88	5.4%	93.3	15.4	13.8	14.4	0.64	2.76
GRO 17070	50	29.6%	94.7	21.6	14.1	20.2	0.68	6.45
GRO 17098	42	47.5%	90.1	10.8	14.6	12.5	0.69	3.00
GRO 17200	39	51.9%	93.5	12.7	13.2	16.5	0.56	3.05
GRO 17210	57	32.1%	90.3	10.6	14.7	10.5	0.60	5.67
Ibitira[d]	51	0.0%	96.2	2.20	4.73	2.13	0.28	0.21
LAR 06875	58	3.3%	91.6	8.27	11.6	7.84	0.41	0.56
MIL 05041	62	1.6%	90.6	8.17	10.5	8.77	0.39	19.0
MIL 07004	44	0.0%	91.7	5.93	12.0	5.74	0.45	0.37
MIL 07016	45	6.3%	91.4	13.1	14.9	12.0	0.81	1.16
MIL 11290	46	16.4%	91.0	11.0	15.1	12.5	0.94	1.97
Orlando	92	3.2%	92.4	10.8	12.2	10.2	0.48	1.52
Orlando[e]	4	n/a	n/a	n/a	17.1	n/a	0.44	n/a
PCA 82502	48	17.2%	95.0	15.4	10.7	15.2	0.57	1.64
PCA 91007	40	4.8%	96.8	14.9	11.0	13.9	0.48	1.23
Sioux County[f]	330	7.8%	93.2	14.9	10.4	17.7	0.40	4.83
Y-792510	71	6.6%	89.4	10.9	13.2	9.90	0.67	1.01
Y-793164[d]	12	29.4%	88.8	7.25	13.0	9.38	0.61	1.15
Y-82037	61	0.0%	91.0	1.90	9.16	1.83	0.49	0.27
Y-82066[d]	33	0.0%	94.6	5.41	6.95	5.28	0.27	0.43
Basalt, Stannern group								
LEW 88010	15	55.9%	84.2	10.8	20.3	12.0	1.04	5.80
PCA 82501	90	37.9%	87.7	10.1	17.8	9.24	0.99	12.1
PCA 91179	222	9.8%	86.6	10.6	17.2	9.79	0.83	30.8
QUE 94484	55	5.2%	86.6	8.22	15.9	7.91	1.17	1.63
Stannern	66	35.9%	87.4	12.3	19.0	12.2	0.94	18.8

[a]Averages excluding high-K and low-K analyses; n = number of analyses averaged.
[b]Percentage of high-K analyses.
[c]Maximum–minimum contents; for An, high-K and low-K analyses are excluded.
[d]Data from literature; see Table 1 for sources.
[e]Low-K plagioclase averaged separately.
[f]Separated basalt clasts.

the high-Ab, high-Or analyses from MIL 11290 (dash-dot line; Fig. 4a). The average Ab and Or contents given in Table 4 exclude high-K analyses. For Orlando, a single grain with anomalously low-K analyses was also excluded, and a single low-K analysis was excluded from the PCA 91179 average. The ranges given include all analyses.

Table 5. Oxide phase compositional parameters for eucrite-type achondrites; Fe/Mg and Fe/Mn—mole ratios; Usp —mole%.

	Ilmenite			Chromite				
Meteorite	*n*	Fe/Mg Ave	Fe/Mn Ave	*n*	Usp Range	Al/Cr Ave	Fe/Mg Ave	Fe/Mn Ave
Cumulate gabbro, eucrite, and anomalous								
A-881394	–	–	–	40	5.93–10.3	0.268	12.2	54.9
ALH 85001	17	8.66	41.4	147	2.18–7.87	0.254	9.78	50.8
EET 87548	15	14.5	40.0	215	6.61–11.5	0.255	16.6	51.7
EET 92023	12	22.1	40.7	15	12.7–30.2	0.228	29.2	50.8
Y-791195[a]	4	18.5	49.2	30	18.6–43.8	0.192	69.1	24.1
Basalt, main group eucrite, and anomalous								
BTN 00300	22	18.3	55.8	24	42.0–54.1	0.192	24.8	75.9
	–	–	–	7	6.05–7.01	0.143	18.0	75.8
Caldera	46	20.6	53.2	113	19.9–39.5	0.227	23.3	69.2
CMS 04049	247	23.6	51.9	19	18.3–23.5	0.250	31.5	56.2
DOM 08001	36	44.8	46.6	5	7.54–17.2	0.236	58.1	50.1
EET 87520	34	18.4	53.4	126	14.9–52.1	0.218	21.1	69.4
EET 87542	215	24.2	27.8	48	9.18–14.8	0.253	23.4	36.6
EET 90020	7	43.7	62.5	53	24.8–57.0	0.226	53.1	85.2
EET 92003	44	37.6	44.0	56	4.34–18.2	0.292	42.2	55.7
Emmaville[a]	16	47.1	48.8	39	7.23–29.7	0.222	49.0	51.9
GRA 98098	154	29.6	59.0	206	41.7–72.3	0.303	40.9	79.9
GRO 06059	188	21.5	54.7	73	10.1–35.7	0.221	23.4	58.5
GRO 17070	33	28.7	50.7	34	18–7–21.4	0.239	29.2	63.5
GRO 17098	53	49.1	46.8	7	6.65–7.70	0.264	46.5	59.1
GRO 17200	82	52.6	46.9	1	9.24	0.188	50.4	55.7
GRO 17210	78	43.8	47.3	39	13.0–8.72	0.473	20.3	63.0
Basalt, main group eucrite, and anomalous								
Ibitira[a]	46	18.5	67.9	59	5.93–10.3	0.295	30.1	93.8
LAR 06875	141	33.2	49.1	82	5.93–10.3	0.191	48.5	55.1
MIL 05041	43	46.8	45.3	13	9.11–43.5	0.233	42.6	52.1
MIL 07004	105	47.6	47.8	123	6.67–45.8	0.207	48.3	61.5
MIL 07016	110	46.4	47.5	8	8.17–8.43	0.392	26.6	53.8
MIL 11290	156	49.6	45.4	–	–	–	–	–
Orlando	120	50.4	46.6	49	6.33–55.9	0.170	65.7	55.3
PCA 82502	132	37.4	50.0	5	9.22–13.9	0.278	28.8	53.9
PCA 91007	382	39.9	49.9	18	8.67–15.0	0.259	37.4	53.0
Sioux County[b]	135	48.8	43.9	119	5.17–25.2	0.245	48.6	55.3
Sioux County[c]	122	40.0	44.5	–	–	–	–	–
Y-792510	117	49.9	46.4	69	7.29–22.5	0.241	53.9	61.2
Y-793164[a]	12	51.4	49.9	–	–	–	–	–
Y-82037	38	43.5	45.6	27	23.8–35.0	0.215	52.8	64.4
Y-82066[a]	10	31.4	48.1	–	–	–	–	–
Basalt, Stannern group								
LEW 88010	30	33.5	48.2	–	–	–	–	–
PCA 82501	304	23.0	45.0	4	9.83–11.5	0.225	22.8	47.8
PCA 91179	381	27.7	51.6	61	9.89–15.1	0.225	26.2	56.2
QUE 94484	74	28.0	34.9	66	1.99–23.7	0.279	21.9	44.3
Stannern	150	52.6	46.1	–	–	–	–	–

[a]Data from literature; see Table 1 for sources.
[b]Separated basalt clasts.
[c]Gabbro clast in thin section; see text.

High-K analyses are rare in cumulate gabbros; none were found in four of the six studied. One analysis from ferroan cumulate Y-791195 contained ~1.5 mole% Or, whereas all other analyses contained <0.5 mole% (Fig. 4b). EET 92023 is unique among the cumulate gabbros in that roughly 9% of plagioclase analyses are

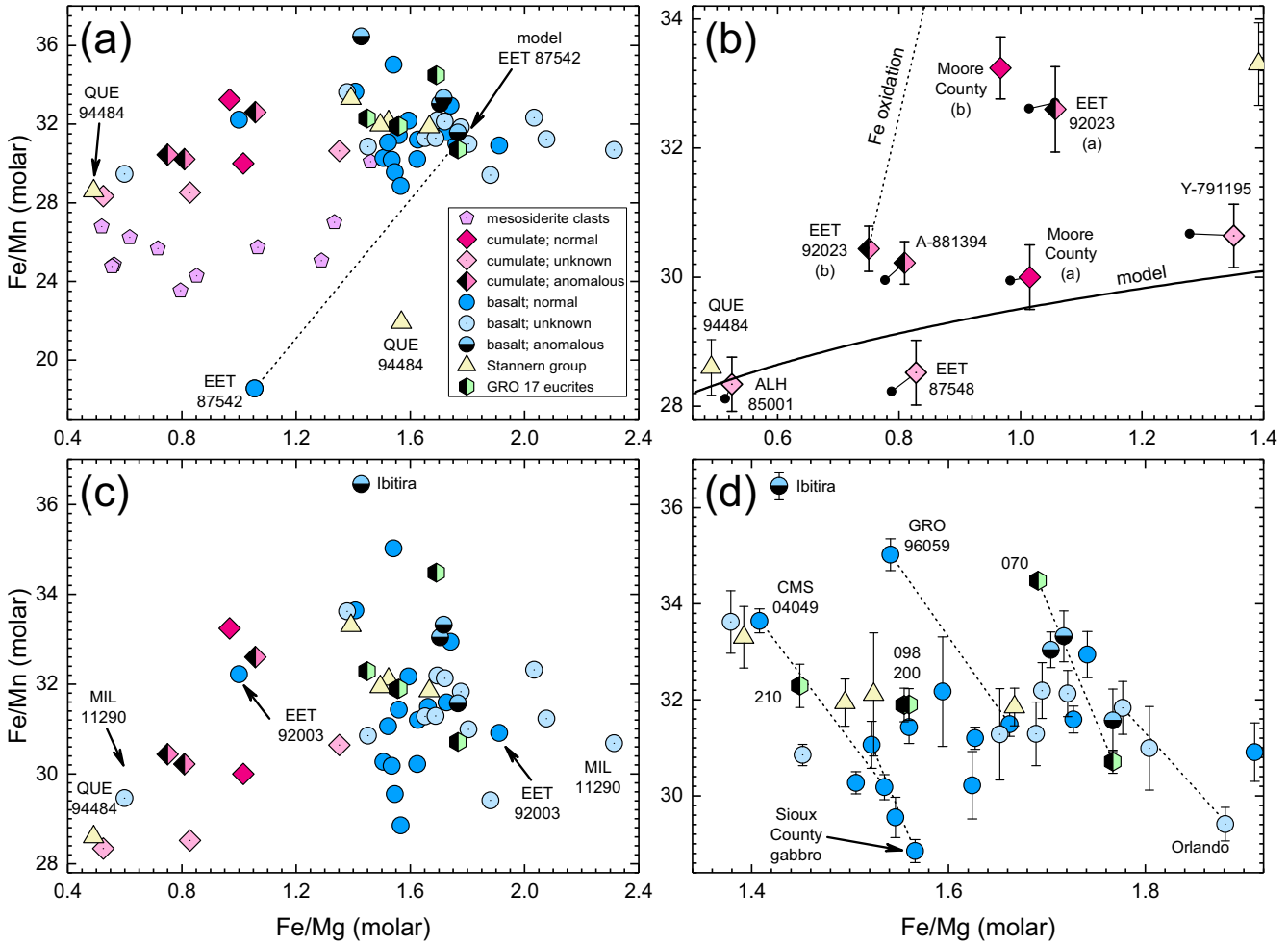

Fig. 2. Molar Fe/Mn versus Fe/Mg for low-Ca pyroxenes of eucrite-type achondrites taken from Table 3, showing: (a) all data compared to mafic clasts from mesosiderites, (b) cumulate gabbros, (c) expanded ordinate excluding pyroxenes with very low Fe/Mn, and (d) expanded axes focusing on five basalts that contain distinct populations of low-Ca pyroxene (tie lines). Normal, unknown, and anomalous refer to O-isotope anomalies as determined by Open University data (Table 1). In (a), "model EET 87542" is low-Ca pyroxene for this meteorite corrected for the effects of FeO reduction. In (b), "Fe oxidation" is a model for addition to type-b pyroxene of $FeSiO_3$ derived from oxidation of metal and reaction with silica; "model" is a semiquantitative pyroxene fractionation track from a basaltic eucrite; black dots connected to meteorite symbols are estimated bulk pyroxene compositions for the cumulates. See text for details. The GRO 17 eucrites are identified by the last three digits of their names. Mesosiderite data are from Mittlefehldt (1990).

high-K, with Or contents up to 2 mole% (Table 4; Fig. 4b).

High-K analyses are especially common (>10%) in nine of the basaltic meteorites (Table 4). Generally, most of the high-K analyses are from the high-Ab tails of the Or-Ab distributions as in the case of main group eucrite MIL 11290 (Fig. 4a). Three of the nine are Stannern group eucrites, and the distributions of high-K analyses with respect to Ab content in them are different compared to the other basalts. For these eucrites, high-K analyses are distributed throughout the Ab range; for example, PCA 82501 (Fig. 4c). Many of the high-K analyses lie to the high-K side of an estimated solvus in the plagioclase-alkali feldspar system, indicating that these compositions likely result from beam overlap on small K-feldspar inclusions in the plagioclase (e.g., see McQuaig et al. 2019). The most K-rich composition measured is $An_{56.0}Ab_{12.7}Or_{31.3}$ in Stannern group eucrite PCA 91179.

Figure 4d shows the average Or versus Ab contents for eucrite-type achondrites. Two averages for Orlando are given, one computed for all analyses on the Or-Ab trend curve for this meteorite, and one for the grain described above that is K-poor compared to the trend curve. The latter is the only example of a grain with atypically low K contents found in this study.

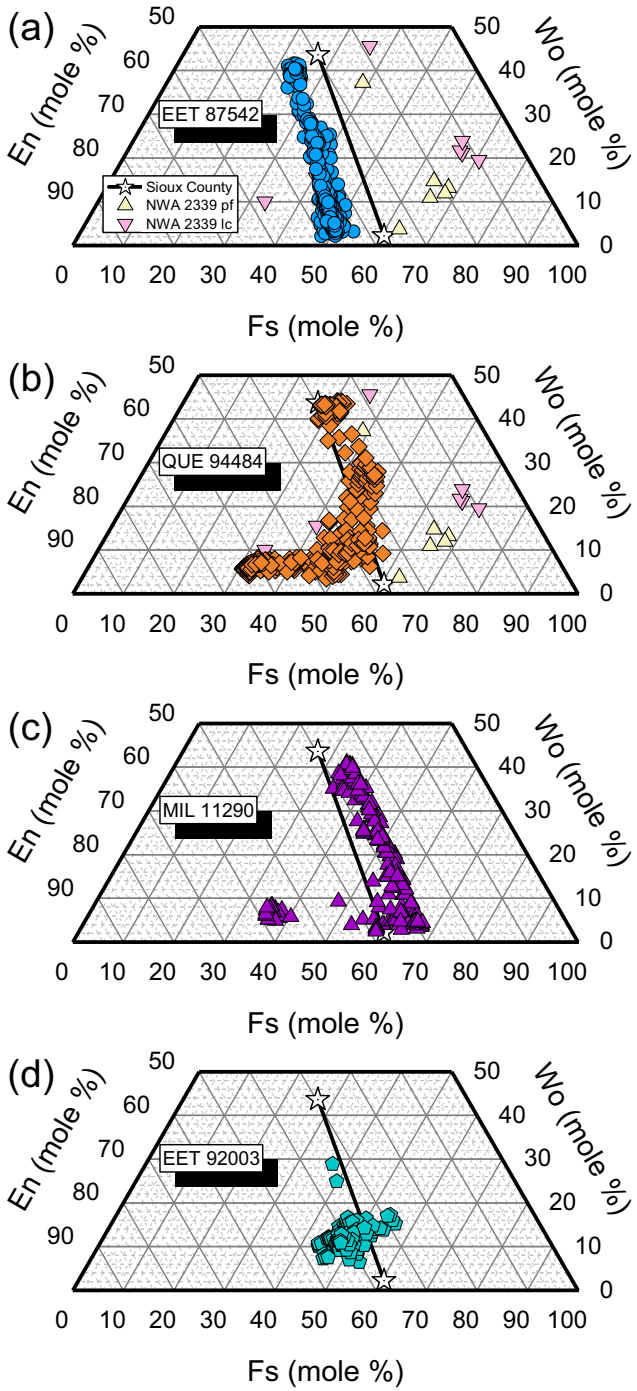

Fig. 3. Pyroxene quadrilateral diagrams for EET 87542 with reduced pyroxenes, and for three eucrite-type achondrites with unequilibrated pyroxenes. Average low-Ca and high-Ca pyroxenes from basaltic clasts from Sioux County are shown for comparison. Data for reduced pyroxenes from NWA 2339 matrix pyroxene fragments (pf) and lithic clasts (lc) from Zhang et al. (2013) shown for comparison in (a) and (b).

Anomalous cumulate Asuka (A-) 881394 and anomalous basalt Ibitira contain the most Na-poor plagioclases (Table 4; Fig. 4d) (cf. Wilkening and Anders 1975; Steele and Smith 1976; Takeda et al. 1997; Mittlefehldt 2005). Other anomalous eucrite-type achondrites have plagioclase compositions within the range of isotopically normal meteorites. Stannern group basalts occupy the Na-rich end of the data array, as first noted by Delaney et al. (1981a).

The most common oxide phases in eucrite-type achondrites are Cr-rich to Ti-rich spinels and ilmenite. The spinels mostly have a restricted range in Al/Cr but a substantial range in Ti, from Ti-poor spinels in cumulate gabbro Allan Hills (ALH) 85001 that are within the field for diogenite chromites, to Ti-rich spinels in Ibitira averaging ~62 mole% ulvöspinel (Usp) component (Table 5; Fig. 5). Among cumulate gabbros, ferroan cumulate Y-791195 contains Ti-rich spinels (Fig. 5) (Mittlefehldt and Lindstrom 1993), which are slightly more Ti-rich than those in Moore County (Bunch and Keil 1971; Mayne et al. 2009). Basalts MIL 07016 and GRO 17210 stand out in containing spinels with an atypically high Al/Cr (Fig. 5). However, we located only a single spinel grain in MIL 07016, and thus, we cannot know whether this composition is representative. We analyzed two grains in GRO 17210 which have different Al/Cr, but both are higher than the basaltic eucrite median. GRO 17210 is tentatively paired with GRO 17098 and GRO 17200. If this pairing is correct, then spinel compositions in this basalt are heterogeneous. Unbrecciated metabasalt BTN 00300 contains spinels with two quite distinct compositions; three grains average 47.8 mole% Usp and a typical Al/Cr; one grain contains 6.44 mole% Usp and Al/Cr higher than the median ratio (Fig. 5). The latter is close in composition to the more Al-poor chromites in some diogenites, while the other three are among the more Ti-rich eucrite-type achondrite spinels. The average spinels in most eucrite-type achondrites have ulvöspinel contents between ~8 and ~40 mole% (Table 5; Fig. 5). Some meteorites contain spinels with a large range in composition, for example, Orlando (Fig. 6a), while others exhibit a much narrower range, for example, the basalt clasts in Sioux County (Fig. 6b).

Besides BTN 00300, GRO 17210, and MIL 07016, two eucrite-type achondrites contain spinels with Al/Cr quite different from the median value: Dominion Range (DOM) 08001 and QUE 94484 (Figs. 6c and 6d). The low-Al grain in DOM 08001 is part of a composite ilmenite-spinel grain. It has by far the highest V_2O_3 content, 2.4 wt%, of all measured; maximum values of

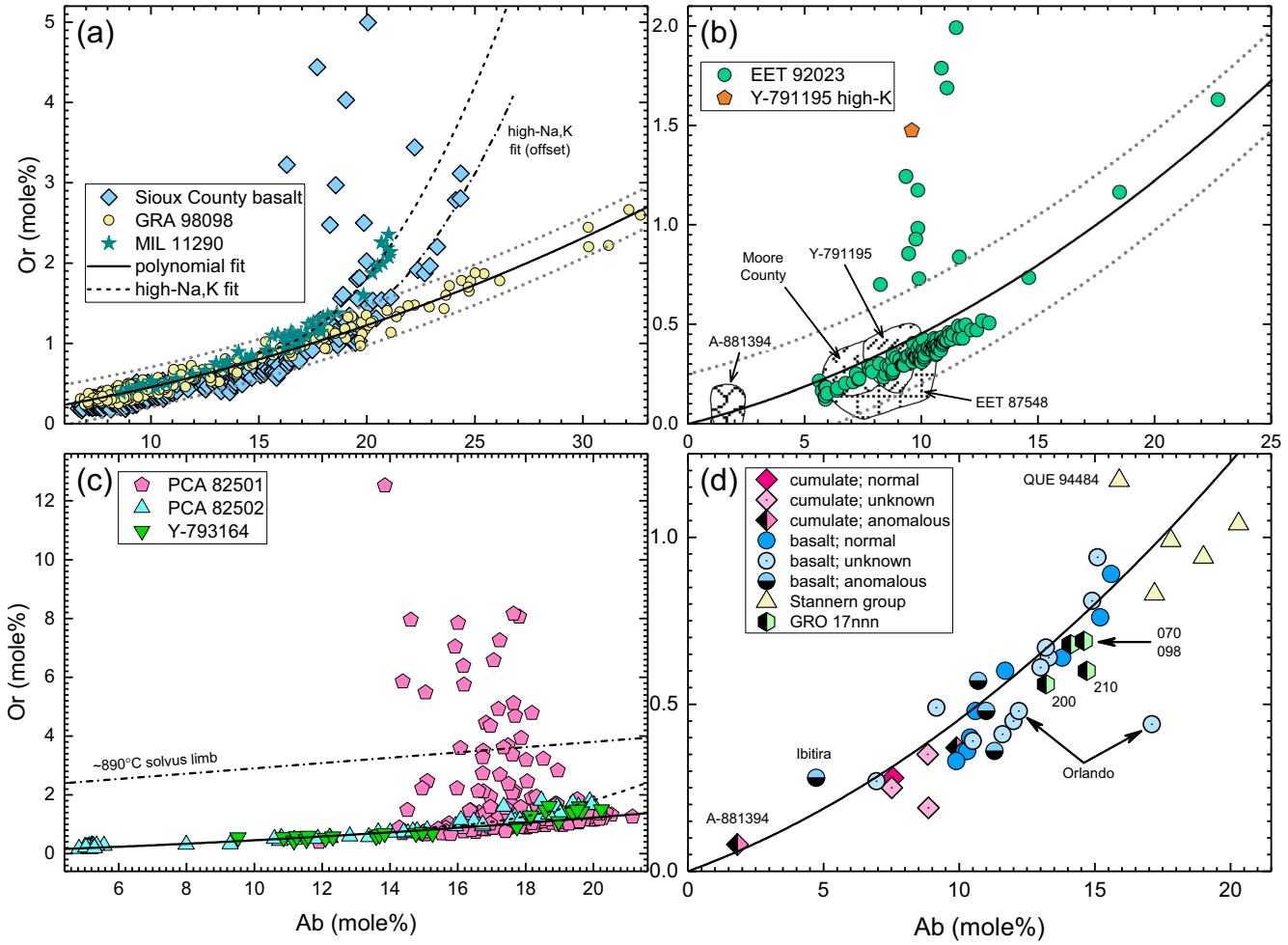

Fig. 4. Mole% Or versus Ab for eucrite-type achondrites showing: (a) contrasting distributions for GRA 98098, MIL 11290, and Sioux County basalt clasts; (b) comparison of eucrite-type cumulate gabbro EET 92023 to other cumulate gabbros; (c) comparison of plagioclase compositional distributions in PCA 82501, PCA 82502, and a metabasalt clast from Y-793164; and (d) differences in plagioclase means. Solid curve is a two-degree polynomial fit to the GRA 98098 data, and the dotted curves are ±0.25 mole% Or from that curve. Analyses lying above the upper dotted curve are defined as high-K plagioclases and are excluded from the means (see text). Dashed curve in (a) and (c) is a polynomial fit to the high Na, K analyses for MIL 11290, and the dash-dot curve in (a) is an offset to the dashed curve (see text). The ~890 °C solvus limb in (c) was estimated from Elkins and Grove (1990). Plagioclase field for cumulate gabbro ALH 85001 in (c) is completely overlapped by those for EET 87548, Moore County, and Y-791195. The GRO 17 eucrites are identified by the last three digits of their names.

≤1.1 wt% are found in all other eucrite-type achondrites. QUE 94484 includes spinel with the highest Al/Cr measured; 0.542 compared to a eucrite-type achondrite median of 0.236. One composite ilmenite–spinel grain contains heterogeneous spinel (black dots, Fig. 6d) with some compositions close to the median Al/Cr and some with >97 mole% (Fe,Mg)Cr_2O_3 component. These latter are exceptional among spinel analyses determined by us or available in the literature (cf. Mittlefehldt 2015).

Average spinel compositions span wider ranges in Fe/Mg and Fe/Mn than do those of ilmenites (Fig. 7). Oxide phases in anomalous basalt Ibitira have higher Fe/Mn than found in other eucrite-type achondrites; other anomalous eucrite-type achondrites are not atypical in this ratio. Petrologically unusual basalts EET 90020 and GRA 98098 have higher Fe/Mn in spinel and ilmenite than do most eucrite-type achondrites. BTN 00300, Caldera, EET 87520, and Y-791195 also stand out as having higher Fe/Mn in spinel than typical for eucrite-type achondrites. EET 87542, which contains pyroxenes with by far the lowest Fe/Mn (Fig. 2a), also contains spinel and ilmenite with low Fe/Mn (Fig. 7). Ilmenite in QUE 94484 also has a low Fe/Mn, as do the more ferroan pyroxenes in this meteorite (Fig. 2a).

Olivine grains are ferroan, with mg# in the range 16.9–28.4 (Table S3). The most ferroan olivine we have

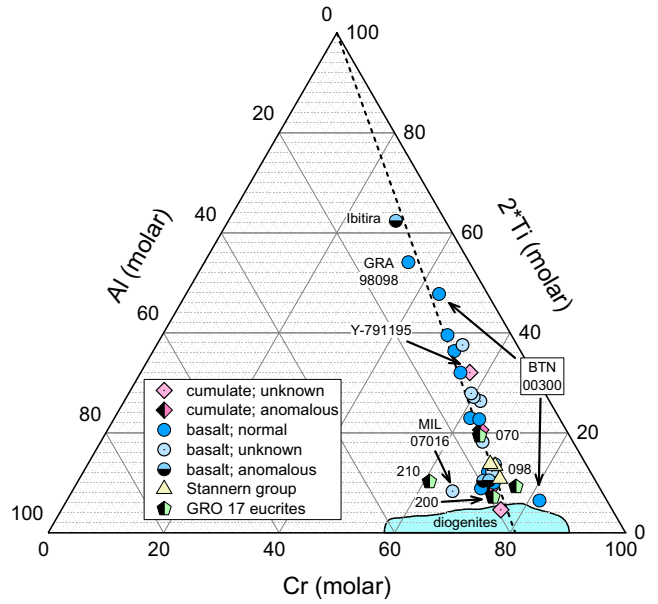

Fig. 5. Spinel ternary diagram showing variations in average spinel compositions for eucrite-type achondrites. Dashed line is the median Al/Cr ratio for all meteorites. The field for diogenites is based on data summarized in Mittlefehldt (2015). The GRO 17 eucrites are identified by the last three digits of their names.

found is from a fine-grained metabasalt clast in polymict eucrite Y-793164 (Mittlefehldt and Lindstrom 1993). Olivine grains in anomalous cumulate gabbro EET 92023 and basalt GRA 98098 occur on the rims of oxide phases, similar to the textural settings in EET 90020 and Ibitira (Steele and Smith 1976; Yamaguchi et al. 2001). Olivine grains in CMS 04049 and MIL 11290 are in mesostasis regions.

Metal and troilite are common accessory phases in basaltic and cumulate eucrites (see Mittlefehldt 2015), but they were not systematically studied as part of this investigation. Two basaltic eucrites are atypically rich in metal and/or troilite: EET 87542 and QUE 94484. Metal in EET 87542 is pure Fe, with Co and Ni below detection (Table S4). Mayne et al. (2009) noted that QUE 94484 was rich in troilite, which was associated with silica, but did not observe metal in this weathered meteorite. We found several small metal grains in QUE 94484, which are effectively pure Fe (Table S4). Small amounts of Co and Ni were above the formal limits of detection, but none of the Ni, and only a few of the Co analyses were above the limits of quantification, defined as three times the limit of detection. Troilite in QUE 94484 is pure FeS, with Cr, Co, and Ni below the detection limit. Cumulate gabbro EET 92023 contains abundant, coarse-grained Ni-rich metal (Kaneda and Warren 1998; Mayne et al. 2009; Yamaguchi et al. 2017). Our analyses show three distinct compositional ranges for Co and Ni, suggesting that kamacite, taenite, and tetrataenite are present. We have not done structural studies on the metal phases and cannot confirm that the highest Ni phase is tetrataenite. Metal of this composition is identified as being Ni-rich rims on taenite by Yamaguchi et al. (2017). Troilite in EET 92023 is pure FeS.

DISCUSSION

A major focus of this research is to determine whether there are petrologic anomalies in eucrite-type achondrites, particularly differences in pyroxene Fe/Mn, that correlate with O-isotope anomalies, and if so, their implications for the origins of the meteorites. Such associations have been documented for NWA 011 (Yamaguchi et al. 2002) and Ibitira (Mittlefehldt 2005). For NWA 011, the O-isotope anomaly is very large, with a $\Delta^{17}O$ of −1.58‰ compared to a eucrite mean from the same laboratory of −0.25‰ (cf. Yamaguchi et al. 2002; Floss et al. 2005). Low-Ca pyroxene Fe/Mn ratios for NWA 011 are ~65–67 (Yamaguchi et al. 2002; Floss et al. 2005), very distinct from the value typical of basaltic eucrites, ~30–32 (Fig. 2a). Furthermore, NWA 011 plots within the carbonaceous ^{50}Ti-^{54}Cr-isotope cluster while HED meteorites plot in the noncarbonaceous cluster (Warren 2011). The formation of NWA 011 and pairs on a parent asteroid distinct from that of HEDs is very strongly supported (Yamaguchi et al. 2002; Floss et al. 2005). Differences in O-isotope composition and pyroxene Fe/Mn for Ibitira compared to typical basaltic eucrites are less pronounced (Wiechert et al. 2004; Mittlefehldt 2005; Scott et al. 2009). Ibitira also has textural and compositional distinctions from typical basaltic eucrites that, taken together, favor formation on a distinct asteroid (Mittlefehldt 2005).

In contrast, some eucrite-type achondrites have clearly resolved O-isotope anomalies yet show no resolvable distinctions in pyroxene Fe/Mn. Emmaville has a $\Delta^{17}O$ that is +12.6 MAD units from the HED igneous median (Table 2) but contains pyroxenes with Fe/Mn within the range of basaltic eucrites (Barrett et al. 2017). Bunburra Rockhole has an O-isotope composition (Bland et al. 2009; Benedix et al. 2017) with $\Delta^{17}O$ +15.3 MAD units different from the HED igneous median (Table 2). However, its pyroxene Fe/Mn is within the range of normal basaltic eucrites (Bland et al. 2009). Thus, although in some instances, eucrite-type achondrites have anomalous O-isotope compositions and petrologic characteristics, such correlations are not assured.

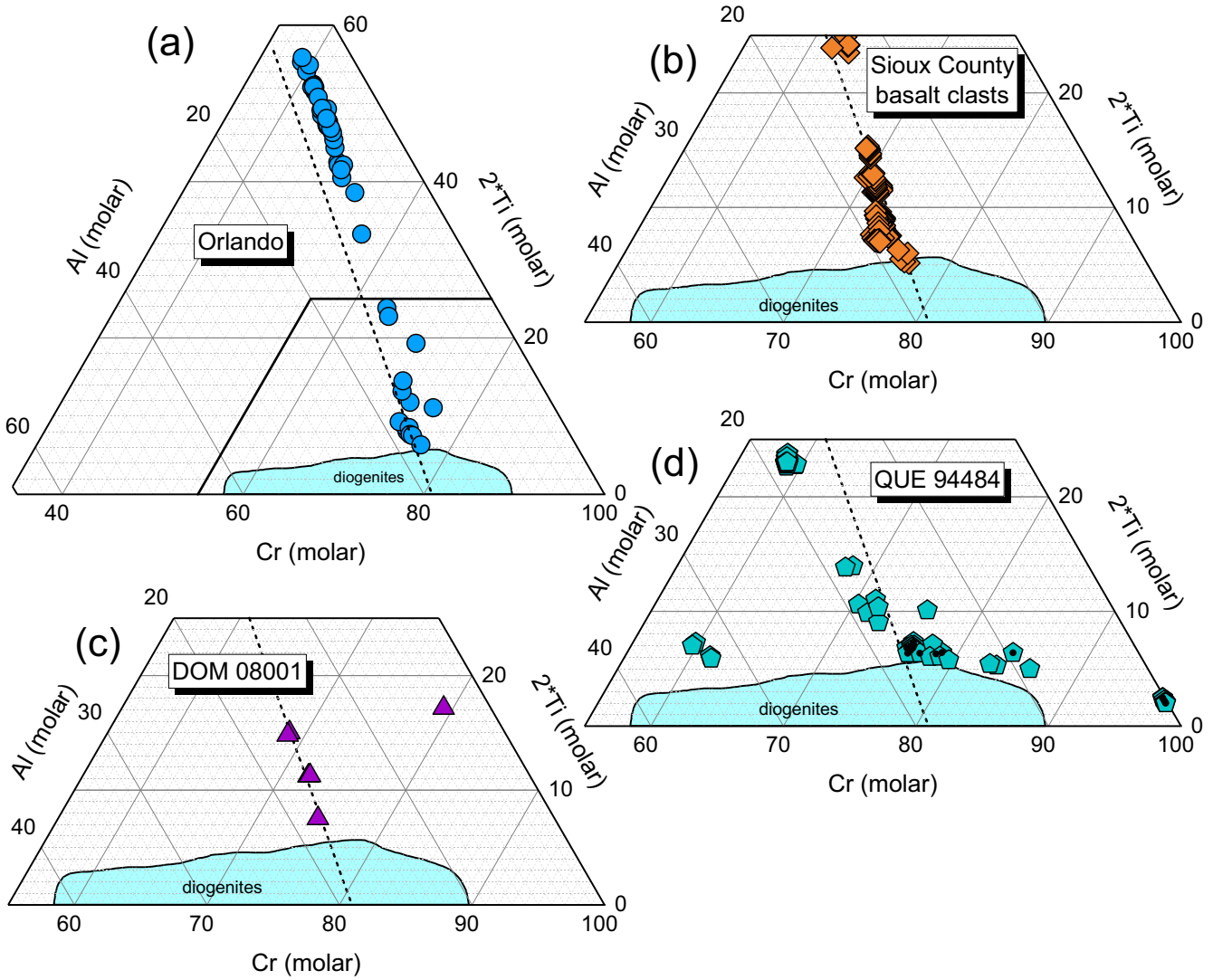

Fig. 6. Spinel ternary diagrams illustrating differences in degree of compositional variation of Orlando (a) and Sioux County basalt clasts (b), and two meteorites (c and d) containing spinels with Al/Cr very different from the eucrite-type achondrite median (dashed lines). Solid line in (a) shows scale area used in (b) through (d). Black dots (d) are analyses from composite ilmenite–spinel grain that includes nearly pure Cr spinel; see text.

Here, we will examine the petrologic data on the suite of eucrite-type achondrites to establish (1) the correlations of petrologic and O-isotope anomalies, (2) whether petrologic anomalies unassociated with isotopic anomalies exist, (3) possible causes for petrologic anomalies, and (4) revisit petrologic distinctions that can serve to identify possible Stannern group eucrites in the absence of telltale bulk compositional information. The discussion will begin by evaluating our new oxygen isotope data in the wider context of eucrite-type achondrite data. We will then discuss a set of basaltic meteorites that show anomalous petrologic characteristics yet have normal O-isotope compositions, followed by a pair of basalts that are anomalous in petrology and O isotopes. We will then transition to a discussion of cumulate gabbros. We will shift the focus to a discussion of plagioclase compositions of all samples. We will conclude with a discussion of the implications of our results for models of petrogenesis on the eucrite parent asteroid.

Oxygen Isotopes

An important motivation of the present study has been to identify robust criteria for distinguishing different groups of eucrite-type achondrites. We have sought to define geochemical, mineralogical, and isotopic characteristics that can be used to separate meteorites derived from the HED parent body from those eucrite-type achondrites derived

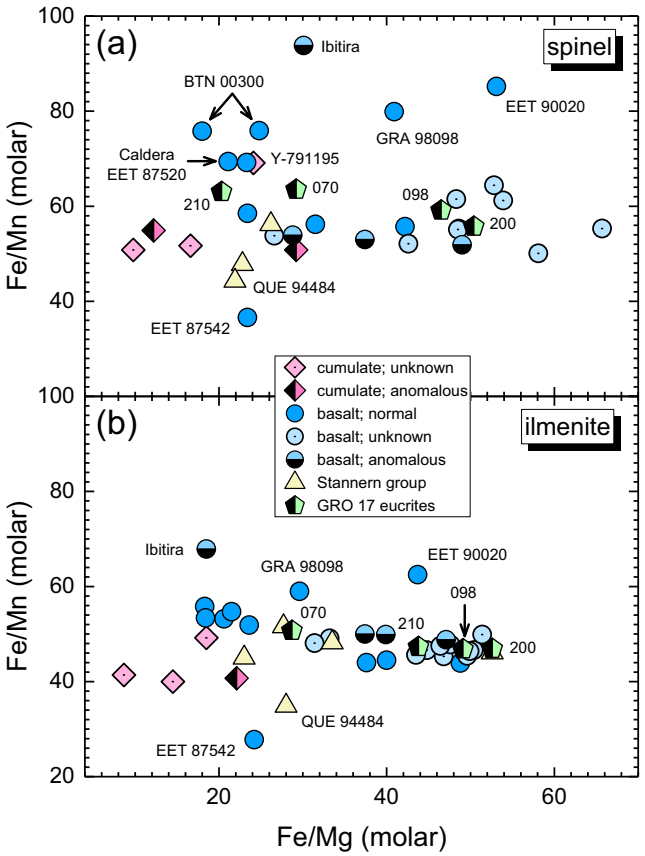

Fig. 7. Variation diagrams of Fe/Mn versus Fe/Mg for eucrite-type achondrite spinel (a) and ilmenite (b). The GRO 17 eucrites are identified by their last three digits.

from other source asteroids. As discussed earlier, using oxygen isotope ($\Delta^{17}O$) differences alone to identify which samples are from the HED parent body and which are not can involve somewhat circular reasoning. Wiechert et al. (2004) identified several samples that had $\Delta^{17}O$ compositions that diverged from the HED mean value, in particular Ibitira and to a lesser extent Pasamonte. Based on the premise that all HED-like samples were from a single parent body, Wiechert et al. (2004) used the thermal modeling of Ghosh and McSween (1998) to explain how the HED source asteroid could have mainly comprised well-mixed, and so isotopically homogenized, material within the interior of the body, but with some heterogeneity retained in its outer layers. In contrast, Greenwood et al. (2005, 2017) and Scott et al. (2009) placed greater emphasis on the fact that the vast majority of HED samples display limited $\Delta^{17}O$ variation. They suggested that this was consistent with magma ocean models for the HED parent body (e.g., Righter and Drake 1997; Ruzicka et al. 1997), with the high levels of melting and mixing involved, leading to isotopic homogenization. Based on this well-mixed HED parent body scenario, outliers such as Ibitira, A-881394, and EET 92023 (Fig. 1) were considered to represent material derived from distinct source asteroids. Scott et al. (2009) used a >3σ from the mean cutoff to define those eucrite-type achondrites as probably arising on distinct asteroids from that of eucrites sensu stricto.

Support for a single isotopically homogenized HED parent body comes from the essentially skewed distribution of $\Delta^{17}O$ values about the HED mean (Fig. 1b). A single isotopically heterogeneous parent body would be expected to show symmetrical tails about this mean value, with anomalous samples distributed evenly at higher and lower $\Delta^{17}O$ values. However, this is not the case. The majority of anomalous eucrites so far identified plot between the eucrite and angrite fractionation lines (Fig. 1), with only NWA 1240 having a more negative $\Delta^{17}O$ value than the normal HED range. This is not the sort of distribution that would be expected of an asteroid with a well-mixed interior, but with outer layers that preserve higher, but normally distributed, levels of isotopic heterogeneity. (We ignore the NWA 011 pairing group which also has a more negative $\Delta^{17}O$ value because of the Ti- and Cr-isotopic data that show it is derived from a different major reservoir in the solar system [Warren 2011].)

Another, but perhaps less clear-cut, line of evidence supporting a single homogeneous source body for isotopically normal HEDs is the fact that some of the isotopic outliers show unique characteristics, such as the exceptionally low Na and K concentrations, low Ga/Al ratio, and extremely old age of A-881394 (Nyquist et al. 2003; Scott et al. 2009). Ibitira is also alkali depleted compared to normal HEDs, highly vesiculated, and its pyroxenes have an anomalously high Fe/Mn ratio (Mittlefehldt 2005). Unfortunately, as is the case for Emmaville (Barrett et al. 2017), not all isotopically anomalous, eucrite-type achondrites show clear-cut mineralogical and geochemical differences to the isotopically normal HEDS.

A further problem with using oxygen isotopic evidence in isolation is the fact that two samples, which are likely derived from different asteroidal sources, can have almost identical $\Delta^{17}O$ compositions. Ibitira and the angrites are a case in point. These have very distinct mineralogical and geochemical compositions (Mittlefehldt 2005; Keil 2012) and were never thought to be genetically related, but as can be seen from Fig. 1, Ibitira plots on the angrite fractionation line. A subtle example is the relationship between mesosiderites and HEDs. They have indistinguishable $\Delta^{17}O$ compositions (Greenwood et al. 2006, 2017) and are broadly petrologically similar (Mittlefehldt 1979; Rubin and Mittlefehldt 1992). Nevertheless, small but important

differences in petrology, bulk composition, and chronology indicate that mesosiderites and HEDs are derived from different asteroids (Rubin and Mittlefehldt 1993). Is it possible that a similar relationship exists between QUE 94484 and normal HEDs? As discussed earlier, QUE 94484 shows anomalous characteristics, in particular zoned pyroxenes with low Fe/Mn and high Fe/Mg ratios and high troilite content (Mayne et al. 2009; this study). However, QUE 94484 has a $\Delta^{17}O$ composition close to the HED median (Fig. 1), although its $\delta^{18}O$ value is anomalously low for a basaltic eucrite. Taken at face value, these suggest that it is possible that QUE 94484, despite its HED-like $\Delta^{17}O$ composition, may not be derived from the HED parent body. But as we discuss below, its anomalous petrological character can be explained as arising on the HED asteroid.

Even if it is accepted that most eucrite-type achondrites with an anomalous $\Delta^{17}O$ composition are derived from distinct asteroidal sources, the skewed distribution seen in Fig. 1b is problematic. With the notable exception of the NWA 011 pairing group, all other eucrite-type achondrites so far identified are members of the noncarbonaceous chondrite (NC) association, as defined on plots such as $\varepsilon^{50}Ti$ versus $\varepsilon^{54}Cr$ and $\Delta^{17}O$ versus $\varepsilon^{54}Cr$ (Warren 2011). Despite the increasing number of differentiated achondrites currently being identified (Greenwood et al. 2020), the vast majority of these NC-related achondrites appear to be HED related. In addition, even with the availability of an increasing number of samples, there is no evidence that the skewed distribution seen in Fig. 1b is an artifact resulting from limited sampling of non-HED differentiated asteroids. The NC association spans a range from $\Delta^{17}O$ from almost −3½ (ureilites) to almost +3½ (R chondrites; Greenwood et al. 2017, 2020). A priori, one might expect there to be an even distribution of differentiated achondrite parent bodies throughout this range even if most samples are derived from parent bodies that have favorable delivery locations, such as seems to be the case for the normal HEDs. A skewed $\Delta^{17}O$ distribution is therefore problematic even if it is accepted that isotopically anomalous eucrites sample distinct asteroidal sources.

Several processes can be put forward to explain the $\Delta^{17}O$ distribution of eucrite-type achondrites. The first possibility is that the majority of anomalous eucrite-type achondrites are generically related to the HEDs by some form of impact processing. It could be hypothesized, based on the current terrestrial fall statistics, that the bulk of large-sized impactors striking the HED parent body would have had an ordinary chondrite-like $\Delta^{17}O$ composition, that is, one lying above the TFL. That such a process has taken place, on at least a small scale, is demonstrated by the howardite impact melt breccia Jiddat al Harasis (JaH) 556 (Janots et al. 2012). This meteorite contains both HED and H chondrite-related clasts enclosed in a siderophile-enriched, recrystallized matrix, which has an anomalous $\Delta^{17}O$ composition ranging from −0.10 to −0.14½ (Janots et al. 2012). Anomalous eucrite-type achondrite Dhofar 007 has an elevated siderophile element composition (Yamaguchi et al. 2010) and so may possibly have formed in an analogous way to JaH 556, although Yamaguchi et al. (2010) appear to favor an origin for Dhofar 007 as a mesosiderite-related clast. However, in most cases, eucrite-type achondrites with anomalous oxygen isotope compositions do not have elevated siderophile element compositions (Scott et al. 2009), indicating that ordinary chondrite-like impactors cannot be invoked as a general explanation for the skewed oxygen isotope distribution seen in Fig. 1b.

Differentiated igneous clasts are a relatively common component in some ordinary chondrite meteorites and have oxygen isotopic compositions that plot above the TFL (Ruzicka et al. 2019). Impactor material with a composition similar to such clasts, incorporated into a normal HED host, would be less easy to identify chemically as it would lack an elevated siderophile element signature. However, the igneous clasts identified by Ruzicka et al. (2019) are all rich in olivine and would change the major element composition of any impact mixture away from that of eucrites. If the outer layers of the HED parent body were preferentially enriched by impactor material that originally had a $\Delta^{17}O$ composition lying above the TFL, local to regional scale assimilation processes might in part account for the skewed distribution seen in Fig. 1b. However, the apparent paucity of isotopically anomalous Stannern group eucrites, which are thought to have been formed by an internally driven magma assimilation process (Barrat et al. 2007), would appear to suggest that assimilation of exogenous material was not a process of major importance.

Brecciated Basalt EET 87542

EET 87542 is a fine-grained, clast-poor fragmental breccia containing lithic clasts of fine-grained basalt. The matrix is relatively fine-grained and homogeneous, with most mineral fragments being ~300 μm or less in diameter. Matrix grain fragments generally have rounded corners suggesting metamorphic recrystallization. Lithic clasts are fine-grained ophitic/subophitic basalts, but grain size in some approach the medium grain size limit of 1 mm. The largest lithic clast in the two sections

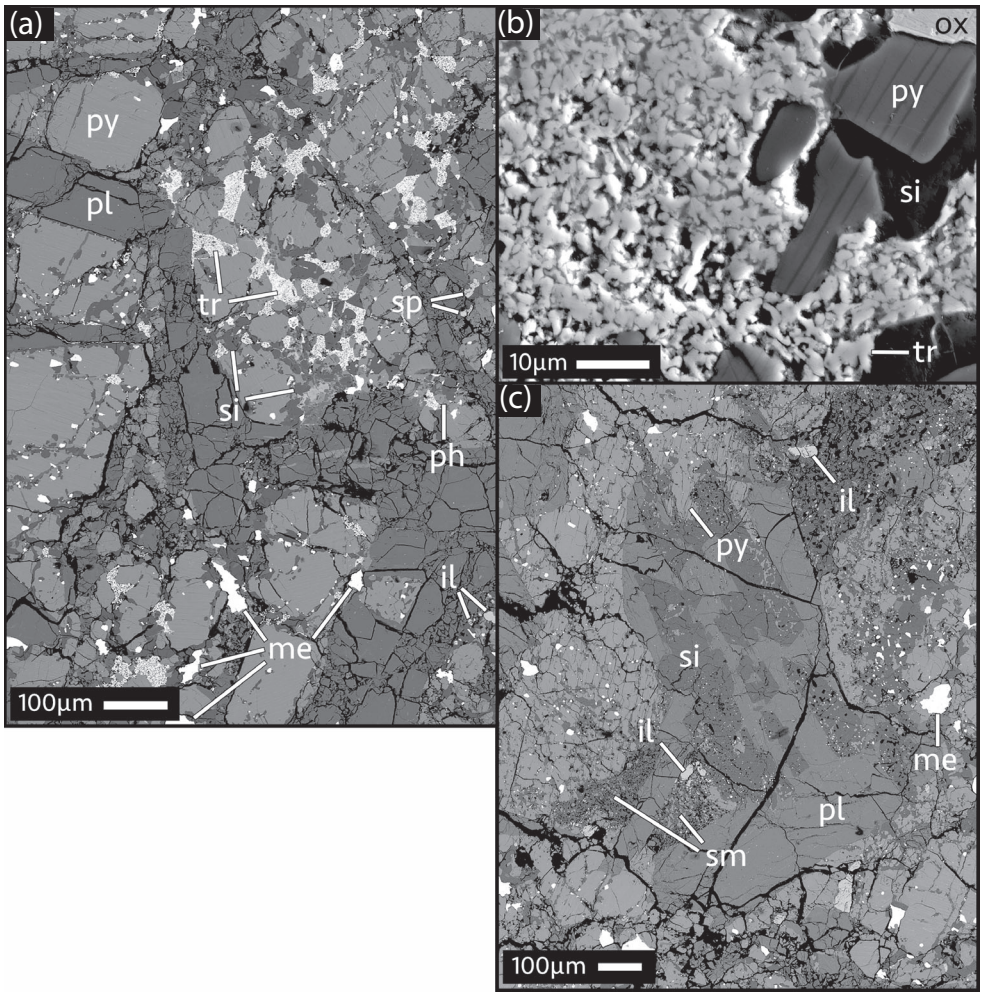

Fig. 8. Backscattered electron (a and c) and secondary electron (b) images from EET 87542,19 illustrating textural details: (a) abundant silica and troilite inclusions in pyroxene in fine- to medium-grained basalt clast; (b) detail view of mottled troilite; (c) coarse euhedral/subhedral silica poikilitically enclosed in plagioclase in medium-grained, subophitic basalt clast. il = ilmenite; me = metal; ph = Ca-phosphate; pl = plagioclase; py = pyroxene; si = silica; sm = silica-rich mesostasis; sp = spinel; tr = troilite.

investigated is >7 mm in longest dimension but is on the edge of the section and thus possibly incomplete.

Very fine grains of nearly pure Fe metal are abundant and are enclosed in pyroxene grains in the matrix and in lithic clasts. The metal is associated with very fine-grained silica in curvilinear vein-like structures in low-Ca pyroxenes (Fig. 8a). Metal is often associated with mottled troilite that is composed of numerous, anhedral to euhedral, micron-sized grains with intergranular pore spaces (Fig. 8b). Fine-grained metal and troilite in vein-like textural settings are found in other basaltic eucrites. Essentially pure Fe metal occurs in curvilinear veins in pyroxene in NWA 5738, but the texture is different from that of EET 87542 and the metal is not associated with silica (Warren et al. 2014). Fine-grained silica is associated with troilite as inclusions in a few pyroxene fragments in the breccia and in one lithic clast in basaltic eucrite NWA 2339 (Zhang et al. 2013). The pyroxene–silica–troilite textures in NWA 2339 show some resemblance to those displayed by EET 87542, suggesting a similar process could be responsible. Zhang et al. (2013) argue that the pyroxene–silica–troilite texture resulted from sulfurization by dry S-rich vapors engendered by impact heating on the surface of the parent asteroid, which they equate with 4 Vesta. Note that one difference between NWA 2339 and EET 87542 is that the silica inclusion textures are uncommon in the former; they are pervasive in the latter.

EET 87542 is noteworthy for having the lowest mean pyroxene Fe/Mn of any eucrite-type achondrite (Table 3), and lower than those of basaltic and gabbroic

clasts from mesosiderites (Fig. 2a). Pyroxenes in EET 87542 are also more magnesian than typical of basaltic eucrites such as Sioux County (Fig. 3a). Most basalt and gabbro clasts in mesosiderites are secondary magmatic rocks formed by remelting of materials of the primary mesosiderite parent asteroid crust after metal–silicate mixing; the low Fe/Mn ratios are engendered by reduction of FeO from the silicate magma by reducing agents derived from the metallic phase (Mittlefehldt 1979, 1990; Rubin and Mittlefehldt 1992). Reduction of FeO also occurred in the solid state in mesosiderite breccias during metamorphism (e.g., Mittlefehldt et al. 1979; Delaney et al. 1981b; Harlow et al. 1982). In this case, metal grains are enclosed in pyroxene and associated with inclusions of silica and troilite (e.g., fig. 3 of Mittlefehldt et al. 1979), as observed in EET 87542.

Pyroxene compositions in NWA 2339 (Zhang et al. 2013) show some compositional similarities to those of EET 87542. Low-Ca pyroxenes in the sulfurized pyroxene fragments in NWA 2339 have Fe/Mn-like low-Ca pyroxenes in EET 87542 but are much more ferroan; Fe/Mg ~3.1 versus 1.06 for EET 87542 (Table 3; Fig. 3a). However, high-Ca pyroxenes in the sulfurized pyroxene fragments have Fe/Mn typical of basaltic eucrites, unlike the case for EET 87542 (Table 3). Low- and high-Ca pyroxenes from the single sulfurized lithic clast in NWA 2339 have Fe/Mn like those of typical basaltic eucrites and are unlike pyroxenes in EET 87542. Thus, although there is some similarity in having an unusually low Fe/Mn in some low-Ca pyroxenes, more generally the pyroxenes in sulfurized materials in NWA 2339 are compositionally quite different from those in EET 87542.

The textural characteristics and compositions of pyroxenes in EET 87542 support a solid-state reduction process as causing the coupled low Fe/Mn and Fe/Mg. A simple mass balance calculation of adding $FeSiO_3$ to the average low-Ca pyroxene composition (Table 3) until the molar Fe/Mn reaches 31 results in a pyroxene with Fe/Mg within the field of basaltic eucrites (Fig. 2a). Thus, a reducing agent acting on typical basaltic eucrite pyroxenes could have modified original pyroxene compositions and resulted in inclusions of silica, metal, and troilite. The compositions of oxide phases were also affected by this process as indicated by the low Fe/Mn of spinel and ilmenite (Fig. 7).

Sulfur vapor is a plausible reducing agent. Kullerud and Yoder (1963) did subsolidus reaction experiments between fayalite and S at a $T = 800$ °C, and P of 200 MPa. At high X_S, the reaction is:

$$Fe_2SiO_4 + 3S \rightarrow 2FeS + SiO_2 + SO_2(g). \quad (1)$$

This basic type of reaction was called upon by Zhang et al. (2013) to explain inclusions of troilite and silica in pyroxenes, where the reactants were S vapor and eucritic pyroxene in lieu of fayalite. In EET 87542, $Fe+SiO_2$ is a common inclusion suite in pyroxene. The above reaction is for equilibrium under a confining pressure. An open system would allow SO_2 gas to escape, driving the reaction to a more reduced assemblage. Furthermore, Kullerud and Yoder (1963) note that one of the univariant assemblages in the Fe-S-O-SiO_2 system is Fe-Fe_2SiO_4-FeS-SiO_2. The texture of troilite—aggregates of anhedral to euhedral, micron-sized grains with intergranular pores—is unlike that typical of basaltic eucrites in which troilite occurs as single, solid grains. The texture is consistent with formation from a vapor phase reaction. We contend that fluxing by hot S vapor in solid eucritic basalt is a plausible mechanism driving the redox process in EET 87542.

Textural and mineral compositional evidence shows that the redox process occurred prior to brecciation. Four observations support this interpretation. (1) The metal+silica±troilite inclusion assemblages occur within pyroxenes in the interiors of basaltic lithic clasts (Figs. 8a and 8b); (2) the inclusion assemblage occurs in many, but not all, pyroxene fragments in the matrix (Fig. 8a); (3) all pyroxene analyses show reduced compositions, including all matrix grains irrespective of whether they contain the inclusion assemblage (Table 3; Fig. 3a); and (4) where inclusion assemblages occur in matrix grains, they are as likely to be in the grain interiors as on the surfaces. In particular, the absence of metal+silica±troilite inclusion assemblages in matrix pyroxenes that nevertheless carry the compositional signature of the redox process, and the lack of preference for inclusion assemblages on the surface of matrix grains are compelling pieces of evidence that this process affected the protolith prior to fragmentation and assembly of the breccia. A hot S vapor fluxing through a porous breccia would more effectively attack the surfaces of small (<100 μm) matrix grains than the interiors of >300 μm grains in intact lithic clasts. Thus, we posit that the EET 87542 protolith was subjected to a flux of hot, S-rich vapor that caused extensive subsolidus reduction of FeO out of pyroxenes and was subsequently impacted to produce a clast-poor monomict breccia.

In the next section, we will argue that QUE 94484 underwent reduction in the magmatic stage, and we have evaluated whether this process is also plausible for EET 87542. Reduction during magmatic crystallization could result in early crystallization of silica as the melt becomes depleted in FeO by reduction. There is some textural evidence indicating that a silica phase might

have begun crystallizing unusually early in EET 87452 basalts, but it is not compelling. Some plagioclase grains in the largest lithic clast poikilitically enclose inclusion-rich silica in skeletal intergrowths, with sharp silica crystal faces against plagioclase (Fig. 8c). However, this texture is the exception, not the rule, and this suggests that it is plausibly an example of skeletal intergrowths of plagioclase and silica along the margin of a mesostasis region. Experimental work has shown that silica is the last silicate phase to crystallize and appears ~100 °C below the liquidus when ~30–20% melt remains (Stolper 1975, 1977). Indeed, one portion of the skeletal silica grain merges with silica-rich mesostasis region in the EET 87542 clast (Fig. 8c). Thus, there is no compelling textural evidence consistent with reduction during magmatic crystallization for EET 87542.

Unbrecciated Stannern Group Basalt QUE 94484

QUE 94484 is an unusual unbrecciated basalt that contains a high abundance of mesostasis regions rich in troilite and silica, and zoned pyroxenes with low Fe/Mn at high Fe/Mg (Mayne et al. 2009). It is a fine-grained subophitic to variolitic basalt with the largest grains verging on the size limit definition for medium-grained basalt (1 mm). Mesostasis regions are rich in silica, augite, troilite, and ilmenite, and lesser amounts of Ca-phosphate, spinel, and Fe metal (Fig. 9). A silica phase occurs as massive, anhedral grains in mesostasis regions, and as very fine-grained intergrowths in augite rims on ferroan pigeonite; the augite abuts mesostasis regions (Fig. 9b). The abundant troilite in these regions is closely associated with silica. Based on preliminary whole-rock compositional data, QUE 94484 is a Stannern group eucrite (Mittlefehldt et al. 2016).

Pyroxenes in QUE 94484 show extensive compositional zoning in Mg-Ca-Mn-Fe but with unusual behavior in Fe/Mn, as first documented by Mayne et al. (2009). Core pyroxene is Mg-rich low-Ca pyroxene that evolves to ferroan pigeonite, and finally to ferroan augite (Fig. 3b). This is like the type 2 eucrite pyroxene pattern of Takeda and Graham (1991). Mayne et al. (2009) showed that the core Mg-rich pyroxenes are compositionally like cumulate eucrite pyroxenes in Mg-Mn-Fe, which we confirm (Fig. 2). Thus, the initial pyroxenes were crystallized from a melt that was indistinguishable from the parents of some cumulate eucrites in major element composition.

Partitioning of Fe/Mn between melt and pyroxene leads to slight increase in melt Fe/Mn as crystallization proceeds (Stolper 1977), and this is seen in the most magnesian QUE 94484 pyroxenes. These pyroxenes show increasing Fe/Mn as Fe/Mg rises from ~0.5 to ~0.6 (Fig. 10a). However, with increasing Fe/Mg beyond this, Fe/Mn in low-Ca pyroxenes decreases dramatically from ~31 to ~22–24 (arrow, Fig. 10a). This general trend is seen in individual pyroxene grains from Mg-pyroxene cores to Fe-augite rims against mesostasis (Fig. 11a). This pattern is not expected for magmas crystallizing low-Ca pyroxene as the major ferromagnesian silicate based on partitioning behavior of Mg, Mn, and Fe (Stolper 1977). QUE 94484 pyroxenes with $Wo_{<40}$ show increasing Mn/Mg with Fe/Mg (Fig. 10a), which is generally consistent with expectations for igneous fractionation. However, the evidence for decreasing Fe/Mn with increasing Fe/Mg and Wo content indicates that the slope of the Mn/Mg versus Fe/Mg trend is steeper than it ought to be for pure igneous fractionation.

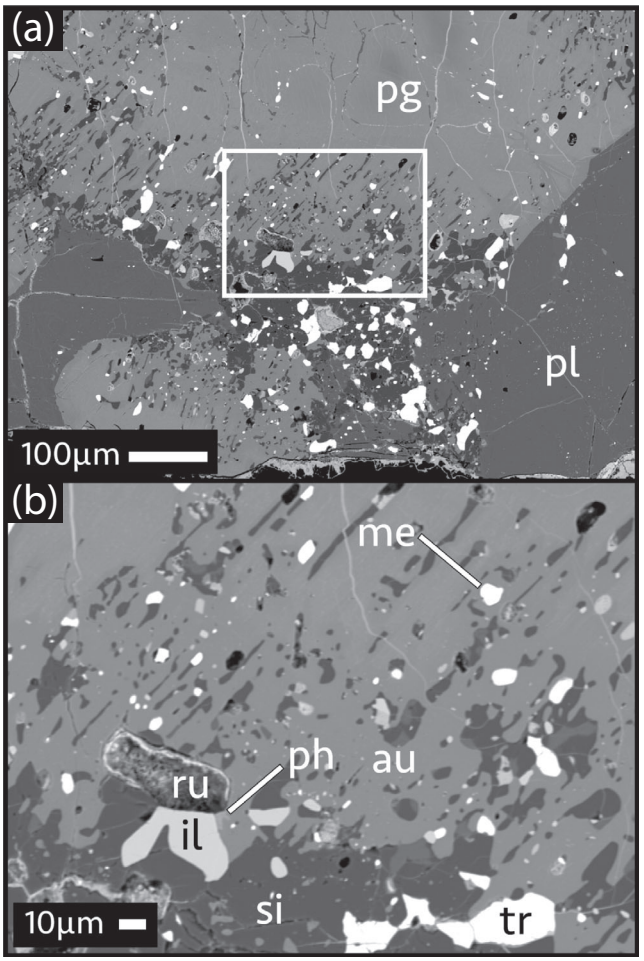

Fig. 9. Backscattered electron image of a mesostasis region in unbrecciated basalt QUE 94484; (b) is a close-up of the region in the box in (a). au = augite; il = ilmenite; me = metal; pg = pigeonite; ph = Ca-phosphate; pl = plagioclase; ru = rust (terrestrial oxidation); si = silica; tr = troilite.

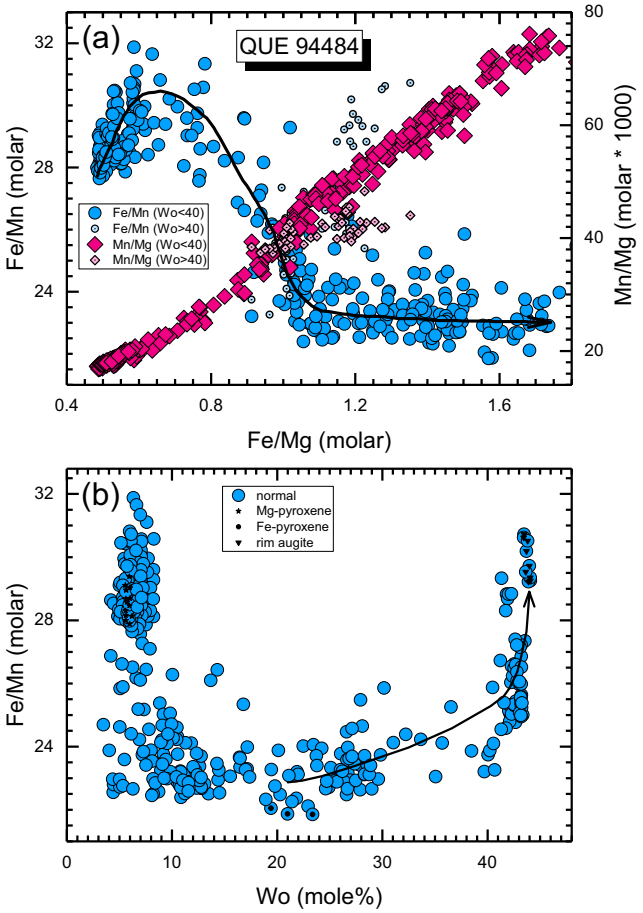

Fig. 10. Pyroxene compositional trends for QUE 94484. Curved arrow in (a) shows an approximate zoning trend for pyroxenes with $Wo_{<25}$. Augites with $Wo_{>40}$ show distinct trends relative to pyroxenes with $Wo_{<40}$. Analyses averaged for magnesian and ferroan low-Ca pyroxene, and rim augite compositions are indicated in (b).

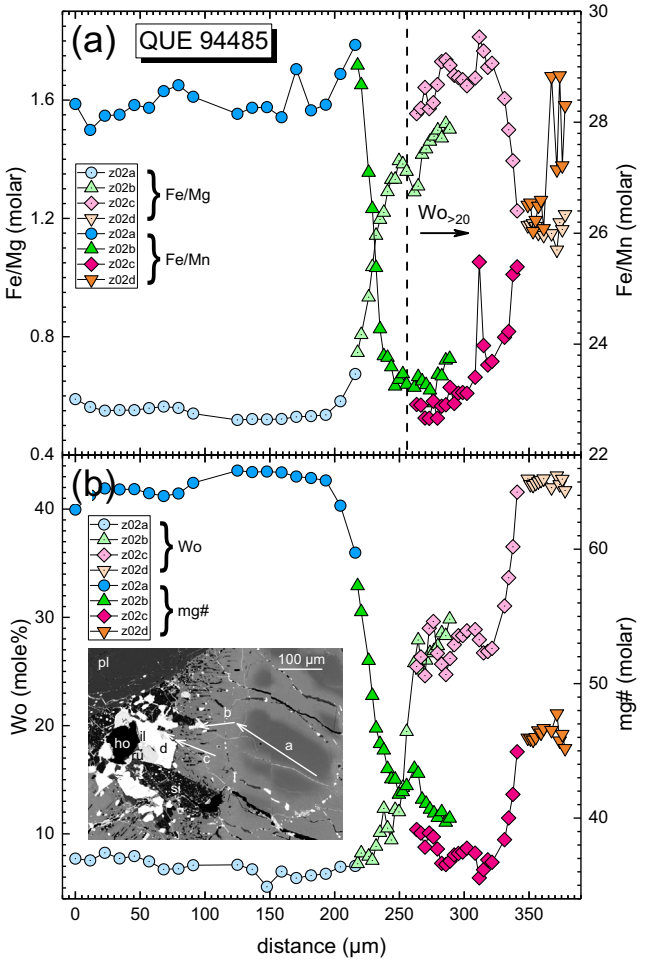

Fig. 11. Pyroxene compositional variations from Mg-rich, low-Ca pyroxene cores to ferroan augite abutting mesostasis. Dashed line in (a) separates augite ($Wo_{>20}$) from low-Ca pyroxene. Inset in (b) shows locations of the four traverses. ho = hole; il = ilmenite; pl = plagioclase; ru = rust (terrestrial oxidation); si = silica.

The substantial decrease in low-Ca pyroxene Fe/Mn with crystallization indicates the removal of FeO from the melt by some mechanism that is not typical of eucritic magmas, and we posit that S is the culprit. Troilite and silica are major components of the abundant mesostasis (Fig. 9) (Mayne et al. 2009; this study), indicating that the S content of the QUE 94484 magma was higher than typical for basaltic eucrites. The sulfur content at sulfide saturation (SCSS) of a basaltic magma is controlled by T, P, fO_2, fS_2, and melt composition, and the S content of a basalt directly impacts the magma FeO content (Haughton et al. 1974; Ding et al. 2018). We hypothesize that an atypically high S content of the QUE 94484 magma triggered loss of Fe from the silicate system to immiscible sulfide melts, resulting in decreasing Fe/Mn in low-Ca pyroxene during crystallization.

At the low fO_2 of eucrite petrogenesis (Stolper 1977), S is dissolved in magma as S^{2-} (Jugo et al. 2010). At some point during crystallization, a basaltic eucrite will become saturated in an immiscible sulfide melt. Sulfide in eucrites is pure FeS (Mayne et al. 2009; this study), and in this case, the SCSS does not depend on fO_2 or fS_2 (O'Neill and Mavrogenes 2002). Indeed, equations to model SCSS in silicate melts based on thermodynamic treatments of experimental work do not include terms for fO_2 or fS_2 (e.g., O'Neill and Mavrogenes 2002; Righter et al. 2009; Ding et al. 2018; Steenstra et al. 2020). Once sulfide saturation is reached, an immiscible sulfide melt forms via the reaction (cf. O'Neill and Mavrogenes 2002):

$$\underset{\text{silicate melt}}{FeO + S} = \underset{\text{sulfide melt}}{FeS} + \tfrac{1}{2}O_2. \quad (2)$$

Note that this is for a closed system, with O dissolved in the sulfide melt. The effect of sulfide saturation is then to reduce FeO contents of the silicate melt, lowering the Fe/Mn of ferromagnesian silicate and oxide phases crystallizing from it.

The strongest compositional control on SCSS is the FeO content of a silicate melt, with SCSS increasing from a minimum value as FeO increases from ~5 to 7 wt % (see fig. 21 of O'Neill and Mavrogenes 2002). The least evolved basaltic eucrites have FeO contents of ~18–19 wt%, while evolved, Nuevo-Laredo group eucrites contain ~20–22 wt% FeO (database of Mittlefehldt 2015). However, the FeO effect is counteracted by temperature; the SCSS of basaltic melts decreases with temperature (e.g., see fig. 7a of Righter et al. 2009). The net effect is that there is only a small variation in expected S content at sulfide saturation for basaltic eucrites, as illustrated in Fig. 12. In this figure, "model glasses" are the experimental glasses from Stolper (1977), with SCSS calculated according to the formalism of Ding et al. (2018). Figure 12a shows eucrite-type basalt data (taken from the database of Mittlefehldt 2015) for falls for comparison; standard deviations are shown for those for which ≥4 analyses were averaged. Figure 12a also shows the SCSS calculated for eucrite-type basalts (falls and finds) for which bulk major element compositions are available. The experimental glasses of Stolper (1977) have a good relationship between temperature and MgO content, and this empirical relationship was used to calculate T for the eucrite-type basalts shown in Fig. 12b. The fall data are again plotted using measured S, whereas the SCSS is plotted for model glasses and model eucrites.

Eucrite-type basalts contain S contents that straddle the zone where sulfide saturation would be expected (shaded bands in Fig. 12). However, note that most of the fall data either do not have standard deviations calculated, meaning there are few analyses available, or have large standard deviations, indicating that S is heterogeneously distributed in these rocks relative to the typical sample size. The very large standard deviation on the Stannern mean (Fig. 12a), for example, results from analyses spanning the range 0.017–1.09 wt% S (e.g., Gibson et al. 1985), a consequence of S being entirely contained in a heterogeneously distributed minor phase; S contents of eucrite-type basalts are poorly known. Two basalts have small standard deviations on their S averages and have S contents well below the SCSS value—Haraiya and Pasamonte. This suggests that some eucrite-type basalts are substantially undersaturated with respect to sulfide, while others might be closer to saturation. During crystallization, the Fe/Mn evolution of pyroxenes for these two cases would be different.

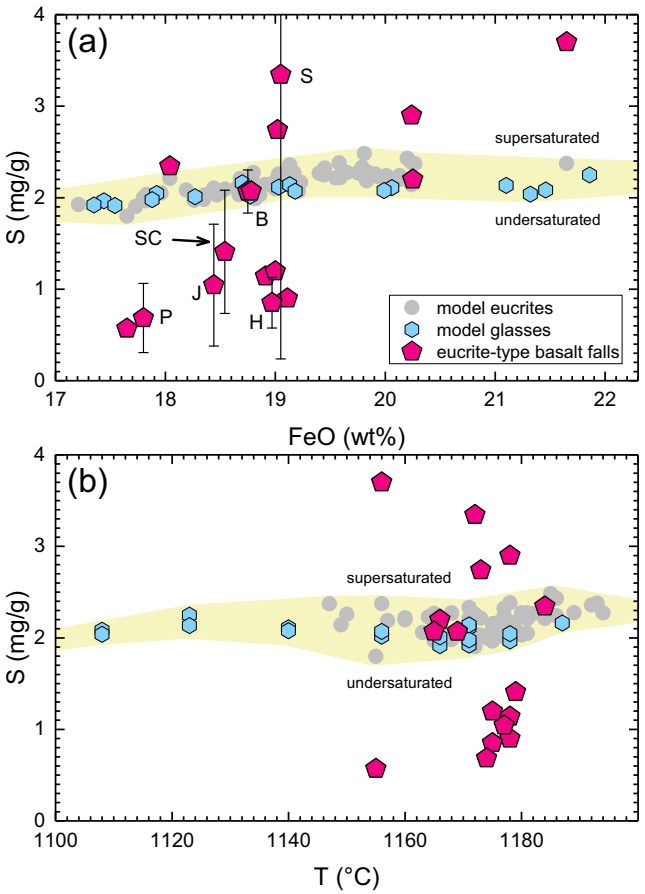

Fig. 12. The S contents of eucrite-type achondrite falls and S contents at sulfide saturation (SCSS) modeled for eucrite-type achondrite compositions and experimental glasses versus (a) FeO content and (b) temperature. Error bars in (a) are standard deviations of the averages; see text. Labeled meteorites are: B = Béréba; H = Haraiya; J = Juvinas; P = Pasamonte; S = Stannern; SC = Sioux County. In (b), temperatures for falls and model eucrites are calculated from their MgO content; see text. Experimental glasses are from Stolper (1977); SCSS is modeled following Ding et al. (2018).

We illustrate this using phase equilibria in a schematic slice of log fS_2-log fO_2-S space at constant log fS_2 for basaltic magma at 1200 °C (Fig. 13) (after fig. 4 of Haughton et al. 1974). This diagram can only be used to illustrate general principles because eucrites were formed under more reducing conditions than shown in Fig. 13—at log fO_2 ~ −13.5 (atm), which decreased during crystallization (Stolper 1977). The fS_2 for eucrite formation is not known, and the S contents of basaltic eucrites are poorly constrained as described above. Furthermore, the basalt composition used in the experiments (Haughton et al. 1974) is substantially different from basaltic eucrites, and as discussed above, melt composition has a strong influence on sulfide

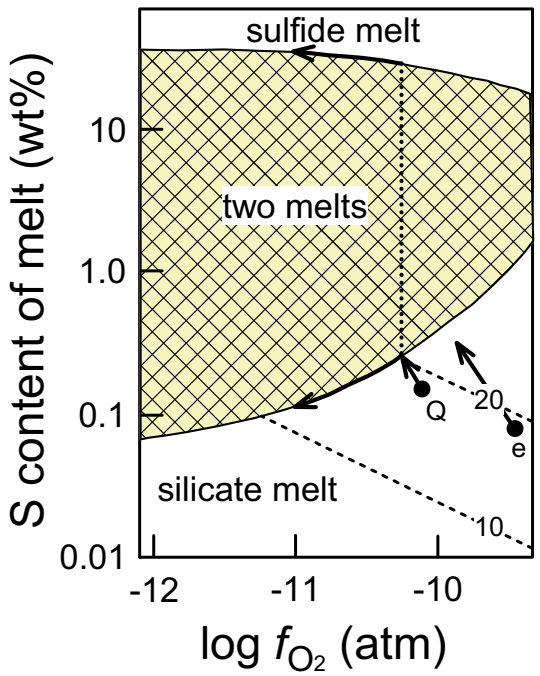

Fig. 13. Schematic phase diagram illustrating the effects of fO_2 on S contents of basaltic melts at 1200 °C and log $fS_2 = -2.10$, after Haughton et al. (1974). Dashed lines are calculated silicate melt FeO contents in wt%. Arrows illustrate proposed S redox mechanism for QUE 94484 (Q) compared to lack of redox for typical basaltic eucrites (e); see text.

saturation. Because of these many differences, Fig. 13 can only be used in a qualitative sense to suggest a mechanism for removal of FeO from the silicate melt system.

With these caveats in mind, we posit that the higher S content of QUE 94484 melt (Q in Fig. 13) resulted in it reaching the two-melt phase field earlier in the crystallization sequence than for typical basaltic eucrites (e in Fig. 13). When the Q melt reached the two-melt phase field, an immiscible FeS melt separated via reaction (2), above, and the FeO content of the silicate system decreased as the silicate magma followed the boundary of the two-melt phase field (arrow). In contrast, the lower S content of typical eucrites (e) allowed for more extensive crystallization to occur before the silicate magma reached the two-melt phase field and an immiscible sulfide melt formed. If our hypothesis is correct, then even the more typical eucrites could have suffered FeO reduction late in their crystallization sequences. Duke (1963) documented petrographic evidence for late-magmatic stage reaction of pyroxene to form troilite and silica in Juvinas, Nuevo Laredo, Sioux County, and Stannern, but he ascribed this to late-stage S vapor. He also showed that while pyroxene cores in Pasamonte are relatively free of inclusions, late-stage ferroan pigeonite and augite are clouded with troilite inclusions. Duke (1963) found no evidence for reaction of pyroxene with S vapor to form troilite in this case indicating co-crystallization from magma of these two phases for this meteorite is plausible. Compositional evidence for this process might be found in pyroxenes from mesostasis regions of type 1 unequilibrated eucrites. Any such evidence would likely have been destroyed during the metamorphism that commonly affected basaltic eucrites (e.g., Yamaguchi et al. 1996).

One issue for which we do not have a ready explanation is the rise in Fe/Mn with Wo in augite (pyroxenes with Wo_{20-45}; arrow; Figs. 10b and 11). Our analyses of pyroxenes in unequilibrated basaltic clasts and matrix grains in polymict eucrite-type achondrite Pasamonte (Mittlefehldt et al. 2017) indicate that a rise in molar Fe/Mn of ~3–4 over the range Wo_{20-45} is expected for igneous fractionation in eucrite-type basalts. In QUE 94484, this rise is ~5–8, which seems at odds with our hypothesis of FeO reduction by S within the magma. The positions of the phase boundaries shown in Fig. 13 change with changing silicate melt composition (Haughton et al. 1974; O'Neill and Mavrogenes 2002), and it is possible that evolution of the final melt to residual compositions allows back-reaction between the sulfide and silicate melts via reaction (2) above. At equilibrium, the sulfide melt would contain dissolved oxygen because the activity of FeO in the silicate melt must equal that in the sulfide melt; a few wt% O is measured in sulfides formed in saturated experimental charges (see discussion in Ding et al. 2018). The lowest T, highest FeO experimental glasses shown in Fig. 12 still contain 35–40 wt% melt (Stolper 1977). Whether the SCSS of residual eucritic melts rises with further crystallization and causes a back reaction of (2) is unknown, but we posit that this might be the explanation for rising Fe/Mn in augites abutting and within the mesostasis regions.

A plausible hypothesis for the generation of Stannern group eucrites is an assimilation–fractional crystallization (AFC) model proposed by Barrat et al. (2007). In this model, main group eucrite melts are contaminated by partial melts of crustal basalts, which result in enhanced incompatible trace element contents with little change in magma mg#. An alternative explanation for the large decrease in pyroxene Fe/Mn for Fe/Mg >0.6 (Fig. 10a) is that assimilation of substantial S occurred at about this point in the AFC process. Troilite is concentrated in the mesostasis of many basaltic eucrites, the low T melting fraction of the rocks. Contamination of main group eucrite magmas by melts of more S-rich crust potentially could result in a magma-like QUE 94484 that exhibits evidence for

sulfide saturation earlier in the crystallization process than is typical. Whole rock data demonstrate that the S contents of main group eucrites are poorly constrained, but variations of a factor of 2–3 seem possible (Fig. 12). This hypothesis predicts that reduction of silicate magma Fe/Mn by sulfide saturation would be more common in Stannern group eucrites, which could be tested through petrological studies of unequilibrated Stannern group and main group eucrites.

Basaltic Eucrites with Distinct Fe/Mn Pyroxene Populations

Basaltic eucrites CMS 04049, GRO 06059, GRO 17070, and Orlando contain pyroxenes having Fe/Mn in two well-resolved populations (Table 3; Fig. 2d). The majority population is referred to as type a, the minority as type b. Most low-Ca pyroxenes in each are within the Fe/Mn range typical of basaltic eucrites, ~31 ± 1. Minor proportions of low-Ca pyroxene grains in unbrecciated medium-grained basalts CMS 04049 (~12%) and GRO 17070 (~3%) have a higher Fe/Mn of 33.7 and 34.5, while in brecciated, metamorphosed basalt GRO 06059, approximately 21% of the low-Ca pyroxenes have Fe/Mn ~35.0. In contrast, ~21% of low-Ca pyroxenes in unbrecciated basalt Orlando have a lower Fe/Mn of 29.5. The anomalous grains were found by randomly targeting pyroxenes of different textural types in our initial analysis set. We also found two populations of low-Ca pyroxene grains in the gabbro clast from Sioux County. We did not do a random sampling of grains in this clast, but the minority population of low-Ca pyroxene analyses has the lower Fe/Mn as in the case of Orlando. In all cases, the population with the lower Fe/Mn has a higher Fe/Mg and Wo content (Table 3; Fig. 2d).

Of the five eucrites mentioned above, we have done the most detailed study of GRO 06059. It is a brecciated rock containing lithic clasts of differing textures, mineral fragments, and a fine-grained matrix with recrystallized, granoblastic to granulitic texture. Basaltic lithic clasts include very fine-grained variolitic basalts and very fine-grained to fine-grained subophitic basalts. These basaltic clasts include elongate plagioclase grains with only slightly rounded corners indicating minimal grain recrystallization. One incomplete clast on the section edge is a medium-grained gabbroic (?) clast composed mostly of plagioclase containing skeletal, euhedral to subhedral silica grains. The texture is reminiscent of the plagioclase grain from EET 87542 (Fig. 8c). A common lithic clast type is metamorphosed impact melt clasts that contain rounded and/or embayed mineral and lithic fragments in a groundmass of very fine-grained pyroxene and plagioclase with granoblastic texture. Mineral fragments of pyroxene and plagioclase are typically up to 600 μm in size and with slight rounding of angular corners. One large (1.25 mm) pyroxene fragment contains abundant inclusions of troilite, oxides, plagioclase, and silica, and is texturally reminiscent of some large pyroxene clasts in howardites and mesosiderites. Matrix grains generally share the property of slight rounding of grain corners, but some regions have a granoblastic texture indicating more extensive grain recrystallization.

GRO 06059 presents textural evidence suggesting that it might not be a simple monomict eucrite. The variations in textures for basaltic clasts are suggestive of different source rocks for them, although this could be due to sampling regions with different cooling regimes within a single flow/shallow intrusion (cf. Buchanan et al. 2000). The abundance of impact melt material as clasts, rather than intrusive veins, indicates impact gardening and mixing on the surface. This in turn suggests that GRO 06059 is a breccia possibly of distinct basaltic eucrite materials. The one large, inclusion-rich pyroxene clast mentioned above is texturally unlike pyroxenes in the basaltic clasts suggesting a different lithic source. Texturally, the evidence indicates that GRO 06059 might be a polymict breccia.

Despite textural evidence suggesting polymict character for GRO 06059, pyroxene compositional variations are not related to lithic clast, mineral fragment, or impact melt textural elements that might support different source rocks for different clast types. There are two distinct low-Ca pyroxene compositional types. Type-a pyroxenes are more calcic and ferroan, with Fe/Mn within the range of normal basaltic eucrites (Table 3). Type-b low-Ca pyroxenes have anomalously high Fe/Mn, in between values of normal basaltic eucrites and Ibitira (Fig. 2d). Most pyroxenes are type a; the greater number of analyses for type-b pyroxenes (Table 3) is due to targeted sampling in later analyses. Type-a pyroxenes are found in fine-grained lithic clasts with subophitic texture, coarser grained lithic clasts with allotriomorphic texture, lithic clasts entrained in impact melt clasts, and in mineral fragments. Type-b pyroxenes are found in all of these except for the fine-grained subophitic basalt clasts. However, we have done very few pyroxene analyses in only two of these latter clasts. The large, inclusion-rich pyroxene mentioned above appears to be entirely type b in composition. In short, except possibly for the large, inclusion-rich pyroxene clast, we have no documentation that the distribution of pyroxene types is related to lithic clast or mineral fragment type.

Type-a and -b pyroxene compositions are often found as discrete regions within individual pyroxene

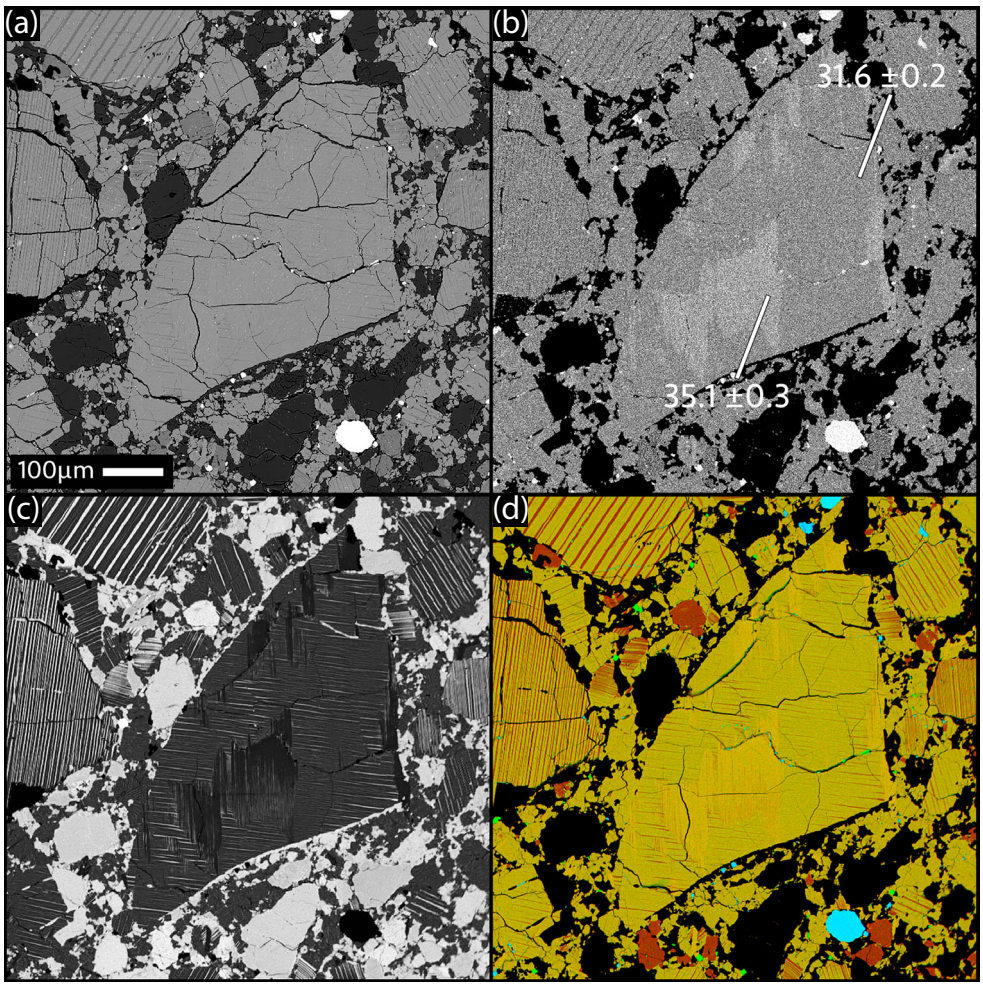

Fig. 14. Backscattered electron image (a), Fe/Mn ratio X-ray map (b), Ca X-ray map (c), and composite Mg (red), Fe (green), and Cr (blue) X-ray map (d) of sector-zoned pyroxene grain in GRO 06059. Average Fe/Mn ratios for host (type a) and zone (type b) are given.

grains and this is a primary igneous feature. Type-b pyroxenes are in irregular patches with sharp and angular boundaries within type-a pyroxene compositions (Fig. 14). This indicates that this is not a metamorphic overprint. The compositions are inconsistent with type-b pyroxenes forming from melt that infilled a skeletal pyroxene phenocryst, as the type-b pyroxenes have lower Fe/Mg and Ca contents—more primitive compositions (Figs. 2d and 15).

The igneous process that we posit is responsible for type-b compositions is a type of sector zoning. Sector zoning is the presence of different compositions in different growth sectors of individual crystals. Sector zones are typically pyramidal in form with broad faces at the crystal margins that taper to points in the interiors (Dowty 1976). Several models have been proposed to explain sector zoning, but experimental work suggests that none are wholly adequate (see Schwandt and McKay 2006). However, models that posit a melt composition boundary layer adjacent to the crystal face caused by sluggish diffusion of multiple elements in the melt are incorrect (Schwandt and McKay 2006). The fundamental mechanism appears to be a combination of (1) rapid crystal growth precluding full equilibrium, (2) slow diffusion of Si in the melt, (3) differences in "protosites" on different crystal faces promoting substitutions for Si in the tetrahedral site, and (4) charge balancing substitutions in the octahedral sites (Dowty 1976; Schwandt and McKay 2006).

Aluminum and Fe^{3+} can substitute for Si in the tetrahedral site (Morimoto et al. 1988), but at the low fO_2 of formation for basaltic eucrites, ~1 log unit below the iron-wüstite buffer (IW-1) (Stolper 1977), Fe^{3+} is not present (Papike et al. 2005). Plausible charge-compensating substitutions for the M1 octahedral site in basaltic eucrites are Al^{3+}, Ti^{4+}, and Cr^{3+} (Morimoto

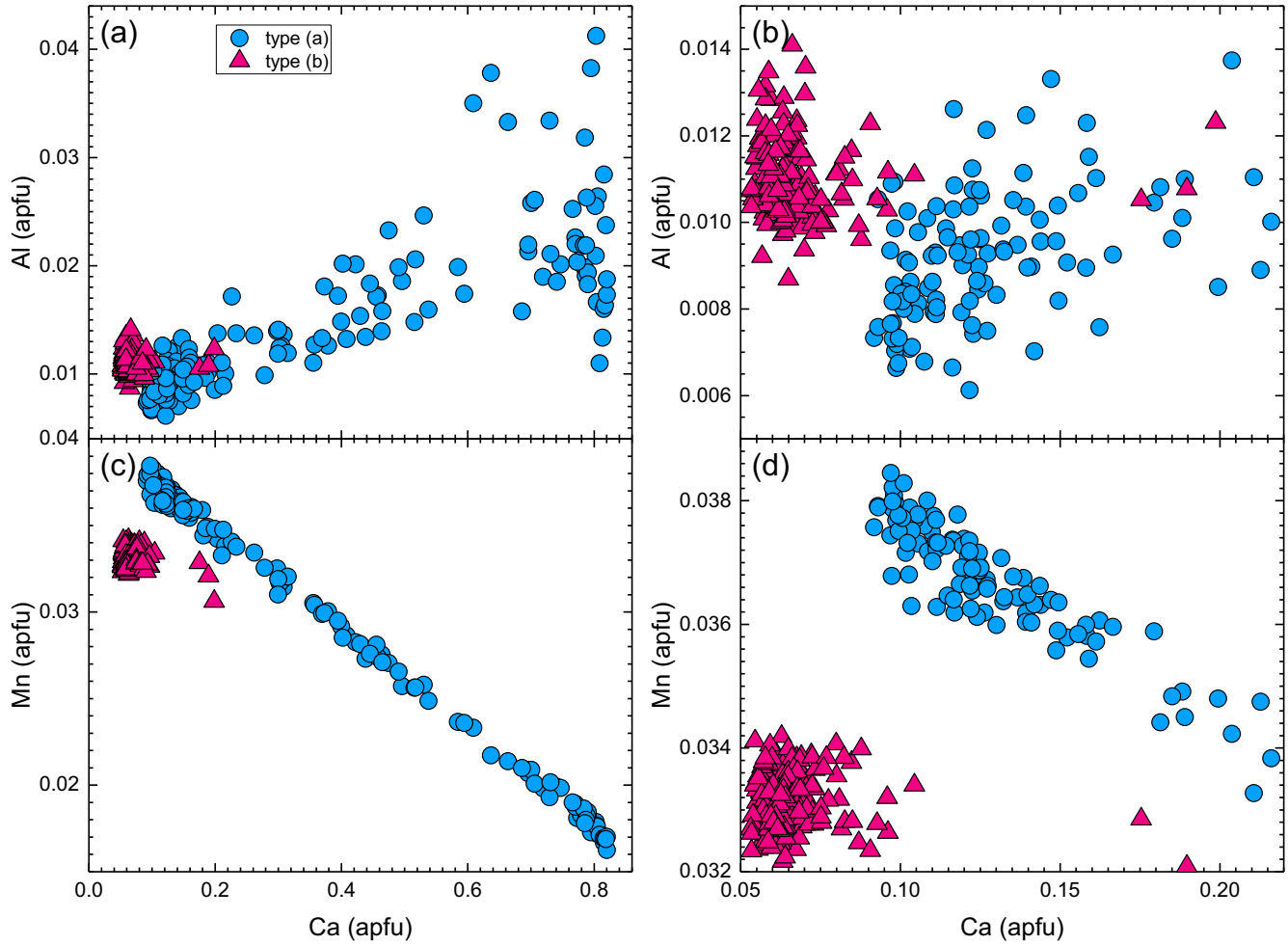

Fig. 15. Aluminum and Mn versus Ca (atoms per formula unit) for pyroxenes in GRO 06059, showing minor element differences between type-a (low Fe/Mn) and type-b (high Fe/Mn) pyroxenes.

et al. 1988; Papike et al. 2005); other highly charged species are too low in abundance to impact pyroxene stoichiometry. Thus, possible charge-coupled substitutions for $^{M1}R^{2+}$-$^{T}Si^{4+}$ are $^{M1}Al^{3+}$-$^{T}Al^{3+}$, $^{M1}Ti^{4+}$-$2^{T}Al^{3+}$, and $^{M1}Cr^{3+}$-$^{T}Al^{3+}$ (cf. Papike et al. 2005). (We have not determined Na in pyroxenes because experience has shown that it is below detection in eucritic pyroxenes, and what little Na is present in pyroxene will be partitioned into augite in favor of low-Ca pyroxenes. Charge compensation in the M1 site for Na^{1+} in the M2 site is not important for these low-Ca pyroxenes.)

The minor elements are in low abundance in these low-Ca pyroxenes: Ti and Cr are each in the range 0.004–0.006 apfu; Al is more abundant at 0.007–0.013 apfu. At these low abundances, uncertainties in analysis of Si preclude the quantitative determination of substitution mechanisms. However, the ranges in Ti and Cr completely overlap in type-a and -b pyroxenes, and thus, there is no evidence for either of these as being important in charge compensation for tetrahedral Al. In contrast, Al is more abundant in type-b pyroxenes (Figs. 15a and 15b) and we thus conclude that the $^{M1}Al^{3+}$-$^{T}Al^{3+}$ couple is the dominant compensation mechanism. Compared with type-a low-Ca pyroxenes, type-b low-Ca pyroxenes have higher Mg, lower Ca and Mn (Figs. 15c and 15d), but overlapping ranges in Fe. Experimental work on pyroxenes shows that pigeonite in equilibrium with orthopyroxene has a higher Fe/Mg (see fig. 5 of Huebner and Turnock 1980), but whether this is accomplished by Mg, Fe, or both is not documented. Based on our analyses, we suggest that Mg partitioning differences dominate.

We have not found an obvious explanation for the difference in Mn partitioning between type-a and -b pyroxenes. The order in which cations fill the M1 and

M2 sites is different for different pyroxene types, but this is mostly controlled by the amount of Ca in the M2 site (Cameron and Papike 1981). The difference in Ca between type-a and -b low-Ca pyroxenes is too small to have a significant impact. Nevertheless, it is the difference in Mn partitioning that gives type b their anomalous Fe/Mn.

Only a few of the eucrite-type achondrites we studied contain two Fe/Mn pyroxene populations, indicating that the process that caused this was uncommon in asteroidal basalts. Thus, the common occurrence of both populations in most textural elements of GRO 06059 supports the case that this is a monomict, not polymict, breccia.

We have not done detailed investigations of the distributions of the minority Fe/Mn populations in CMS 04049, GRO 17070, or Orlando. The distributions of low-Ca pyroxene populations in CMS 04049 and GRO 17070 mimic that of GRO 06059, and it is plausible that a similar type of sector zoning is present in all three. Type-b low-Ca pyroxenes in CMS 04049 have high Al and lower Mn than type-a pyroxenes, identical to the situation for GRO 06059. Unlike GRO 06059, type-b low-Ca pyroxenes have slightly higher mean Ti and Cr contents than do type-a low-Ca pyroxenes, although the ranges partially overlap. Type-b pyroxenes in GRO 17070 have lower Mn contents, but their Al, Ti, and Cr contents overlap with those of type a. The Al, Ti, and Cr contents of type-a and -b low-Ca pyroxenes in Orlando overlap, while Mn and Fe are higher in type b. The cause of the low Fe/Mn population for this eucrite is not known.

Pyroxenes with atypical Fe/Mn are minor components in only some basaltic eucrites. In these basalts, most low-Ca pyroxenes have Fe/Mn within the range of O-normal basaltic eucrites. An incorrect assignment of these basaltic eucrites as being anomalous in Fe/Mn did not (and would not have) occurred.

Paired Eucrite-Type Basalts PCA 82502 and PCA 91007

PCA 82502 is a vesicular basalt composed of sparse microphenocrysts of pigeonite and plagioclase in a very fine-grained subophitic groundmass. Although classified as being unbrecciated, it has a cataclastic texture and is a breccia. Basaltic clasts predominate in our thin section; finely brecciated matrix is very subordinate and can be easily overlooked during preliminary examination. Vesicles are confined to the basaltic clasts. PCA 82502 is tentatively paired with PCA 91081 and PCA 91083, which we have not studied. PCA 91007 is petrologically almost identical to PCA 82502, the most noticeable differences being easily distinguished brecciated matrix and a visually greater matrix/clast ratio in our thin section; PCA 91007 is classified as a brecciated eucrite. Low-Ca pyroxene compositions for PCA 82502 and PCA 91007 are indistinguishable (Table 3; Fig. 2d) and plagioclase compositional distributions overlap. One distinction between them is that chromite and ilmenite average compositions are more ferroan in PCA 91007 (Table 5). We have done fewer analyses of oxide phases in PCA 82502, but their compositional distributions fall within the wider ranges for PCA 91007 oxides. Vesicles are rare in eucrite-type achondrites (see McCoy et al. 2006), which strongly favor pairing these four basalts. Using the terminology of Scott (1984), we conclude that PCA 91007 is probably paired (>95%) with the PCA 82502 pairing group.

PCA 91007 and Pasamonte have similar O-isotope compositions (Scott et al. 2009); PCA 91007 is +4.3 MAD units from the HED igneous median and Pasamonte is at +5.0 MAD units (Table 2). PCA 82502 is less divergent from the HED igneous median but does meet our very conservative limits for identifying outliers (+3.1 MAD units; Table 2). Analyses of different splits of PCA 82502 and PCA 91007 vary in $\Delta^{17}O$, but this variation cannot be ascribed to contamination by terrestrial alteration phases (see discussion in the supporting information). We conclude that this range represents analyses of different splits of a single, moderately heterogeneous basalt. The O-isotope compositions of PCA 82502 and PCA 91007 are consistent with them being paired meteorites, strengthening our petrology-based conclusion. The two PCA basalts have an averaged O-isotope composition with a deviation of +3.7 MAD units from the HED igneous median (Table 2), close to that of Pasamonte. PCA 91007 and Pasamonte have identical Cr-isotope compositions that are distinct from igneous HEDs (Sanborn et al. 2016). The O- and Cr-isotope evidence supports the derivation of Pasamonte and the PCA paired basalts from a different asteroid than O-normal HEDs (cf. Sanborn et al. 2016).

Despite similar O-isotope and Cr-isotope compositions which would allow for derivation from a single homogeneous asteroid, petrologically, the PCA basalts are distinct from Pasamonte. Pasamonte is a fragmental, polymict breccia, not a cataclastic rock. It contains clasts with varying textures and includes rare chondritic clasts (Metzler et al. 1995; Mittlefehldt et al. 2017). The variability of clast textures in Pasamonte contrasts with the uniformity of clasts in the PCA paired meteorites. Furthermore, vesicles are absent in Pasamonte clasts, but given the sizes of the clasts and the low abundance of vesicles in the PCA paired meteorites (0.4 vol% in PCA 91007; McCoy et al. 2006), this is not a persuasive distinction. There

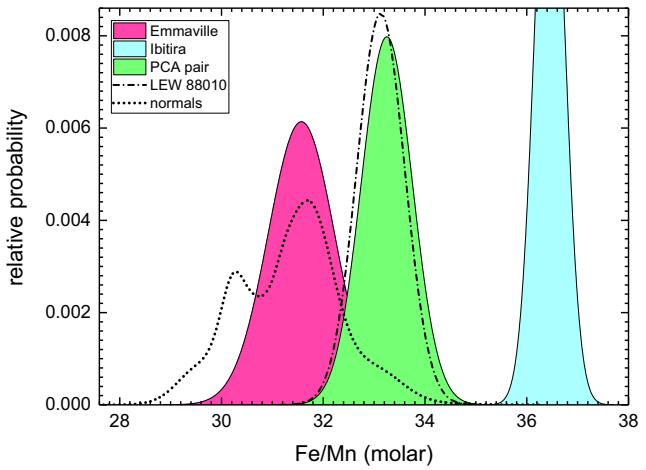

Fig. 16. Probability density function (PDF) plot of low-Ca pyroxene Fe/Mn ratios for the PCA pair compared to summed probabilities for O-isotope normal eucrites. The area under each curve encloses 100% probability that the Fe/Mn ratio lies within the given range. Also shown are PDFs for isotopically anomalous Emmaville and Ibitira, and O normal Stannern group eucrite LEW 88010. Camebax data were excluded from the calculations because some of these analyses have a significant systematic bias compared to the later analyses (e.g., EET 87520, Fig. S1 in the supporting information) and we cannot determine which Camebax data might be biased.

is no compelling textural evidence indicating that Pasamonte and the PCA 82502 pairing group are derived from a single asteroid, but neither is a common source precluded.

The Fe/Mn ratios for low-Ca pyroxenes in PCA 82502 and PCA 91007 lie at the high end of the ranges for eucrites. We determined the distributions of low-Ca pyroxene Fe/Mn ratios using probability density functions (PDF) for individual basaltic eucrites and the combined analyses for PCA 82502 and PCA 91007 (PCA pair). (The calculation of these probability density functions is described in the supporting information.) The PDF for the PCA pair has some overlap with the summed PDFs of O-normal eucrites (Fig. 16). Low-Ca pyroxenes in the PCA pair have an Fe/Mn of 33.2 ± 0.5, which is within range that encompasses 95% of the probability density function for O-normal eucrites (29.2–33.4). The probability density function tail to higher Fe/Mn is due to the Stannern group eucrite LEW 88010, which is indistinguishable from that of the PCA pair (Fig. 16). Other than the higher pyroxene Fe/Mn, there are no petrological, compositional, or isotopic distinctions between LEW 88010 and other Stannern group eucrites, and thus, no reason to suspect it might be anomalous. Because of this, we conclude that the higher pyroxene Fe/Mn for the PCA pair does not require a separate parent asteroid for these meteorites; only O- and Cr-isotopic compositions make this case.

The relationship between the PCA pair and normal eucrites is thus similar to the situation for Emmaville, where mineral compositions, including pyroxene Fe/Mn, are indistinguishable from those of normal eucrites, yet the O-isotope composition is very different (+12.6 MAD units from the HED igneous median; Table 2) (Barrett et al. 2017).

Cumulate Gabbros

We have studied four cumulate gabbros and include older data on two others (Table 1). All of them except ALH 85001 are unbrecciated. Pyroxene compositions from two thin sections of ALH 85001 are consistent with a single source for all grains indicating that it is a monomict breccia. Furthermore, its bulk rock Ca, Sc, and Cr contents plot within fields for cumulate eucrites but not polymict eucrites (Mittlefehldt and Lindstrom 2003), and its highly siderophile element contents are very low compared to those of polymict eucrites, which might contain impactor debris (Warren et al. 2009).

Two of the cumulate gabbros are isotopically anomalous: A-881394 and EET 92023 with O-isotope anomalies of +16.0 and +16.5 MAD units from the HED igneous median (Table 2). A-881394 is well resolved from eucrites and diogenites in ^{54}Cr isotope ratios (Wimpenny et al. 2019). The ^{54}Cr isotope ratio for EET 92023 plots intermediate between those of eucrites and the eucrite-type meteorites A-881394 and Bunburra Rockhole, which have O-isotope ratios like that of EET 92023; within uncertainty, EET 92023 overlaps the fields for both eucrite and eucrite-type achondrites in ε^{54}Cr (Sanborn et al. 2016).

A-881394 is an ancient rock, with a Pb-Pb age of 4565 Ma (Wimpenny et al. 2019). Short-lived ^{26}Al-^{26}Mg and ^{53}Mn-^{53}Cr chronometers give concordant ages (Nyquist et al. 2003; Wadhwa et al. 2009), but these ages are ~1 Ma younger than Pb-Pb ages (Wadhwa et al. 2009; Wimpenny et al. 2019). The latter authors ascribe the difference to a lower closure temperature for the Al-Mg system compared to the U-Pb system, which if correct, would suggest the same for the Mn-Cr system. The formation age for EET 92023 has not been measured; an Ar-Ar age of 3.76 Ga is interpreted to reflect an impact-resetting age (Bogard and Garrison 2009).

A-881394 is petrologically anomalous compared to cumulate eucrites. It has a granular texture, pyroxene has not inverted to orthopyroxene, and augite exsolution lamellae are thin, all distinctions from cumulate eucrites (Takeda et al. 1997; Nyquist et al. 2003). Aluminum, Ti, and Cr contents in A-881394

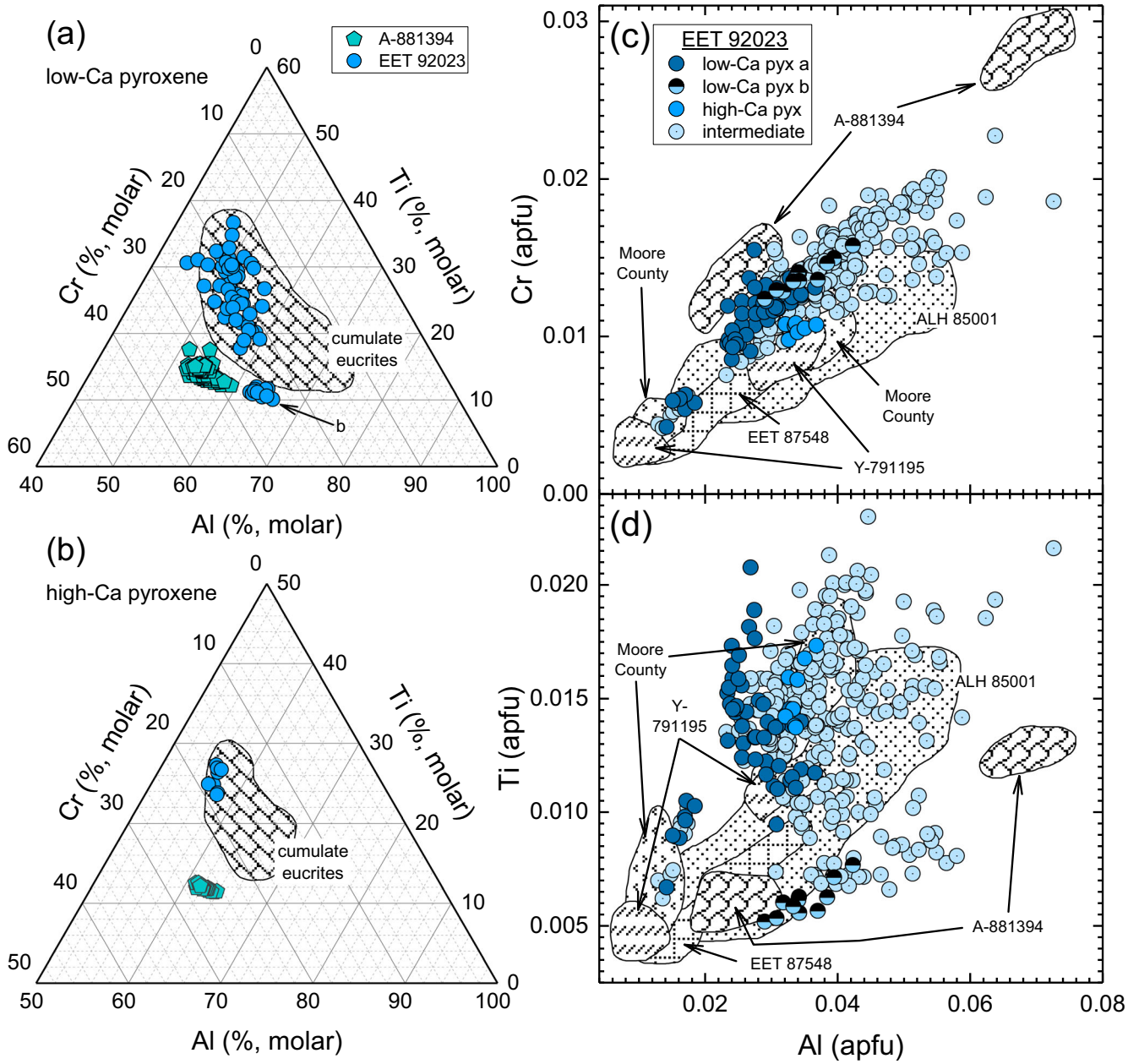

Fig. 17. Pyroxene minor elements in cumulate gabbros. a, b) Ternary plots for low- and high-Ca pyroxenes in A-881394 and EET 92023 compared to fields for cumulate eucrites. Minor elements are calculated as a percentage of the sum of molar Al, Ti, and Cr. Low-Ca pyroxene type b for EET 92023 is distinct from type a (labeled in [a]). Plots of pyroxene Cr versus Al (c) and Ti versus Al (d) for anomalous cumulate EET 92023 compared to fields for individual cumulate eucrites and anomalous cumulate A-881394. For EET 92023, all pyroxene compositions are shown; for all others, only low-Ca and high-Ca pyroxene data were used to construct the fields. ALH 85001 and EET 87548 have partially overlapping fields for low- and high-Ca pyroxenes and continuous fields are shown for them; for all others, the fields are well separated. High-Ca pyroxenes have higher Al, Ti, and Cr contents.

pyroxenes are anomalous compared to cumulate eucrites (Figs. 17a and 17b). Furthermore, A-881394 contains more calcic plagioclase than any eucrite or eucrite-type basalt, including Ibitira (Table 4; Figs. 4b and 4d) (Takeda et al. 1997; Nyquist et al. 2003; Mittlefehldt 2005). The pyroxene textural evidence shows that A-881394 cooled more quickly than cumulate eucrites, which could indicate shallower emplacement in the crust. The very low Na content of plagioclase requires a different parental melt

composition. Bulk rock analyses of A-881394 have lower Na contents than do cumulate eucrites (e.g., Warren et al. 2009). This distinguishes it from cumulate eucrites, which could have formed from typical basaltic eucrites (e.g., Treiman 1997).

EET 92023 is also petrologically anomalous compared to cumulate eucrites. Pyroxene in EET 92023 has not inverted to orthopyroxene and augite exsolution lamellae are thinner than found in cumulate eucrites (Yamaguchi et al. 2017). Most low-Ca pyroxene analyses (type a) have Fe/Mn substantially higher than those of cumulate eucrites, excluding the minor component of Moore County (Fig. 2b). A single grain in EET 92023 (type b) is more magnesian and has lower Fe/Mn. Pyroxenes contain small melt inclusions, which are unusual for cumulate eucrites (Yamaguchi et al. 2017). Plagioclase compositions for EET 92023 show wide ranges in Ab and Or in contrast to other cumulate gabbros (Fig. 4b). Yamaguchi et al. (2017) noted discontinuous Na zoning with Na-K-rich rims in plagioclases for this meteorite. These authors report a K-feldspar composition, but the analysis is too Si-rich for stoichiometric feldspar. The high-K plagioclase analyses shown in Fig. 4b are stoichiometric feldspar, and hint that K-feldspar might be present. The pyroxene textures and plagioclase compositions are consistent with more rapid cooling for EET 92023 compared to cumulate eucrites.

Minor element contents in EET 92023 pyroxene endmembers generally display distribution patterns like those of cumulate eucrites, but intermediate pyroxene compositions do not. Aluminum, Ti, and Cr contents of type-a low-Ca pyroxenes and high-Ca pyroxenes fall within the fields of cumulate eucrites (Figs. 17a and 17b). Minor element contents of type-a low-Ca pyroxenes are lower than those of high-Ca pyroxenes, yielding semilinear Cr-Al and Ti-Al distributions like those for other cumulates (Figs. 17c and 17d). Type-b low-Ca pyroxenes fall outside the field of cumulate eucrites at lower Ti contents (Fig. 17a) and are lower in Ti than type-a low-Ca pyroxenes (Fig. 17d). For cumulate eucrites and A-881394, pyroxenes with Ca contents intermediate between the low- and high-Ca endmembers also have intermediate Al, Ti, and Cr contents caused by electron beam overlapping the two endmembers. The situation is much different for EET 92023; analyses with intermediate Ca contents can have minor element contents higher than those of endmembers (Figs. 17c and 17d). Many intermediate pyroxenes have higher Al and Cr than the high-Ca pyroxenes, but the Cr-Al distribution is still semilinear. The Ti-Al distribution shows no coherent pattern; Ti contents vary widely in analyses with similar Al contents. This distribution is unlike that of any other eucrite-type achondrite in this study with the exception of unequilibrated basaltic eucrite EET 92003.

The most anomalous petrologic characteristic of EET 92023 is that it contains relatively coarse-grained, Ni-rich metal not known from other unbrecciated or monomict, basaltic, or cumulate eucrites (Table S4; Kaneda and Warren 1998; Mayne et al. 2009; Yamaguchi et al. 2017; this study). Non-polymict eucrites typically contain $\leq$0.3 vol% metal (Delaney et al. 1984), which is usually in grains of a few to a few tens of microns in size; most metal grains contain $\leq$1 wt% Ni (Duke 1965; Mayne et al. 2009; this study). Exceptional basaltic eucrite Camel Donga contains about 1 vol% metal containing up to ~0.6 wt% Ni (Cleverly et al. 1986; Palme et al. 1988; Warren et al. 2017). EET 92023 contains ~0.5 wt% metal that is up to ~300 μm across (Kaneda and Warren 1998) and forms composite grains of kamacite, taenite, and probable tetrataenite (Mayne et al. 2009; Yamaguchi et al. 2017; this study). Whole-grain Ni contents are >4 wt%, using the lowest average kamacite composition determined by us as the lower limit. The Ni-rich metal demonstrates the presence of a component not known from any other eucrite.

Average low-Ca pyroxene Fe/Mn for A-881394 is moderately higher than a model for cumulates from normal basaltic eucrites predicts (Fig. 2b). This model is based on pyroxene/melt Fe/Mg and Fe/Mn partition coefficients calculated from experiments on natural eucrites (Stolper 1977). A small amount of pyroxene was iteratively removed from a eucrite melt composition (Sioux County basalt; Mittlefehldt et al. 1998a) and the remaining melt composition adjusted accordingly to derive the curve shown in Fig. 2b. The model is semiquantitative, but it adequately mimics the low-Ca pyroxene compositions for cumulate eucrites and magnesian-pyroxene core compositions for Stannern group eucrite QUE 94484. These cumulate eucrites are consistent with the accumulation of pigeonite and plagioclase from main group eucrites that includes a small amount of trapped melt (cf. Treiman 1997; Mittlefehldt and Lindstrom 2003). The black dots connected by tie lines to meteorite symbols are estimated bulk pyroxene compositions. These were calculated by estimating a mixing ratio for low- and high-Ca pyroxene for each meteorite based on compositions of pyroxenes from melting experiments on Sioux County (Stolper 1977). Low- and high-Ca pyroxene endmembers for each cumulate were combined in proportions to yield a bulk composition that follows the track of experimental pyroxenes on a pyroxene quadrilateral diagram. A-881394 low-Ca pyroxenes and estimated bulk pyroxenes plot above the model curve indicating that its parent melt was distinct from basaltic eucrites in Fe/Mn.

EET 92023 contains two low-Ca pyroxene compositions and both are distinct from the model curve (Fig. 2b). Type-b pyroxene analyses are from a single grain, which has an Mg-Mn-Fe composition like that of A-881394. Type-a pyroxene analyses have Fe/Mn much higher than the model curve, and a substantially higher Fe/Mg than the type-b pyroxenes. The type-a pyroxenes cannot be formed through oxidation of metal plus reaction with free silica that then homogenize with type-b pyroxene. The model for this process reaches a type-a Fe/Mn at Fe/Mg far too low (Fe oxidation, Fig. 2b). We conclude that the type-a pyroxene compositions are anomalous and were formed in a melt with elevated Fe/Mn compared to basaltic eucrites.

Yamaguchi et al. (2017) concluded that EET 92023 likely represents a mixed lithic type formed through impact of a metal-rich impactor onto a mafic crust. These authors showed that some plagioclase grains include irregularly shaped Ca-rich cores which they interpreted as restites from a melting episode. The type-b pyroxene could be a similar relict, but additional work would be needed to test this hypothesis. The melt inclusions in pyroxene identified by Yamaguchi et al. (2017) attest to rapid cooling of a melt allowing for entrapment of melt pockets by growing crystals. The very chaotic minor element contents in EET 92023 pyroxenes compared to what we observe for all other cumulate and basaltic achondrites are consistent with rapid, disequilibrium crystallization. Furthermore, the wide range in plagioclase compositions, as observed for basaltic eucrites but not for cumulate gabbros (Table 4), supports more rapid crystallization for EET 92023. Yamaguchi et al. (2017) concluded that the pre-impact protolith of EET 92023 was a cumulate gabbro. Mittlefehldt and Lindstrom (2003) showed that EET 92023 has higher incompatible trace lithophile element contents than would a model cumulate and concluded that EET 92023 includes a trapped melt component. Considering the new evidence that EET 92023 was formed by impact melting, a more likely scenario is that this rock is a polymict mixture of cumulate gabbro and basalt from the parent asteroid crust and a metal impactor. Like Yamaguchi et al. (2017), we consider the anomalous O-isotope composition to be that of the EET 92023 parent asteroid, which is anomalous in Fe/Mn compared to O-normal eucrites. The Cr-isotope composition of that asteroid is also anomalous compared to normal eucrites (Sanborn et al. 2016).

Finally, Moore County also contains two low-Ca pyroxene types, with the type-b pyroxenes being represented by several analyses from two of the eight grains analyzed. Moore County type-b pyroxenes have Fe/Mn like that of EET 92023 type-a pyroxenes but have a different origin. Moore County type-b analyses have lower Mn and higher Al than type-a pyroxenes as is the case for the two pyroxene types in GRO 96059 discussed above. The origin of type-b pyroxenes in Moore County is plausibly the same as those in GRO 96059, sector zoning.

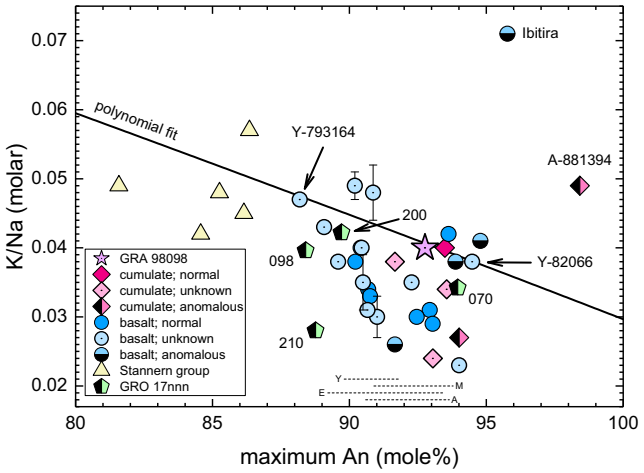

Fig. 18. K/Na versus An for averages of the five most calcic plagioclase analyses for each meteorite studied here. The polynomial fit line to GRA 98098 analyses (solid line), and the complete An ranges for the four cumulate eucrites ALH 85001, EET 87548, Moore County, and Y-791195 (light dashed lines at the bottom) are shown for comparison. Error bars on K/Na are shown for a few select basaltic eucrites. The GRO 17 eucrites are identified by the last three digits of their names.

Plagioclase Compositions and Eucrite Formation

Plagioclase compositions display an array of variations within the suite of eucrites that reveal clues to their crystallization histories (Table 4; Fig. 4). The most calcic plagioclases in many basaltic eucrites overlap the range for cumulate eucrites (Fig. 18), and some match the most calcic plagioclases produced in melting experiments on basaltic eucrites, An_{94} (Stolper 1977). This indicates that plagioclases more faithfully record initial magmatic compositions than do pyroxenes. Furthermore, plagioclase in basaltic eucrites can have substantial ranges in composition even for those rocks containing equilibrated pyroxenes, for example, GRA 98098. These characteristics are understandable because of the slower diffusion rates in plagioclase due to the necessity for coupled CaAl-NaSi diffusion (e.g., Grove et al. 1984). This enables plagioclase to more closely retain liquidus compositions in core regions and record compositional variations accrued during crystallization.

The highest maximum plagioclase Ca contents for main group eucrites vary from $An_{94.5}$ for Y-82066 to

$An_{88.2}$ for a metabasalt clast from Y-793164 (Fig. 18). Y-82066 is a primitive main group eucrite like the Sioux County basalt clasts as judged by its low bulk rock incompatible trace lithophile element contents and higher mg# (Mittlefehldt and Lindstrom 1993). Two other basaltic eucrites contain plagioclase with maximum An contents like those of near-liquidus experimental plagioclase, EET 92003 ($An_{94.0}$) and CMS 04049 ($An_{93.6}$). EET 92003 is petrologically anomalous in its pyroxene compositions (Fig. 3d). The Y-793164 basalt clast is intermediate between primitive main group eucrites and the residual melts of the Nuevo-Laredo group eucrites (Mittlefehldt and Lindstrom 1993). These authors concluded that Y-793164 basalt clast could represent a melt residual from 25% to 30% crystallization of a eucrite like Y-82066. The lower An content of the most calcic plagioclase in Y-793164 reflects loss of the earliest crystallized grains.

The most calcic plagioclase compositions for Stannern group eucrites are more sodic than those of main group eucrites, including the ferroan-basalt clast from Y-793164 (Fig. 18) (see also Delaney et al. 1981a). The substantially less-calcic compositions for Stannern group eucrite plagioclases indicate that their parent magmas had a higher albite/anorthite component ratio than did main group eucrites. This is consistent with the melt hybridization model for formation of Stannern group eucrites (Barrat et al. 2007). In this model, initial melts of main group eucrite composition (melt i) interact with earlier formed basalts, which are partially melted. The crustal melts (melt c) are mixed with melt i to form a hybrid composition (melt h) containing enhanced incompatible trace element contents, but major element contents only modestly changed. This process hypothesized for generation of Stannern group eucrites (Barrat et al. 2007) is an AFC process. An important component of the heat needed to assimilate the country rock is provided by latent heat of crystallization of the intruding magma (DePaolo 1981). In the case of Stannern group eucrite formation, melt i would be crystallizing pyroxene and plagioclase (Stolper 1977). This ought to result in the most calcic plagioclase compositions being like those in main group eucrites, contrary to observations. Our observations suggest that the assimilation process includes exchange between melt i and the country rock, rather than strictly being due to crystallization and partial melting:

$$CaAl_2Si_2O_{8\,\mathrm{melt\ i}} + NaAlSi_3O_{8\,\mathrm{crust}} = NaAlSi_3O_{8\,\mathrm{melt\ h}} + CaAl_2Si_2O_{8\,\mathrm{crust}}.$$

The enthalpy of fusion of anorthite is greater than that of albite (e.g., Bouhifd et al. 2007) and this reaction would thus provide energy to promote the AFC process.

There are significant variations in K/Na for the most calcic plagioclases within the suite (Fig. 18). Plagioclase was the first Na- and K-bearing phase to crystallize from eucritic magmas, and the differences in K/Na plausibly reflect variations in magma composition. Some of this variation might be caused by fractionation of the eucrite suite during crystallization; the basaltic eucrites with the highest K/Na tend to have more sodic compositions in their maximum An plagioclases. However, there are also real differences in K/Na for plagioclases with similar An contents, for example, plagioclases in several eucrites with maximum $An_{90\text{-}91}$ have well-resolved K/Na (symbols with error bars, Fig. 18). Plagioclase K/Na depends on melt K/Na, plagioclase An, and T of formation (Sato 1984). Liquidus temperatures for basaltic eucrites are similar (Stolper 1977), and therefore, the difference K/Na for the $An_{90\text{-}91}$ plagioclases indicates differences in parent melt K/Na.

Plagioclases in many of eucrite-type achondrites contain high-K regions (Table 4; Fig. 4). These are uncommon in cumulate eucrites and highly metamorphosed basaltic eucrites but occur in about half of the basaltic eucrites. Stannern group eucrite plagioclases commonly contain high-K regions (Table 4; Fig. 4b), and in this, they are distinct from most other basaltic eucrites. The highest Or content found in a main group eucrite is $Or_{\sim 19}$ for MIL 05041, and in a Stannern group eucrite is $Or_{\sim 33}$ for PCA 91179. These analyses likely reflect partial beam overlap on potassium feldspar grains. Potassium feldspar grains <10 μm in size are present in several eucrites but are more abundant in Stannern group eucrite PCA 91179 than in main group eucrites (McQuaig et al. 2019). Potassium feldspar has only rarely been reported from eucrites and is generally poorly described. Our results and those of McQuaig et al. (2019) suggest that this phase might be more common in eucrites than generally thought.

Implications for Eucrite-Type Achondrite Petrogenesis

The consensus view is that eucrites represent residual melts from crystallization of a magma ocean on their parent asteroid (e.g., Righter and Drake 1997; Ruzicka et al. 1997), with an alternate hypothesis being that they represent primary partial melts of a primitive asteroid (Stolper 1977). The magma ocean hypothesis is supported by two key observations (1) the homogeneity of O-isotope compositions of igneous HEDs is best explained by homogenization in a magma ocean (>50% melting; Greenwood et al. 2005); and (2) the moderately siderophile element (Ni, Co, Mo, W, P) contents of

basaltic eucrites are best explained by prior extraction of a metallic core (Righter and Drake 1996), and are inconsistent with equilibration with solid metal in a chondritic source region (McSween et al. 2011). The range of core masses derived from siderophile element modeling (Righter and Drake 1997) encompasses that determined for Vesta from Dawn data (Russell et al. 2012), lending credence that the modeling accurately simulates asteroid differentiation processes. The moderately siderophile element argument has been strengthened by recent modeling that shows that the abundances of eight moderately siderophile elements in basaltic eucrites can be matched only when their parent asteroid undergoes melting to form a deep magma ocean requiring >50% melting (Steenstra et al. 2016). The observation that supports the partial melt hypothesis is that melting experiments establish that basaltic eucrites are multiply saturated with olivine, pyroxene, plagioclase, Cr-rich spinel, and metal on their liquidi, consistent with equilibration with a melting residue of a primitive, chondritic asteroid (Stolper 1977). We will examine the extent to which our results might distinguish between these hypotheses.

The oxygen isotope argument cannot be used to claim a magma ocean origin for the anomalous eucrite-type basalts and gabbros because there are too few of them to demonstrate O-isotope homogeneity within any grouping (Fig. 1). In some cases, $\Delta^{17}O$ identity exists—the A-881394, Bunburra Rockhole, and EET 92023 trio, for example (Fig. 1)—but these rocks are petrologically and compositionally distinct (Bland et al. 2009; Benedix et al. 2017; this study) suggesting that they likely hail from different parent asteroids. A partial melt origin is viable for the O anomalous eucrite-type achondrites based solely on this parameter, but a magma ocean origin is not precluded.

The O anomalous eucrite-type basalts Bunburra Rockhole, Ibitira, Pasamonte, and the PCA pairing group have Co contents like basaltic eucrites (5.1–9.6 $\mu g\ g^{-1}$ compared with 2.6–8.8 $\mu g\ g^{-1}$; database of Mittlefehldt [2015]; original data sources given therein). These are substantially lower than the 14.5–23 $\mu g\ g^{-1}$ calculated for melts in equilibrium with metal-bearing chondritic sources (McSween et al. 2011), arguing against a partial melt origin for these basalts. Note that Ibitira is multiply saturated on its liquidus with phases consistent with its being a primary partial melt of a chondritic source, while Pasamonte and Emmaville are more evolved compositions (Stolper 1977).

Righter and Drake (1997) considered the physics of magma oceans on Vesta-sized asteroids and concluded that the magmas would be vigorously convecting. Crystals formed during cooling would be entrained in the convecting system, and for this reason, Righter and Drake (1997) modeled initial crystallization of the magma ocean as an equilibrium process. Convective lockup occurred when ~20% melt remained, and this melt, which was basically eucritic in composition, underwent fractional crystallization (Righter and Drake 1997). As equilibrium crystallization is thermodynamically equivalent to equilibrium partial melting in reverse, the Righter and Drake (1997) model is consistent with the experimental results of Stolper (1977). A possible exception is that metal would not be saturated in the silicate melt at ~20% equilibrium crystallization because the metal–sulfide core segregated much earlier from the silicate system. However, metal in most basaltic eucrites is typically a late-stage phase interstitial between pyroxene and plagioclase (Duke 1965), and the petrographic evidence does not strongly support saturation of metal on basaltic eucrite liquidi.

Ashcroft and Wood (2015) have done a combined experimental and modeling study of eucrite and diogenite petrogenesis and find some concordance with Righter and Drake (1997). They found that equilibrium partial melting of 45% (or equilibrium crystallization until 45% melt remains) followed by fractional crystallization could result in the formation of diogenites and eucrites. The distinction between these authors' model and that of Righter and Drake (1997) is that the latter form diogenites as part of the equilibrium crystallization process. For the reasons discussed by Stolper (1977), it is difficult to derive eucritic compositions that are saturated in olivine by a fractional crystallization process that first produced diogenites. Indeed, the experiments run by Ashcroft and Wood (2015) to simulate diogenite and eucrite formation are not saturated in olivine as are the more primitive (Mg-rich) main group eucrites (Stolper 1977).

Ashcroft and Wood (2015) tested a wider range of compositions than those studied experimentally through modeling and found that changing the major element compositions of the starting silicates by up to 10% relative for individual oxide components could still result in differentiation sequences that could produce diogenites and eucrites. This indicates that a range of parent asteroids could be modestly different in bulk composition and yet produce mineralogically indistinguishable basalts. Thus, the modeling of Ashcroft and Wood (2015) provides a ready explanation for the petrologic and isotopic observations presented here. A family of asteroids showing variations in major element and/or isotopic composition produced a suite of very similar basalts by very similar differentiation processes. Some of the basalts are petrologically identical but isotopically distinct, while others are petrologically and isotopically distinct. The corollary, of course, is that there could be basalts that are

petrologically and isotopically identical yet are derived from different asteroids; we would have no way to distinguish them unless the subsequent histories (impact, etc.) of the two asteroids were quite different. Mesosiderites and HEDs might be an example of this (see next section).

Of necessity, petrologic modeling of asteroid differentiation greatly simplifies nature. Thus, even a relatively complex model (e.g., Mandler and Elkins-Tanton 2013) cannot easily explain all details of geochemistry (see Barrat and Yamaguchi 2014). We have shown here that the same applies to petrology. For example, QUE 94484 followed a slightly different crystallization path than typical eucrites caused by a higher than typical S content in its magma. We have posited that the high S content was engendered by the magma hybridization process that produced this Stannern group eucrite, but in general, Stannern group eucrites do not have higher modal troilite contents than main group eucrites (data from Delaney et al. 1984). Thus, a small stochastic variation in QUE 94484's evolution from the norm resulted in a quite noticeable difference in petrology. Because of this, our petrological data cannot be used to provide definitive tests of competing formational hypotheses for eucrite-type achondrites.

Mesosiderite Connections?

As discussed above, three of the eucrite-type achondrites we have studied are metal- and/or troilite-rich rocks: EET 92023, EET 87542, and QUE 94484. The latter two contain low-Ca pyroxenes with low Fe/Mn (Fig. 2) as do many mafic clasts in mesosiderites (Mittlefehldt 1990; Rubin and Mittlefehldt 1992), and an origin as a clast from a mesosiderite has been considered for EET 92023 (Mittlefehldt and Lindstrom 1996; Kaneda and Warren 1998). Thus, we address possible mesosiderite connections for these three rocks.

Although it contains coarse, Ni-rich metal, EET 92023 is highly unlikely to have been derived from the mesosiderite parent asteroid. Mesosiderites have O-isotope compositions indistinguishable from those of HEDs (Greenwood et al. 2006, 2017) while EET 92023 is anomalous (+16.5 MAD units, Table 2). Thus, the same arguments raised by Scott et al. (2009) favoring distinct asteroidal sources for O-anomalous basalts apply to EET 92023 in relation to mesosiderites. Furthermore, Fe/Mn ratios in low-Ca pyroxenes of EET 92023 are higher than those of cumulate eucrites, while those of mesosiderite mafic clasts are much lower (Figs. 2a and 2b) (Mittlefehldt 1990; Yamaguchi et al. 2017). Finally, the cooling rate of metal in EET 92023 is about one order of magnitude faster than that of mesosiderites (Yamaguchi et al. 2017). Thus, we conclude that EET 92023 is not related to mesosiderites.

QUE 94484 is rich in silica–troilite mesostasis and mesosiderites contain abundant troilite (table 41, Mittlefehldt et al. 1998b) and their silicate fraction has higher modal silica than do the petrologically similar howardites (Prinz et al. 1980). However, QUE 94484 is petrologically unlike mafic clasts from mesosiderites. QUE 94484 is an unequilibrated basalt as demonstrated by its pyroxene compositional distribution (Fig. 3b), which is like that of type 2 eucrite pyroxenes (Takeda and Graham 1991). In contrast, mesosiderite silicates are typically metamorphosed (Floran 1978) and basaltic clasts from the least metamorphosed mesosiderites are equilibrated (Mittlefehldt 1979, 1990). Furthermore, the metal in QUE 94484 is Co- and Ni-free (Table S4), quite different from the Co- and Ni-bearing metal in mesosiderites (Hassanzadeh et al. 1990). We conclude that QUE 94484 is not related to mesosiderites.

In some respects, EET 87542 is petrologically like mesosiderites in that it is an equilibrated basalt (Fig. 3a) with very low Fe/Mn in its pyroxenes (Fig. 2). Pyroxene Fe/Mn is, however, lower than any measured for mesosiderite mafic clasts. As was the case for QUE 94484, metal in EET 87542 is Co- and Ni-free (Table S4) and quite unlike that of mesosiderites. Again, we conclude that there is no connection with mesosiderites for this eucrite.

Above we mentioned that it is conceivable that petrologically, compositionally, and isotopically identical basalts might be derived from different asteroids. The HEDs and mesosiderites could represent such a case. As mentioned above, these two groups have identical O-isotope compositions (Greenwood et al. 2006, 2017). Some mesosiderite basalt and gabbro clasts are petrologically and compositionally like basaltic and cumulate eucrites (Mittlefehldt 1979, 1990; Rubin and Mittlefehldt 1992). However, many of the basalt and gabbro clasts in mesosiderites are secondary igneous rocks that were formed by remelting the crust of their asteroid after metal silicate mixing (e.g., Mittlefehldt 1990; Rubin and Mittlefehldt 1992). The post-differentiation history of the mesosiderite parent asteroid was considerably different from that of the HED parent asteroid, and it is unlikely that they are derived from the same asteroid (Mittlefehldt 1990; Rubin and Mittlefehldt 1993).

CONCLUSIONS

We undertook our studies with three goals in mind: (1) to determine the extent to which anomalous O-isotope compositions of eucrite-type achondrites can be

correlated with anomalous petrologic characteristics, (2) to provide details into causes of petrologic anomalies among eucrite-type achondrites, and (3) develop further insight into magmatic processes on asteroids. Because pyroxene Fe/Mn has been shown to be efficacious in determining parent body parentage for basalts (Papike et al. 2003) and has found some utility in establishing petrologic distinctions between eucrite-type achondrites with anomalous O-isotope compositions (Yamaguchi et al. 2002; Mittlefehldt 2005), a major part of our focus was on this parameter. Furthermore, we did additional O-isotope analyses on a suite of eucrite-type achondrites including some which exhibited unusual petrologic properties.

Our studies support the following conclusions:

1. Two basaltic eucrites have HED-normal O-isotope compositions yet are petrologically quite anomalous: EET 87542 and QUE 94484. They are within ±1 MAD unit of the HED igneous median. Both contain low-Ca pyroxenes with Fe/Mn far from the basaltic eucrite range of 30–32; EET 87542 uniformly at 18.6; QUE 94484 variable, but as low as 21.9 for ferroan pigeonite. The low pyroxene Fe/Mn was engendered by parent body processes acting on typical basaltic eucrites: solid-state reduction by S gas for EET 87542; reduction during crystallization by S in the magma for QUE 94484. This demonstrates that stochastic differences in processes can cause substantial localized petrological changes on individual asteroids.
2. Evidence from EET 87542 and QUE 94484 points to an important role for S in modifying the petrology of eucrites, potentially leading to erroneous conclusions regarding parent body parentage of bona fide eucrites. The S geochemistry of the HED parent asteroid, which might be 4 Vesta, is presently poorly known. Most eucrite magmas appear to have been close to sulfide saturation. Some eucritic melts, such as QUE 94484, may have had higher S contents, which caused loss of FeO from the silicate magma to an immiscible sulfide melt, causing a drop in the Fe/Mn ratio of the silicate system. The solid-state reduction of FeO in the EET 87542 protolith during metamorphism adds to evidence (e.g., Zhang et al. 2013) that S gas was a locally important reducing agent in the HED parent asteroid crust.
3. Although initial descriptions for PCA 82502 and PCA 91007 differ, they are petrologically identical clast-rich cataclastic breccias composed of vesicular, very fine-grained basalts. Vesicles are very rare in eucrites (McCoy et al. 2006). Pyroxene compositions are identical for these two basalts, and plagioclase, ilmenite, and chromite compositional ranges and O-isotope compositions overlap. These meteorites are paired with a high degree of confidence. The PCA 82502 pairing group includes PCA 91081 and PCA 91083. PCA 82502 and PCA 91007 have moderately variable O-isotope compositions that are not caused by terrestrial alteration. Low-Ca pyroxenes in the PCA pair have Fe/Mn of 33.2 that overlaps a range that encompasses 95% of the probability density function for O-normal eucrites (29.2–33.4). We cannot conclude that the PCA pair is anomalous in Fe/Mn, and thus, anomalies in pyroxene Fe/Mn and O-isotope composition are not coincident. Pasamonte is also in the PCA isotopic group (Scott et al. 2009; Sanborn et al. 2016; Greenwood et al. 2017), but petrologically these rocks are distinct.
4. We confirm the petrological anomalies of cumulate gabbro EET 92023 noted by others (Kaneda and Warren 1998; Mayne et al. 2009; Yamaguchi et al. 2017), and find that it is also anomalous compared to cumulate eucrites in pyroxene Fe/Mn and minor element distribution patterns, and in the ranges of plagioclase Ab and Or components. We also confirm the anomalous O-isotope composition previously reported for this rock (Greenwood et al. 2017). We concur with Yamaguchi et al. (2017) that EET 92023 was formed by mixing of a metal impactor into a mafic crust, but we find that the silicate fraction was likely a polymict mixture of cumulate and basaltic materials. The high Fe/Mn of the low-Ca pyroxenes cannot have been generated by interaction with oxidized impactor metal on normal eucritic pyroxenes. Rather the crust was anomalous in this parameter compared to the HED parent asteroid. EET 92023 is a case where anomalies in pyroxene Fe/Mn and isotopic compositions are coincident.
5. Plagioclase compositions are more faithful recorders of initial igneous compositions than are pyroxenes, even for many metamorphosed basaltic eucrites. The most calcic plagioclase analyses for each meteorite show that some basalts have maximum-An plagioclases that are identical to those of cumulate eucrites and to near-liquidus plagioclases from melting experiments on eucrites (Stolper 1977). This indicates that liquidus plagioclase compositions are preserved in some basalts. Other basalts, such as a ferroan clast from Y-793164, contain more sodic maximum-An plagioclases, which can be interpreted as these rocks being residual melts after pyroxene–plagioclase fractionation to produce cumulate gabbros. The K/Na ratio for eucrite plagioclases can be different for analyses with the same An content, indicating that initial magma K/Na varied within the basalts. Stannern group eucrites contain maximum An-plagioclases that

are more sodic than those of main group eucrites, including the evolved basalt clast from Y-793164. This is compatible with the hypothesis for Stannern group magma formation via mixing of primary basalts with crustal partial melts (Barrat et al. 2007). The lack of more calcic plagioclase in Stannern group eucrites suggests that reactive exchange of the anorthite component of the primary melt and the albitic component of the crust occurred.

6. We find that low-Ca pyroxenes in basaltic eucrites have a relatively narrow range in Fe/Mn of 29.2–33.4 that encompasses 95% of the probability density function for O-normal eucrites. However, small-scale processes can affect pyroxene Fe/Mn. Five basalts, a gabbro clast from Sioux County, and Moore County contain two distinct populations of low-Ca pyroxene Fe/Mn. In all cases, most analyses (type a) fall within the ranges for eucritic basalts or cumulates. For three—CMS 04049, GRO 96059, and Moore County—the minor component (type b) has higher Fe/Mn, while for Orlando, GRO 17070, and the gabbro clast from Sioux County, the type-b pyroxenes have lower Fe/Mn. Evidence from GRO 96059 shows that the cause of the distinction is sector zoning in which patches within grains of type-a compositions (Fe/Mn = 31.5) have low Ca and Mn, and high Mg and Al. High Fe/Mn ratios in these zones (35.0) are caused by low Mn contents. This could not cause misidentification of a basalt as having anomalous Fe/Mn because the type-b pyroxenes are a minor component.

Acknowledgments—We thank the National Science Foundation and NASA for funding the ANSMET collecting teams that brought back the Antarctic samples studied here, and the Meteorite Working Group, NASA-Johnson Space Center, and the National Museum of Natural History (Smithsonian Institution) for allocation of the samples. We thank the Arizona State University Center for Meteorite Studies, the British Museum (Natural History), the Smithsonian Institution, and M. E. Zolensky for the loan of some of the samples used in this study. We thank J. Malley for his help with oxygen isotope analysis work. We thank K. Righter for providing an internal review of a section added during revisions after the journal reviews. We thank the Associate Editor C. Goodrich, and the reviewers R. Mayne, A. H. Treiman, and A. Zhang for their comments on this manuscript which helped us improve it. Support for this research was provided by NASA's Emerging Worlds Program to DWM, and the Planetary Science Research Program. Oxygen isotope studies at the Open University are funded via Consolidated Grant ST/T000228/1 from the UK Science and Technology Facilities Council.

Data Availability Statement—The data that support the findings of this study are openly available in Interdisciplinary Earth Data Alliance (IEDA) at https://doi.org/10.26022/IEDA/111901.

Editorial Handling—Dr. Cyrena Goodrich

REFERENCES

Ashcroft H. O. and Wood B. J. 2015. An experimental study of partial melting and fractional crystallization on the HED parent body. *Meteoritics & Planetary Science* 50:1912–1924.

Barrat J. A. and Yamaguchi A. 2014. Comment on "The origin of eucrites, diogenites, and olivine diogenites: Magma ocean crystallization and shallow magma processes on Vesta" by BE Mandler and LT Elkins-Tanton. *Meteoritics & Planetary Science* 49:468–472.

Barrat J. A., Jambon A., Bohn M., Blichert-Toft J., Sautter V., Göpel C., Gillet P., Boudouma O., and Keller F. 2003. Petrology and geochemistry of the unbrecciated achondrite Northwest Africa 1240 (NWA 1240): An HED parent body impact melt. *Geochimica et Cosmochimica Acta* 67:3959–3970.

Barrat J. A., Yamaguchi A., Greenwood R. C., Bohn M., Cotten J., Benoit M., and Franchi I. A. 2007. The Stannern trend eucrites: Contamination of main group eucritic magmas by crustal partial melts. *Geochimica et Cosmochimica Acta* 71:4108–4124.

Barrett T. J. 2018. *The history of water and other associated volatiles in howardite-eucrite-diogenite meteorites*. Ph.D. thesis, The Open University, Milton Keynes, UK.

Barrett T. J., Mittlefehldt D. W., Greenwood R. C., Charlier B. L. A., Hammond S. J., Ross D. K., Anand M., Franchi I. A., Abernethy F. A. J., and Grady M. M. 2017. The mineralogy, petrology, and composition of anomalous eucrite Emmaville. *Meteoritics & Planetary Science* 52:656–668.

Benedix G. K., Bland P. A., Friedrich J. M., Mittlefehldt D. W., Sanborn M. E., Yin Q. Z., Greenwood R. C., Franchi I. A., Bevan A. W. R., Towner M. C., Perrotta G. C., and Mertzman S. A. 2017. Bunburra Rockhole: Exploring the geology of a new differentiated asteroid. *Geochimica et Cosmochimica Acta* 208:145–159.

Bland P. A., Spurny P., Towner M. C., Bevan A. W. R., Singleton A. T., Bottke W. F., Greenwood R. C., Chesley S. R., Shrbeny L., Borovicka J., Ceplecha Z., McClafferty T. P., Vaughan D., Benedix G. K., Deacon G., Howard K. T., Franchi I. A., and Hough R. M. 2009. An anomalous basaltic meteorite from the innermost main belt. *Science* 325:1525–1527.

Bogard D. D. and Garrison D. H. 2009. Ar-Ar impact heating ages of eucrites and timing of the LHB (abstract #1131). 40th Lunar and Planetary Science Conference. CD-ROM.

Bouhifd M. A., Besson P., Courtial P., Gerardin C., Navrotsky A., and Richet P. 2007. Thermochemistry and melting properties of basalt. *Contributions to Mineralogy and Petrology* 153:689–698.

Buchanan P. C., Mittlefehldt D. W., Hutchison R., Koeberl C., Lindstrom D. J., and Pandit M. K. 2000. Petrology of the Indian eucrite Piplia Kalan. *Meteoritics & Planetary Science* 35:609–615.

Bunch T. E. and Keil K. 1971. Chromite and ilmenite in non-chondritic meteorites. *American Mineralogist* 56:146–157.

Cameron M. and Papike J. J. 1981. Structural and chemical variations in pyroxenes. *American Mineralogist* 66:1–50.

Clayton R. N. and Mayeda T. K. 1983. Oxygen isotopes in eucrites, shergottites, nakhlites, and chassignites. *Earth and Planetary Science Letters* 62:1–6.

Clayton R. N., Onuma N., and Mayeda T. K. 1976. A classification of meteorites based on oxygen isotopes. *Earth and Planetary Science Letters* 30:10–18.

Cleverly W. H., Jarosewich E., and Mason B. 1986. Camel Donga meteorite, a new eucrite from the Nullarbor Plain, Western Australia. *Meteoritics* 21:263–269.

Consolmagno G. J. and Drake M. J. 1977. Composition and evolution of the eucrite parent body: Evidence from rare earth elements. *Geochimica et Cosmochimica Acta* 41:1271–1282.

Day J. M. D., Walker R. J., Ash R. D., Liu Y., Rumble D. III, Irving A. J., Goodrich C. A., Tait K., McDonough W. F., and Taylor L. A. 2012. Origin of felsic achondrites Graves Nunataks 06128 and 06129, and ultramafic brachinites and brachinite-like achondrites by partial melting of volatile-rich primitive parent bodies. *Geochimica et Cosmochimica Acta* 81:94–128.

Delaney J. S., Prinz M., Nehru C. E., and Harlow G. E. 1981a. A new basalt group from howardites: Mineral chemistry and relationships with basaltic achondrites (abstract #1075). 12th Lunar and Planetary Science Conference. CD-ROM.

Delaney J. S., Nehru C. E., Prinz M., and Harlow G. E. 1981b. Metamorphism in mesosiderites. Proceedings, 12th Lunar and Planetary Science Conference. pp. 1315–1342.

Delaney J. S., Prinz M., and Takeda H. 1984. The polymict eucrites. *Proceedings, 15th Lunar and Planetary Science Conference, Part 1, Journal of Geophysical Research: Solid Earth* 89 (supplement):C251–C288.

DePaolo D. J. 1981. Trace element and isotopic effects of combined wallrock assimilation and fractional crystallization. *Earth and Planetary Science Letters* 53:189–202.

Ding S., Hough T., and Dasgupta R. 2018. New high pressure experiments on sulfide saturation of high-FeO∗ basalts with variable TiO_2 contents—Implications for the sulfur inventory of the lunar interior. *Geochimica et Cosmochimica Acta* 222:319–339.

Dowty E. 1976. Crystal structure and crystal growth: II. Sector zoning in minerals. *American Mineralogist* 61:460–469.

Duke M. B. 1963. *Petrology of the basaltic achondrite meteorites*. Ph.D. thesis, California Institute of Technology, Passadena, CA, USA.

Duke M. B. 1965. Metallic iron in basaltic achondrites. *Journal of Geophysical Research* 70:1523–1527.

Duke M. B. and Silver L. T. 1967. Petrology of eucrites, howardites and mesosiderites. *Geochimica et Cosmochimica Acta* 31:1637–1665.

Elkins L. T. and Grove T. L. 1990. Ternary feldspar experiments and thermodynamic models. *American Mineralogist* 75:544–559.

Floran R. J. 1978. Silicate petrography, classification, and origin of the mesosiderites: Review and new observations. Proceedings, 9th Lunar and Planetary Science Conference. pp. 1053–1081.

Floss C., Taylor L. A., Promprated P., and Rumble D. III 2005. Northwest Africa 011: A "eucritic" basalt from a non-eucrite parent body. *Meteoritics & Planetary Science* 40:343–360.

Ghosh A. and McSween H. Y. Jr. 1998. A thermal model for the differentiation of asteroid 4 Vesta, based on radiogenic heating. *Icarus* 134:187–206.

Gibson E. K., Moore C. B., Primus T. M., and Lewis C. F. 1985. Sulfur in achondritic meteorites. *Meteoritics* 20:503–511.

Greenwood R. C., Franchi I. A., Jambon A., and Buchanan P. C. 2005. Widespread magma oceans on asteroidal bodies in the early solar system. *Nature* 435:916–918.

Greenwood R. C., Franchi I. A., Jambon A., Barrat J. A., and Burbine T. H. 2006. Oxygen isotope variation in stony-iron meteorites. *Science* 313:1763–1765.

Greenwood R. C., Franchi I. A., Scott E. R. D., Barrat J.-A., and Norman M. 2009. Oxygen isotope variation in the HEDs: How homogeneous is Vesta? (abstract #5436). *Meteoritics & Planetary Science* 44:A81.

Greenwood R. C., Barrat J. A., Scott E. R. D., Janots E., Franchi I. A., Hoffman B., Yamaguchi A., and Gibson J. M. 2012. Has Dawn gone to the wrong asteroid? Oxygen isotope constraints on the nature and composition of the HED parent body (abstract #2711). 43rd Lunar and Planetary Science Conference. CD-ROM.

Greenwood R. C., Burbine T. H., Miller M. F., and Franchi I. A. 2017. Melting and differentiation of early-formed asteroids: The perspective from high precision oxygen isotope studies. *Chemie der Erde-Geochemistry* 77:1–43.

Greenwood R. C., Burbine T. H., and Franchi I. A. 2020. Linking asteroids and meteorites to the primordial planetesimal population. *Geochimica et Cosmochimica Acta* 271:377–406.

Grove T. L., Baker M. B., and Kinzler R. J. 1984. Coupled CaAl-NaSi diffusion in plagioclase feldspar: Experiments and applications to cooling rate speedometry. *Geochimica et Cosmochimica Acta* 48:2113–2121.

Harlow G. E., Delaney J. S., Nehru C. E., and Prinz M. 1982. Metamorphic reactions in mesosiderites: Origin of abundant phosphate and silica. *Geochimica et Cosmochimica Acta* 46:339–348.

Hassanzadeh J., Rubin A. E., and Wasson J. T. 1990. Compositions of large metal nodules in mesosiderites: Links to iron meteorite group IIIAB and the origin of mesosiderite subgroups. *Geochimica et Cosmochimica Acta* 54:3197–3208.

Haughton D. R., Roeder P. L., and Skinner B. J. 1974. Solubility of sulfur in mafic magmas. *Economic Geology* 69:451–467.

Huebner J. and Turnock A. 1980. The melting relations at 1 bar of pyroxenes composed largely of Ca-, Mg-, and Fe-bearing components. *American Mineralogist* 65:225–271.

Janots E., Gnos E., Hofmann B., Greenwood R., Franchi I., Bermingham K., and Netwing V. 2012. Jiddat al Harasis 556: A howardite impact melt breccia with an H chondrite component. *Meteoritics & Planetary Science* 47:1558–1574.

Jérome D. Y. and Goles G. G. 1971. A re-examination of relationships among pyroxene-plagioclase achondrites. In *Activation analysis in geochemistry and cosmochemistry*, edited by Brunfelt A. O. and Steinnes E. Oslo: Universitetsforlaget. pp. 261–266.

Jugo P. J., Wilke M., and Botcharnikov R. E. 2010. Sulfur K-edge XANES analysis of natural and synthetic basaltic

glasses: Implications for S speciation and S content as function of oxygen fugacity. *Geochimica et Cosmochimica Acta* 74:5926–5938.

Kaneda K. and Warren P. H. 1998. Iron-nickel metal bearing unique eucrite Elephant Moraine 92023: Its petrography, siderophile concentrations, and petrogenesis (abstract #5200). *Meteoritics & Planetary Science* 33:A81.

Keil K. 2012. Angrites, a small but diverse suite of ancient, silica-undersaturated volcanic-plutonic mafic meteorites, and the history of their parent asteroid. *Chemie der Erde-Geochemistry* 72:191–218.

Kullerud G. and Yoder H. S. J. 1963. Sulfide-silicate relations. *Carnegie Institution of Washington, Year Book* 62:215–218.

Leys C., Ley C., Klein O., Bernard P., and Licata L. 2013. Detecting outliers: Do not use standard deviation around the mean, use absolute deviation around the median. *Journal of Experimental Social Psychology* 49:764–766.

Mandler B. E. and Elkins-Tanton L. T. 2013. The origin of eucrites, diogenites, and olivine diogenites: Magma ocean crystallization and shallow magma chamber processes on Vesta. *Meteoritics & Planetary Science* 48:2333–2349.

Mason B. 1962. *Meteorites*. New York: Wiley. 274 p.

Mayne R. G., McSween H. Y., McCoy T. J., and Gale A. 2009. Petrology of the unbrecciated eucrites. *Geochimica et Cosmochimica Acta* 73:794–819.

McCoy T. J., Ketcham R. A., Wilson L., Benedix G. K., Wadhwa M., and Davis A. M. 2006. Formation of vesicles in asteroidal basaltic meteorites. *Earth and Planetary Science Letters* 246:102–108.

McQuaig D. R., Simon J. I., Mittlefehldt D. W., and Armytage R. M. G. 2019. Petrographical and geochemical investigations of Stannern group eucrites (abstract #3000). 50th Lunar and Planetary Science Conference. CD-ROM.

McSween H. Y. Jr., Mittlefehldt D. W., Beck A. W., Mayne R. G., and McCoy T. J. 2011. HED meteorites and their relationship to the geology of Vesta and the Dawn Mission. *Space Science Reviews* 163:141–174.

McSween H. Y. Jr., Binzel R. P., De Sanctis M. C., Ammannito E., Prettyman T. H., Beck A. W., Reddy V., Le Corre L., Gaffey M. J., McCord T. B., Raymond C. A., Russell C. T., and the Dawn Science Team. 2013. Dawn; the Vesta–HED connection; and the geologic context for eucrites, diogenites, and howardites. *Meteoritics & Planetary Science* 48:2090–2104.

Metzler K., Bobe K. D., Palme H., Spettel B., and Stöffler D. 1995. Thermal and impact metamorphism on the HED parent asteroid. *Planetary and Space Science* 43:499–525.

Miller M. F. 2002. Isotopic fractionation and the quantification of ^{17}O anomalies in the oxygen three-isotope system: An appraisal and geochemical significance. *Geochimica et Cosmochimica Acta* 66:1881–1889.

Mittlefehldt D. W. 1979. Petrographic and chemical characterization of igneous lithic clasts from mesosiderites and howardites and comparison with eucrites and diogenites. *Geochimica et Cosmochimica Acta* 43:1917–1936.

Mittlefehldt D. W. 1990. Petrogenesis of mesosiderites: I. Origin of mafic lithologies and comparison with basaltic achondrites. *Geochimica et Cosmochimica Acta* 54:1165–1173.

Mittlefehldt D. W. 2005. Ibitira: A basaltic achondrite from a distinct parent asteroid and implications for the Dawn mission. *Meteoritics & Planetary Science* 40:665–677.

Mittlefehldt D. W. 2015. Asteroid (4) Vesta: I. The howardite-eucrite-diogenite (HED) clan of meteorites. *Chemie der Erde-Geochemistry* 75:155–183.

Mittlefehldt D. W. 2021. Mineral analyses and compositional diagrams for eucrite-type achondrites, Version 1.0. Interdisciplinary Earth Data Alliance (IEDA). https://doi.org/10.26022/IEDA/111901.

Mittlefehldt D. W. and Lindstrom M. M. 1993. Geochemistry and petrology of a suite of ten Yamato HED meteorites. *Proceedings of the NIPR Symposium on Antarctic Meteorites* 6:268–292.

Mittlefehldt D. W. and Lindstrom M. M. 1996. Antarctic Stannern and Nuevo Laredo trend eucrites, cumulates, and others (abstract). *Meteoritics & Planetary Science* 31: A90.

Mittlefehldt D. W. and Lindstrom M. M. 2003. Geochemistry of eucrites: Genesis of basaltic eucrites, and Hf and Ta as petrogenetic indicators for altered Antarctic eucrites. *Geochimica et Cosmochimica Acta* 67:1911–1934.

Mittlefehldt D. W., Chou C.-L., and Wasson J. T. 1979. Mesosiderites and howardites: Igneous formation and possible genetic relationships. *Geochimica et Cosmochimica Acta* 43:673–688.

Mittlefehldt D. W., Jones J. H., Palme H., Jarosewich E., and Grady M. M. 1998a. Sioux County—A study in why sleeping dogs are best left alone (abstract #1220). 29th Lunar and Planetary Science Conference. CD-ROM.

Mittlefehldt D. W., McCoy T. J., Goodrich C. A., and Kracher A. 1998b. Non-chondritic meteorites from asteroidal bodies. In *Planetary materials*, edited by Papike J. J. Washington, D.C.: Mineralogical Society of America. pp. 4-1–4-195.

Mittlefehldt D. W., Peng Z. X., and Mertzman S. A. 2016. Compositions of normal and anomalous eucrite-type mafic achondrites (abstract #6324). *Meteoritics & Planetary Science* 51 (Suppl.).

Mittlefehldt D. W., Berger E. L., and Le L. 2017. Petrology of anomalous mafic achondrite polymict breccia Pasamonte (abstract #1194). 48th Lunar and Planetary Science Conference. CD-ROM.

Morimoto N., Fabries J., Ferguson A. K., Ginzburg I. V., Ross M., Seifert F. A., Zussman J., Aoki K., and Gottardi G. 1988. Nomenclature of pyroxenes. *American Mineralogist* 73:1123–1133.

Nyquist L. E., Reese Y., Wiesmann H., Shih C. Y., and Takeda H. 2003. Fossil ^{26}Al and ^{53}Mn in the Asuka 881394 eucrite: Evidence of the earliest crust on asteroid 4 Vesta. *Earth and Planetary Science Letters* 214:11–25.

O'Neill H. S. C. and Mavrogenes J. A. 2002. The sulfide capacity and the sulfur content at sulfide saturation of silicate melts at 1400 C and 1 bar. *Journal of Petrology* 43:1049–1087.

Palme H., Wlotzka F., Spettel B., Dreibus G., and Weber H. 1988. Camel Donga: A eucrite with high metal content. *Meteoritics* 23:49–57.

Papike J. J., Karner J. M., and Shearer C. K. 2003. Determination of planetary basalt parentage: A simple technique using the electron microprobe. *American Mineralogist* 88:469–472.

Papike J. J., Karner J. M., and Shearer C. K. 2005. Comparative planetary mineralogy: Valence state partitioning of Cr, Fe, Ti, and V among crystallographic sites in olivine, pyroxene, and spinel from planetary basalts. *American Mineralogist* 90:277–290.

Prinz M., Nehru C. E., Delaney J. S., Harlow G. E., and Bedell R. L. 1980. Modal studies of mesosiderites and related achondrites, including the new mesosiderite ALHA 77219. Proceedings, 11th Lunar and Planetary Science Conference. pp. 1055–1071.

Righter K. and Drake M. J. 1996. Core formation in Earth's Moon, Mars, and Vesta. *Icarus* 124:513–529.

Righter K. and Drake M. J. 1997. A magma ocean on Vesta: Core formation and petrogenesis of eucrites and diogenites. *Meteoritics & Planetary Science* 32:929–944.

Righter K., Pando K., and Danielson L. R. 2009. Experimental evidence for sulfur-rich Martian magmas: Implications for volcanism and surficial sulfur sources. *Earth and Planetary Science Letters* 288:235–243.

Rousseeuw P. J. and Croux C. 1993. Alternatives to the median absolute deviation. *Journal of the American Statistical Association* 88:1273–1283.

Rubin A. E. and Mittlefehldt D. W. 1992. Classification of mafic clasts from mesosiderites: Implications for endogenous igneous processes. *Geochimica et Cosmochimica Acta* 56:827–840.

Rubin A. E. and Mittlefehldt D. W. 1993. Evolutionary history of the mesosiderite asteroid: A chronologic and petrologic synthesis. *Icarus* 101:201–212.

Russell C. T., Raymond C. A., Coradini A., McSween H. Y., Zuber M. T., Nathues A., De Sanctis M. C., Jaumann R., Konopliv A. S., Preusker F., Asmar S. W., Park R. S., Gaskell R., Keller H. U., Mottola S., Roatsch T., Scully J. E. C., Smith D. E., Tricarico P., Toplis M. J., Christensen U. R., Feldman W. C., Lawrence D. J., McCoy T. J., Prettyman T. H., Reedy R. C., Sykes M. E., and Titus T. N. 2012. Dawn at Vesta: Testing the protoplanetary paradigm. *Science* 336:684–686.

Ruzicka A., Snyder G. A., and Taylor L. A. 1997. Vesta as the HED parent body: Implications for the size of a core and for large-scale differentiation. *Meteoritics & Planetary Science* 32:825–840.

Ruzicka A. M., Greenwood R. C., Armstrong K., Schepker K. L., and Franchi I. A. 2019. Petrology and oxygen isotopic composition of large igneous inclusions in ordinary chondrites: Early solar system igneous processes and oxygen reservoirs. *Geochimica et Cosmochimica Acta* 266:97–528.

Sanborn M. E. and Yin Q.-Z. 2014. Chromium isotopic composition of the anomalous eucrites: An additional geochemical parameter for evaluating their origin (abstract #2018). 45th Lunar and Planetary Science Conference. CD-ROM.

Sanborn M. E., Yin Q.-Z., and Mittlefehldt D. W. 2016. The diversity of anomalous HEDs: Isotopic constraints on the connection of EET 92023, GRA 98098, and Dhofar 700 with Vesta (abstract #2256). 47th Lunar and Planetary Science Conference. CD-ROM.

Sato H. 1984. Partition relation of K between magma and plagioclase in a suite of volcanic rocks from northeast Shikoku, Japan. *Journal of the Japanese Association of Mineralogists, Petrologists and Economic Geologists* 79:47–59.

Schiller M., Baker J., Creech J., Paton C., Millet M.-A., Irving A., and Bizzarro M. 2011. Rapid timescales for magma ocean crystallization on the howardite-eucrite-diogenite parent body. *The Astrophysical Journal Letters* 740:L22.

Schwandt C. S. and McKay G. A. 2006. Minor-and trace-element sector zoning in synthetic enstatite. *American Mineralogist* 91:1607–1615.

Scott E. R. D. 1984. Pairing of meteorites found in Victoria Land, Antarctica. *Memoirs of National Institute of Polar Research, Special Issue* 35:102–125.

Scott E. R. D., Greenwood R. C., Franchi I. A., and Sanders I. S. 2009. Oxygen isotopic constraints on the origin and parent bodies of eucrites, diogenites, and howardites. *Geochimica et Cosmochimica Acta* 73:5835–5853.

Shearer C. K., Burger P. V., Neal C., Sharp Z., Spivak-Birndorf L., Borg L., Fernandes V. A., Papike J. J., Karner J., Wadhwa M., Gaffney A., Shafer J., Geissman J., Atudorei N. V., Herd C., Weiss B. P., King P. L., Crowther S. A., and Gilmour J. D. 2010. Non-basaltic asteroidal magmatism during the earliest stages of solar system evolution: A view from Antarctic achondrites Graves Nunatak 06128 and 06129. *Geochimica et Cosmochimica Acta* 74:1172–1199.

Steele I. M. and Smith J. V. 1976. Mineralogy of the Ibitira eucrite and comparison with other eucrites and lunar samples. *Earth and Planetary Science Letters* 33:67–78.

Steenstra E. S., Knibbe J. S., Rai N., and Van Westrenen W. 2016. Constraints on core formation in Vesta from metal–silicate partitioning of siderophile elements. *Geochimica et Cosmochimica Acta* 177:48–61.

Steenstra E. S., Berndt J., Klemme S., Rohrbach A., Bullock E. S., and Van Westrenen W. 2020. An experimental assessment of the potential of sulfide saturation of the source regions of eucrites and angrites: Implications for asteroidal models of core formation, late accretion and volatile element depletions. *Geochimica et Cosmochimica Acta* 269:39–62.

Stolper E. 1975. Petrogenesis of eucrite, howardite and diogenite meteorites. *Nature* 258:220–222.

Stolper E. 1977. Experimental petrology of eucritic meteorites. *Geochimica et Cosmochimica Acta* 41:587–611.

Takeda H. and Graham A. L. 1991. Degree of equilibration of eucritic pyroxenes and thermal metamorphism of the earliest planetary crust. *Meteoritics* 26:29–134.

Takeda H., Ishii T., Arai T., and Miyamoto M. 1997. Mineralogy of the Asuka 87 and 88 eucrites and crustal evolution of the HED parent body. *Antarctic Meteorite Research* 10:401–413.

Treiman A. H. 1997. The parent magmas of the cumulate eucrites: A mass balance approach. *Meteoritics & Planetary Science* 32:217–230.

Wadhwa M., Amelin Y., Bogdanovski O., Shukolyukov A., Lugmair G. W., and Janney P. 2009. Ancient relative and absolute ages for a basaltic meteorite: Implications for timescales of planetesimal accretion and differentiation. *Geochimica et Cosmochimica Acta* 73:5189–5201.

Warren P. H. 2011. Stable-isotopic anomalies and the accretionary assemblage of the Earth and Mars: A subordinate role for carbonaceous chondrites. *Earth and Planetary Science Letters* 311:93–100.

Warren P. H., Kallemeyn G. W., Huber H., Ulff-Møller F., and Choe W. 2009. Siderophile and other geochemical constraints on mixing relationships among HED-meteoritic breccias. *Geochimica et Cosmochimica Acta* 73:5918–5943.

Warren P. H., Rubin A. E., Isa J., Gessler N., Ahn I., and Choi B.-G. 2014. Northwest Africa 5738: Multistage fluid-driven secondary alteration in an extraordinarily evolved eucrite. *Geochimica et Cosmochimica Acta* 141:199–227.

Warren P. H., Isa J., Ebihara M., Yamaguchi A., and Baecker B. 2017. Secondary-volatiles linked metallic iron in eucrites: The dual-origin metals of Camel Donga. *Meteoritics & Planetary Science* 52:737–761.

Wasson J. T. 2013. Vesta and extensively melted asteroids: Why HED meteorites are probably not from Vesta. *Earth and Planetary Science Letters* 381:138–146.

Wiechert U. H., Halliday A. N., Palme H., and Rumble D. 2004. Oxygen isotope evidence for rapid mixing of the HED meteorite parent body. *Earth and Planetary Science Letters* 221:73–382.

Wilkening L. L. and Anders E. 1975. Some studies of an unusual eucrite: Ibitira. *Geochimica et Cosmochimica Acta* 39:205–1210.

Wimpenny J., Sanborn M. E., Koefoed P., Cooke I. R., Stirling C., Amelin Y., and Yin Q. Z. 2019. Reassessing the origin and chronology of the unique achondrite Asuka 881394: Implications for distribution of ^{26}Al in the early solar system. *Geochimica et Cosmochimica Acta* 244:478–501.

Yamaguchi A., Taylor G. J., and Keil K. 1996. Global crustal metamorphism of the eucrite parent body. *Icarus* 124:97–112.

Yamaguchi A., Taylor G. J., and Keil K. 1997. Not all eucrites are monomict breccias (abstract #1360). 28th Lunar and Planetary Science Conference. CD-ROM.

Yamaguchi A., Taylor G. J., Keil K., Floss C., Crozaz G., Nyquist L. E., Bogard D. D., Garrison D. H., Reese Y. D., Wiesmann H., and Shih C.-Y. 2001. Post-crystallization reheating and partial melting of eucrite EET90020 by impact into the hot crust of asteroid 4Vesta ~4.50 Ga ago. *Geochimica et Cosmochimica Acta* 65:3577–3599.

Yamaguchi A., Clayton R. N., Mayeda T. K., Ebihara M., Oura Y., Miura Y. N., Haramura H., Misawa K., Kojima H., and Nagao K. 2002. A new source of basaltic meteorites inferred from Northwest Africa 011. *Science* 296:334–336.

Yamaguchi A., Setoyanagi T., and Ebihara M. 2010. An anomalous eucrite, Dhofar 007, and a possible relationship with the mesosiderites. *Meteoritics & Planetary Science* 41:863–874.

Yamaguchi A., Shirai N., Okamoto C., and Ebihara M. 2017. Petrogenesis of the EET 92023 achondrite and implications for early impact events. *Meteoritics & Planetary Science* 52:709–721.

Zhang A.-C., Wang R.-C., Hsu W.-B., and Bartoschewitz R. 2013. Record of S-rich vapors on asteroid 4 Vesta: Sulfurization in the Northwest Africa 2339 eucrite. *Geochimica et Cosmochimica Acta* 109:1–13.

SUPPORTING INFORMATION

Additional supporting information may be found in the online version of this article.

Table S1. Oxygen isotopic anomaly in median absolute deviation (MAD) units for diogenites and eucrite-type achondrites, Open University data.

Table S2a. Pyroxene compositional characteristics for EET 87520 calculated for each instrument and by analysis set (a, b, etc.).

Table S2b. Pyroxene compositional characteristics for ALH 85001 calculated for each instrument and by analysis set (a, b, etc.).

Table S3. Olivine compositional parameters in eucrite-type achondrites; Fe/Mg and Fe/Mn—mole ratios; mg#—mole%.

Table S4. Cobalt and Ni contents (wt%) of metal in select eucrite-type achondrites.

Table S5. Synopsis of low-Ca pyroxene compositional parameters for different possible endmembers of GRA 98098; Fe/Mg and Fe/Mn—mole ratios; Wo—mole%.

Fig. S1. Probability density function plots for Fe/Mn ratios of low-Ca pyroxenes for analyses done on different electron microprobes in this study: (a) medium-grained basaltic eucrite EET 87520; (b) medium-grained, brecciated cumulate eucrite ALH 85001. Thin section numbers are included in the legend. See text for description of how the probability curves are calculated. Horizontal lines are $\pm 3\sigma$ standard deviation on the mean, taken from Table S2; tick marks show 1σ increments.

Fig. S2. Silicon in atoms per formula unit versus molar Fe/Mn for Fe-calibration tests on (a) EET 87520 and (b) ALH 85001 on the SX100 and JEOL microprobes. Abbreviations indicate standard used for Fe calibration: Jh = Johnstown hypersthene; Kh = Kakanui hornblende; Mo = Marjalahti olivine; Rf = Rockport fayalite; sf = synthetic fayalite; Sk = Spring Mountains kaersutite; So = Springwater olivine. Older data are identified by probe and Fe standard. Error bars are 1σ standard deviations.

Fig. S3. Δ^{17}O versus δ^{18}O for different analysis sets for paired eucrite-type basalts PCA 82502 and PCA 91007 compared to an average of all Open University analyses for Pasamonte. Labels give the sample split, treatment type and the number of analyses. Treatment type: e = EATG residue; h = HCl residue; u = untreated. Error bars are 1σ standard deviations.

Fig. S4. a) Backscattered electron image of pyroxene grain in medium-grained basaltic eucrite EET 87520 showing a Ca-poor region (lighter gray) relatively free of augite lamellae (medium gray) with zoning out to more Ca-rich regions indicated by denser augite lamellae. Au = augite; Pg = pigeonite; Pl = plagioclase; Si = silica phase. b) Histogram of pyroxene analyses excluding Camebax analyses. Inset shows low-Ca pyroxene analyses binned by 0.05 mole% Wo. Note tail towards higher Wo contents caused by beam overlap on augite lamellae. c) Plot of Fe/Mn versus Wo for EET 87520. Inset shows analyses with Wo<6.8; box shows limits used to define low-Ca pyroxene. d) Expansion of (c) inset focusing on the upper Wo limit used to define low-Ca pyroxene.

Fig. S5. a) Plot of Fe/Mn versus Wo for GRA 98098 showing all analyses. b) Expansion showing densest population of analyses with $Wo_{\leq 21}$, with the most compact cluster enclosed by the dashed box. c) Expansion showing three possible upper limits for Wo that could be chosen to define low-Ca pyroxene.

Fig. S6. Pyroxene quadrilateral diagram for individual analyses from two thin sections each of EET 87520 and EET 87542 eucrites. Pyroxene compositions for each taken from initial descriptions in the *Antarctic Meteorite Newsletter* (AMN) are also shown. Endmember compositions for Sioux County basalt clasts are shown for comparison.

Fig. S7. Composite elemental maps and back-scattered electron images of the four GRO eucrites showing textures and mineralogy.

Fig. S8. Pyroxene quadrilateral diagrams for the four GRO eucrites. Individual analyses and endmembers are shown for each. Endmember compositions for Sioux County basalt clasts are shown for comparison.

Fig. S9. A 3-D plot of Wo, Fe/Mg, and Fe/Mn tilted to show the complete separation of GRO 17070 from the others, the complete overlap of GRO 17098 and GRO 17200, and high-Mg compositions present in GRO 17210 but not the others. GRO 17070 contains two compositional groups of low-Ca pyroxene, named type-a and type-b.

Fig. S10. Histograms of pyroxene analyses with $Wo_{\leq 3.5}$ in three of the GRO eucrites. The dashed line is the cutoff Wo content for those pyroxenes plotted in Fig. S11.

Fig. S11. Histograms of mg# for pyroxene analyses with $Wo_{\leq 2.5}$ in three of the GRO eucrites. The dashed line is the cutoff in mg# (41.2) used to parse the pyroxene data for the parsed median; mg# = 100* (MgO/[MgO + FeO]).

Fig. S12. Orthoclase versus albite contents for plagioclase analyses from all four GRO eucrites. The polynomial fit is a two-degree polynomial fit to the GRA 98098 data (see discussion in the parent paper) and the dotted curves are ± 0.25 Or about the fit. All GRA 98098 fall within that envelope. The dashed line is the *y*-axis maximum used in Fig. S13.

Fig. S13. Orthoclase versus albite contents for plagioclase analyses from all four GRO eucrites, with the polynomial fit and envelope as in Fig. S12.

Fig. S14. MnO versus MgO for ilmenite grain averages for the four GRO eucrites.

Fig. S15. Ternary diagram for chromite grain averages for the four GRO eucrites. The dashed line is the median molar Al/Cr for all eucrites from this study.